August 2021

Initial Investigation of Connection Behavior for Buckling-Restrained Braces (BRBs) in Precast Concrete Frames

Hannah Dillingham Kessler
Clemson University, hfdillingham@gmail.com

INITIAL INVESTIGATION OF CONNECTION BEHAVIOR FOR BUCKLING-RESTRAINED BRACES (BRBs) IN PRECAST CONCRETE FRAMES

A Thesis
Presented to
the Graduate School of
Clemson University

In Partial Fulfillment
of the Requirements for the Degree
Master of Science
Civil Engineering

---

by
Hannah Dillingham Kessler
August 2021

Accepted by:
Laura Redmond, Committee Chair
Brandon Ross
M.Z. Naser

ABSTRACT

Recently, there has been increased interest in using buckling-restrained braces (BRBs) in pinned precast concrete frames located in seismic zones. BRB frames (BRBFs) are a relatively new, but well-understood lateral force resisting system for steel structures. A codified method of design for precast BRBFs cannot be created due to a lack of experimental studies on this system. To act as a first step in the codification process, the objectives of this thesis are to complete an extensive review of potential brace-to-frame connection designs for precast BRBFs and to experimentally test a connection design through representative seismic loads. To complete the first objective many potential connection designs were examined, including some that had the advantage of eliminating gravity load transfer from the precast frame into the connection or brace. Some of these connections were candidates for testing, but constructability issues, undesirable bolt loading states, an incompatibility with a wide range of bay sizes, and other factors caused these connections not to be chosen for test. A traditional gusset plate connection using the Uniform Force Method (UFM) for force distribution was selected for the experimental program as it is widely used for BRB connections to steel frames. A quasi-static cyclic test was performed on a scaled, partial precast frame to determine the validity of the connection interface forces predicted by the UFM as compared to the interface forces observed in testing. Additional conclusions about the behavior of the system were inferred using a simplistic finite element model correlated to the experimental results. Experimental results implied that the UFM alone is not accurate in predicting gusset plate interface forces for this system. The test results indicated there

is likely some change in this distribution due to frame action. In addition, a deviation from the pinned force distribution among precast members that varied with frame displacement implied that there is some change in column base fixity as the frame undergoes larger horizontal displacements. The simplistic finite element model tuned column base stiffness and showed an increase in stiffness as a potential cause for this deviation. This thesis concludes by outlining two possible approaches to continue research towards codification of precast BRBFs based on the results of this research.

ACKNOWLEDGEMENTS

My gratitude goes out to numerous people for their aid in my graduate studies. First, I would like to thank my advisor, Dr. Laura Redmond, for taking a chance on the undergraduate that approached her looking for research experience on the first day of classes. I am grateful she asked me to stay on with her for graduate school and be a part of this project. I truly owe everything I know about the experimental process to Dr. Redmond; it is impossible not to learn from her dedication, thoroughness, and depth of technical knowledge. I would also like to thank the Precast/Prestressed Concrete Institute who provided funding for this project, along with an advisory board whose advice was invaluable: Jared Brewe, Harry Gleich, Suzanne Aultman, Brandon Ross, Jon Mohle, Kim Seeber, Kevin Kirkley, Greg Force, Tom Schaeffer, and Jeff Viano. I am grateful to Metromont Corporation and CoreBrace for lending the expertise of Fanfu Fan, Corbin Martin, and Brandt Saxey. Dr. Garrett Pataky and Kaitlynn Conway of the mechanical engineering department were a great help and generous with their equipment and time. My fellow research group members, Rob Locke, John Bell, John Crowder, Omar Abuodeh, Rumi Shrestha, Stephen Wright, and Hannah Stewart were absolutely critical in the completion of the experimental work and also served as great friends. Finally, I am grateful to my ever-supportive husband, Charlie, and my wonderful parents, Tim and Lee. They encouraged, loved, and comforted me through many highs and lows. I would not have made it here without them.

TABLE OF CONTENTS

Page

Table of Contents (Continued)

LIST OF TABLES

LIST OF FIGURES

List of Figures (Continued)

Figure Page

List of Figures (Continued)

List of Figures (Continued)

Figure Page

List of Figures (Continued)

CHAPTER ONE

INTRODUCTION

Motivation

Buckling-restrained braced (BRB) frames have become a well-established lateral force resisting system (LFRS) for steel construction. The use of precast buckling-restrained braced frames (BRBFs) would simplify connections and reduce weight of the LFRS, while also providing sufficient strength and ductility. To date, the research conducted on BRB frames in precast systems is insufficient to codify a method of design.

The most common type of BRB is the unbonded brace which typically consists of three elements: a steel core which can deform plastically in tension and compression, and a steel tube filled mortar or concrete which surrounds the brace and prevents buckling [1]. BRBs have been shown to possess enough rigidity to satisfy structural drift limits, provide significant energy absorption, and reduce forces on foundations and adjacent members [1, 2, 3, 4]. Testing procedures for BRB subassemblages and design procedures for steel structures utilizing BRBs have been codified in AISC 341, Seismic Provisions for Steel Buildings, since its 2005 edition [5].

Currently, the most common LFRSs for precast structures are shear walls and moment frames [6]. Both shear walls and moment frames include cast-in-place elements, post-tensioned connections, and/or grouted connections which limit some of the inherent benefits of selecting a precast system like quick erection time, higher quality control, and lower project costs [7]. In addition, shear wall systems add undesirable seismic weight to the structure.

BRBs were recently used as the LFRS for a precast structure in the New Madrid seismic zone of the United States [8]. BRBs were selected as they eliminated the need for moment connections and shear walls and provided sufficient load capacity and seismic drift levels. Because there is little research regarding precast BRBFs and there is currently no codified procedure for design, the engineers had to justify the system to local building authorities. If the use of precast concrete BRBFs could be codified, it would greatly increase the viability of precast construction in seismic zones.

Objectives and Technical Approach

An advisory board made up of experienced professionals working in or associated with the precast concrete industry was provided to the researchers by the Precast/Prestressed Concrete Institute, the sponsors of this work. The objectives of this work were identified through reviewing existing literature on the topics and through discussion with the advisory board.

The first objective of this research was to determine candidate design options for the BRB connection and the precast beam and column. Initially, several deterministic connection designs were considered to join the precast components to the BRB that were aimed at eliminating transfer of gravity load into the brace. However, after discussion with the advisory board, a traditional gusset plate connection was chosen for this initial experiment because of its widespread and accepted use for braced frames, including BRBFs.

Two methods for determining distribution of brace force to the gusset plate interfaces were considered in this work: the “keep it simple stupid” (KISS) method and

the Uniform Force Method (UFM). The KISS method requires moments be transferred at the connection interfaces, whereas the UFM sizes the gusset to distribute forces such that force equilibrium is achieved without interface moments [9]. Ultimately the UFM was selected as it distributed tension across both the beam and column interfaces. This allowed the use of common rebar sizes, reinforcing steel grades, and corbel dimensions. Although other research has shown deviation from the UFM in fixed frames due to frame action [10-13], a precast system is more flexible at the beam-column connection and therefore theoretically closer to the assumptions of the UFM. A more detailed description of the connection selection and design processes can be found in Chapter 2 of this thesis.

Ordinary, intermediate, and special moment frame detailing as specified in ACI 318-19 Chapter 18 [14] were considered during the initial design stages of the precast beam and column. Ultimately, special moment frame detailing was chosen because it would provide the most conservatism and ductility for an initial prototype. Though special moment frame detailing was specified for the precast beam and column, the frame was assumed to be fully pinned for force distribution between members. Typical "pinned" precast column base and beam-column jumper plate connections were used in addition to the "pinned" gusset plate connection. Though a typical welded or bolted gusset is assumed to act as a pin in the overall frame, designers still must consider moments at the gusset connections to the beam and column by either eliminating them through using the UFM or designing for them using the KISS method. For more detailed information on design of precast members, see Chapter 3 of this thesis.

The second objective of this research was to determine the adequacy of the force distribution assumed by the UFM with a physical test on a precast concrete frame. The schematic of the test set up used in this work is shown in **Figure 1**. The behavior of a BRBF under load due to a seismic event was simulated with two servo-controlled hydraulic actuators. The horizontal or "beam" actuator was used to apply a small displacement increment after which the diagonal or "brace" actuator was adjusted to the correct force from a pre-determined BRB hysteresis curve. Further explanation of the testing procedure is provided in Chapter 4 of this thesis. This testing approach was inspired by BRB steel connection tests executed by Coy in 2007 [15].

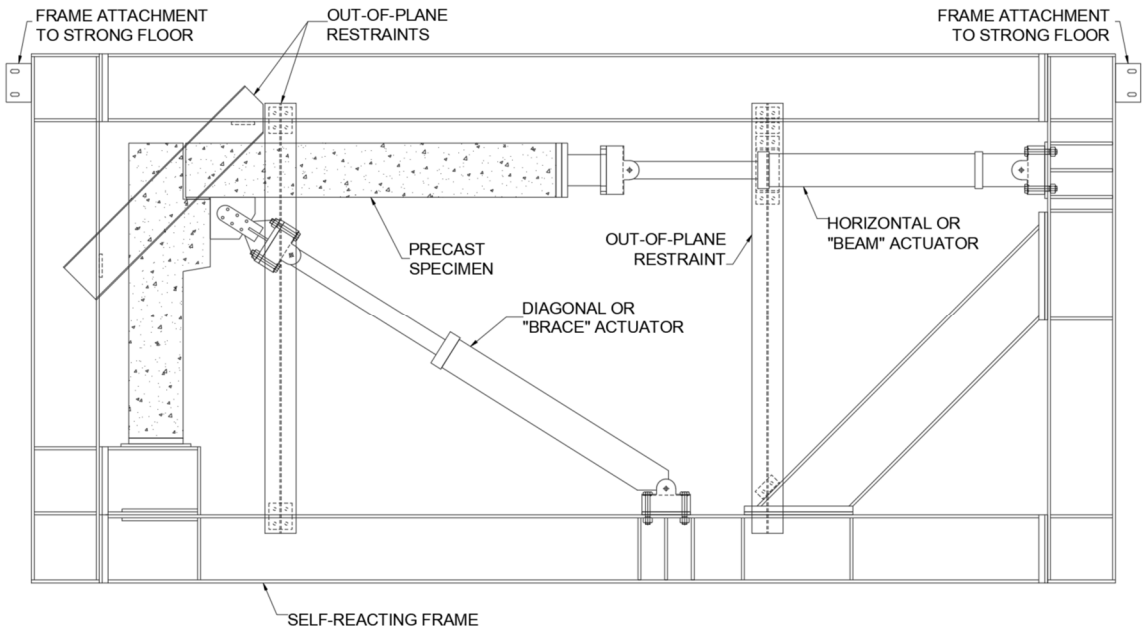

Figure 1: Overview of test setup

To determine the distribution of forces through the gusset plate, strain gauges were applied along the gusset edges that connected to the beam and column. Experimental interface forces were determined from these gauge measurements through a

procedure described in Chapter 5 of this thesis. In addition, the assumption of approximately pinned connections was checked during testing through load cells integrated with the servo-controlled hydraulic actuators. Additional supporting evidence for the relative forces in the beam and column was collected by monitoring the formation of cracks with each test cycle and the precast member deformations.

This pinned frame assumption was determined to be incorrect from experimental results. To better understand one potential cause for this discrepancy a simplistic finite element model (FEM) was created to study the effects of column partial fixity. Experimental results implied that column base fixity may have increased at higher frame displacements, so the model varied stiffnesses of rotational springs that represented this fixity to verify or disprove this as a source of the discrepancy. The model and its results are discussed in detail in Chapter 5 of this thesis.

Though this test is the first step in codifying the use of precast BRBFs, the singular specimen tested in this program is not enough to inform a robust design methodology on its own. Recommendations for two potential paths to expand on this work follow in Chapter 6 of this thesis.

Significance of Work

This work is of particular significance because no other experimental studies exist on traditional steel BRBs in precast concrete frames that meet the objectives of this work. Guerrero et al. [16] tested ⅓ scale precast moment frames with BRBs on a shake table but did not characterize the load path at the BRB-to-frame connection. There is also limited research existing on the applicability of the UFM to concrete structures, particularly

precast concrete structures. Though the influence of frame action on gusset interface forces in fixed frames has been well-studied [10-13], there is a lack of information on its influence in pinned or partially fixed frames. This research has shown that the typical connections of a precast system are not flexible enough to satisfy the pinned assumptions of the UFM and that the force distribution across the gusset plate connecting the BRB to the beam and column changes with increasing horizontal frame displacement. This research has laid the groundwork for formulating a performance-based design methodology for precast BRBFs.

Document Outline

This thesis is organized into six chapters. Chapter 1 contains the introductory information. Chapter 2 contains a detailed description of connection design. Chapter 3 contains descriptions of the prototype structure and precast member designs. Chapter 4 details the experimental program design. Chapter 5 presents the results and discusses their implications. Chapter 6 provides conclusions about the implications of this research and some suggestions for future work. The modified procedure for determining BRB hysteresis, detailed member design calculations, and selected raw data can be found in the Appendices.

CHAPTER 2

CONNECTION DESIGN

A significant contribution of this work was to thoroughly examine the options for designing the connection of a BRB to a precast system and present them before the advisory board. This chapter first presents the initial designs considered and summarizes the reasons they ultimately were not selected for the tested configuration. The gusset plate connection design which was used for the test specimen is presented after.

Initial Connection Designs

An early concern of the advisory board was that high gravity loads in many precast structures could lead to large compression loads and moments transferred into the connection and into the BRB. Because of this, several ideas for connections that would not transfer gravity load from the beam to the BRB and its connection were considered in the beginning stages of design.

Non-Gravity Load Transferring Connections

A variety of connections were considered that would eliminate gravity load transfer from the beam to the brace and gusset plate. Several ideas used slotted or oversized holes, air gaps, or a combination of the two to eliminate this transfer. Some examples are shown in **Figures 2** and **3**. Despite these connections' advantage of using standard parts, each had several drawbacks. Connection designs using air gaps would have led to combined shear and bending in the bolts. Because this bolt load state is not typically allowed in practice, characterizing this behavior would require an extensive test program of varying gap and bolt sizes. Oversized or slotted holes have the drawback of

allowing the individual bolts of a connection to be engaged at different times. The bolts that engage first must undergo higher plastic deformation before the following bolts are engaged. This could have caused one bolt to be overloaded. Tight tolerances would have been required to prevent this condition.

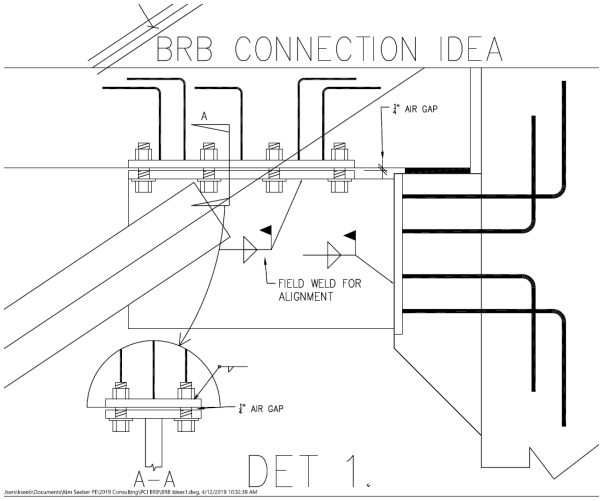

Figure 2: Connection with bolts in single shear, 1/4" air gap to prevent gravity load transfer

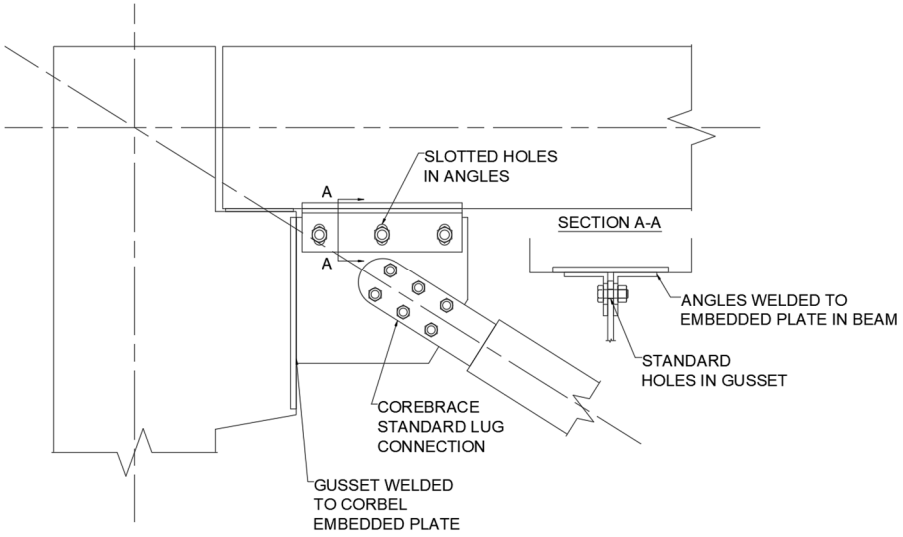

Figure 3: Connection with bolts in double shear, slotted holes to prevent gravity load transfer

Another design considered was one that would connect the BRB directly to the column through welding the BRB to an embedded plate in the bottom of the corbel. This

design was advantageous because it circumvented attaching to the beam entirely and the connection itself was not complex. This design could have been acceptable with narrow spans but would have be difficult to incorporate in cases where a wide span was needed.

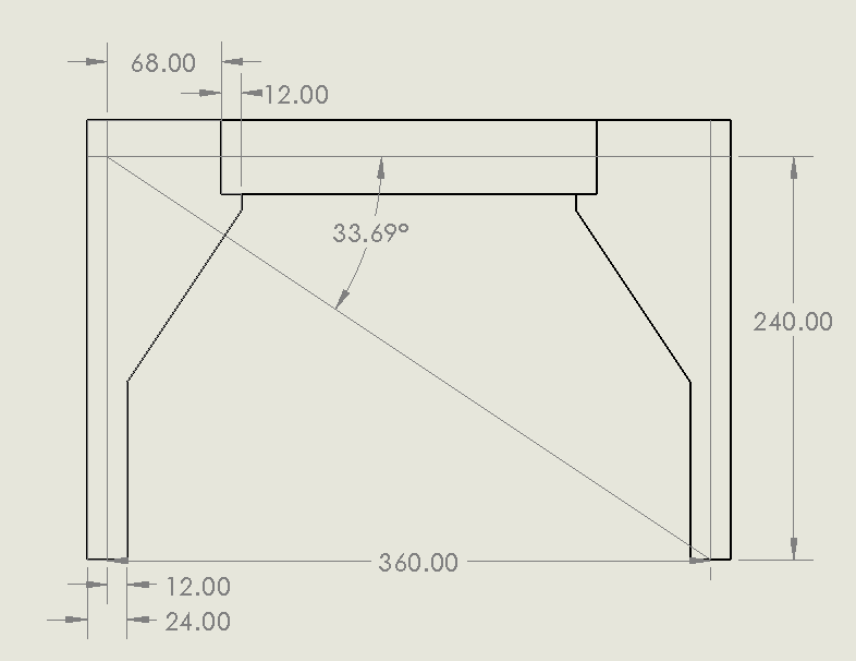

Figure 4: Example of bay construction allowing BRB to be connected directly to bottom of corbel

A design in which a lug connection was welded solely to an embedded plate in the corbel was considered, see **Figure 5** below. This connection had the advantages of a deterministic load path and complete negation of gravity load transfer from the beam to the BRB and its connection. This connection would also be compatible with pinned lug ends available on BRBs produced by CoreBrace, a BRB manufacturer in the United States. The corbel and connection were preliminarily sized for a moderate brace force of 270 kips using ACI 318-19 Chapter 16.5 [14] and Chapter 9 of the 1969 Air Force Stress Analysis Manual [17], respectively. It was found that while a connection transferring the entire brace load to the corbel was feasible, it would require a minimum of (8) Grade 60

#9 bars as primary corbel reinforcing at the top and (12) at the bottom. These bars would have to be placed in two layers and at a tight spacing, which may have led to constructability issues. The lugs would be more than 2" thick. Additionally, as noted on CoreBrace's website, this pinned lug connection requires tighter erection tolerances [18].

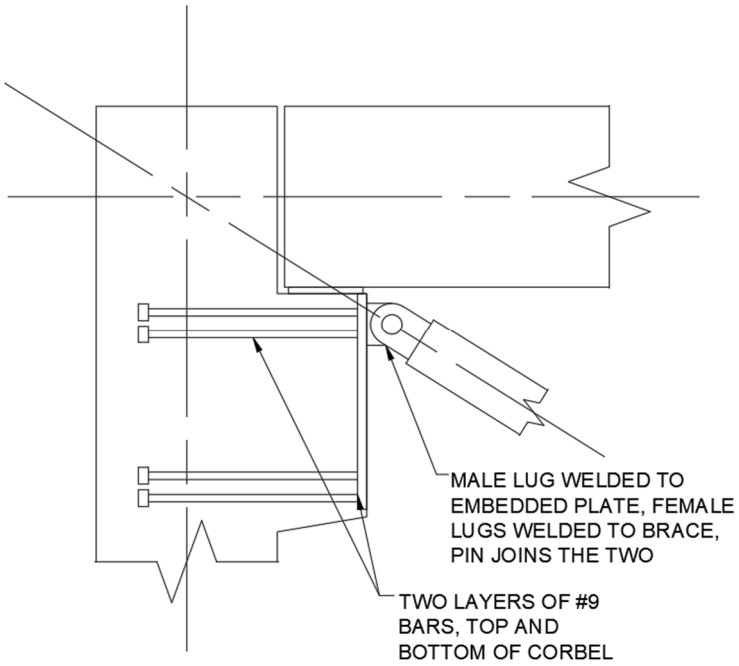

Figure 5: Pinned lug connection

Gusset Plate Connection Design

Ultimately, it was decided by the advisory board that for the pathfinding efforts associated with this test, more complex connections that eliminated gravity load transfer from the beam would not be pursued. Instead, it was determined that an acceptable method to ensure as little gravity load as possible was transferred was to install the braces after the floor topping was poured and cured. Therefore, a traditional gusset plate connection was used. Though these connections are not deterministic, two commonly

used methods exist to approximate forces transferred to each connected edge of the gusset from the brace: the KISS method and the UFM.

The KISS method assumes that the total horizontal component of the brace force is applied as a shear force along the beam connected interface and the total vertical component of the brace force is applied as a shear force along the column connected interface. To maintain moment equilibrium about the work point between the beam and column large moments must be transmitted at the beam and column connected interfaces which can lead to uneconomical gusset configurations [19].

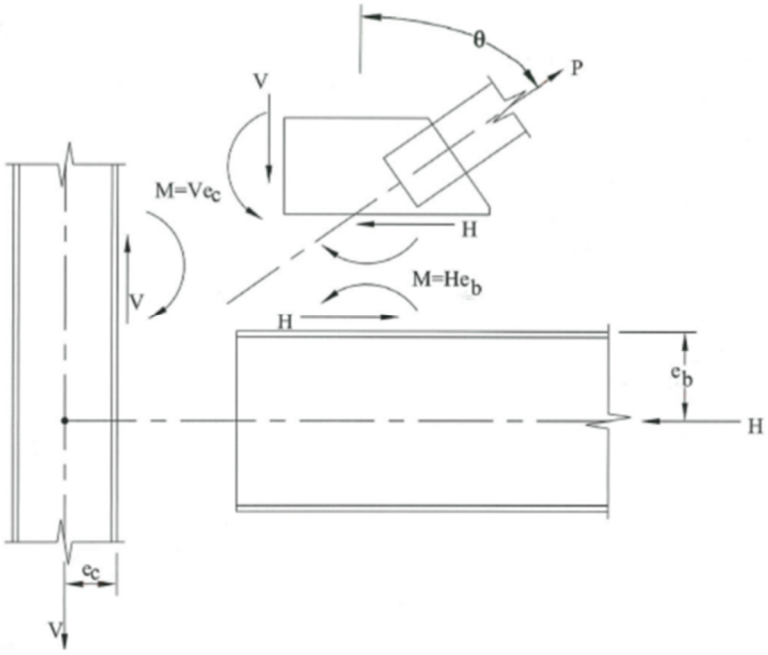

Figure 6: KISS method interface force and moment distribution [19]

The UFM was developed by William Thornton and first appeared in the AISC Steel Construction Manual in 1992 [19]. The UFM assigns dimensions of gusset connected edges such that no interface moments occur on any of the three connection interfaces: the gusset-to-beam, gusset-to-column, and beam-to-column interfaces [20].

The dimensional constraints required by the UFM can sometimes force oddly shaped or large gusset plates [19].

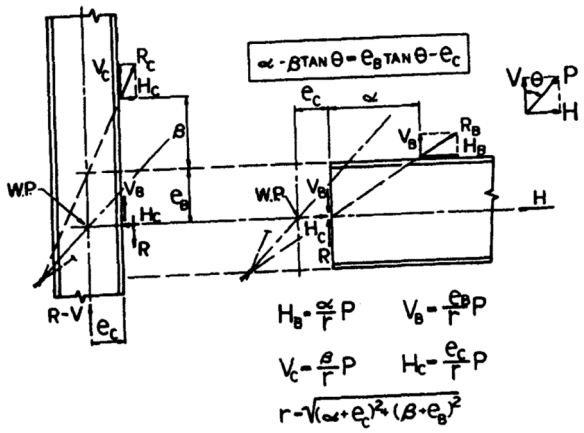

Figure 7: UFM geometric relationships and force distribution [9]

This method was validated on two different sets of idealized steel gusset connection tests [21, 22]. A more recent analytical study [23] based on experimental tests on an idealized fixed concrete joint with gusset plate tested in direct tension [24] showed promising correlation between experimental and analytical interface forces and those predicted by the UFM.

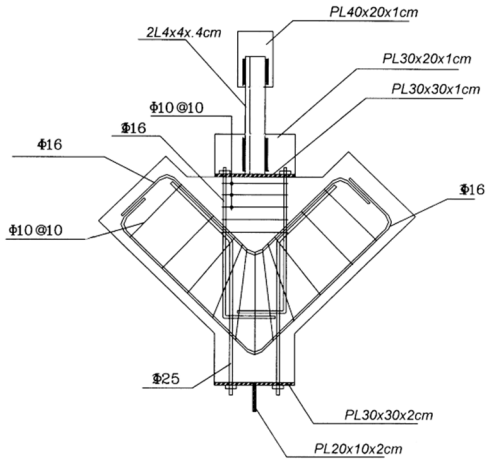

Figure 8: One type of specimen tested by Maheri and Hadjipour [24]; direct tension applied to PL40x20x1cm and restrained at PL20x10x2cm

Though it resulted in a similar reinforcing scheme, the KISS method was not used in this design as the UFM is the method of design adopted in the AISC Steel Construction Manual. Both the KISS method and UFM have the drawback of not accounting for frame action, which is the addition of forces (shear and normal) to the gusset plate by the opening or closing of the angle between the beam and column [11]. Thornton proposed that frame action be ignored for concentric connections in his initial derivation of the UFM [9], but later studies on steel and cast-in-place concrete fixed frames [10-13] have shown that frame action can alter the gusset interface forces significantly. It was shown by Lin [11] that the shear force at the connected interfaces is increased in magnitude and the normal force at the connected interfaces is decreased in magnitude by frame action.

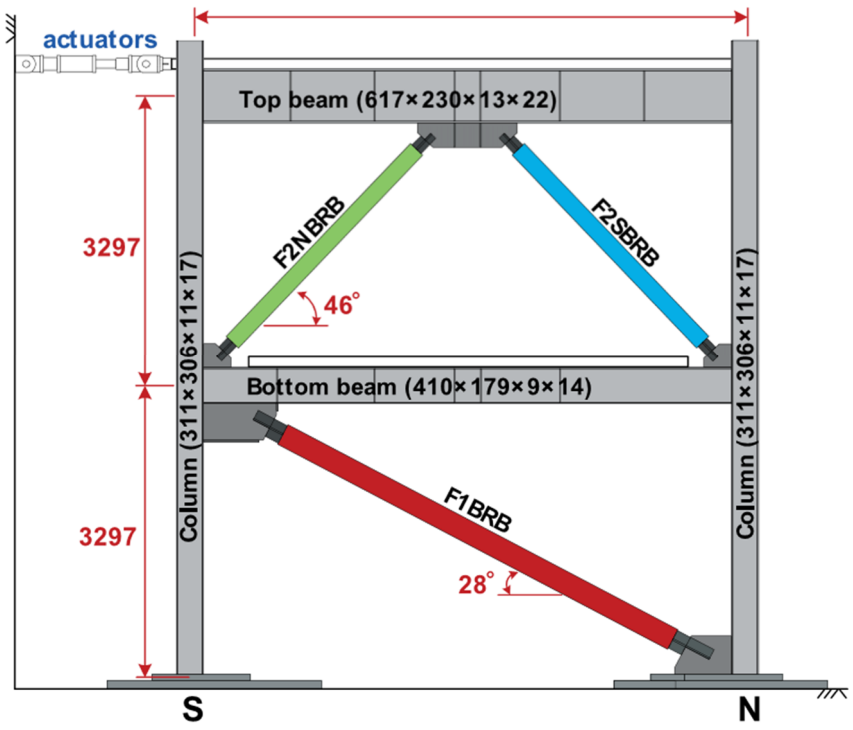

Figure 9: The tested steel frame of Lin [11] with welded moment-resisting connections between beam and column members

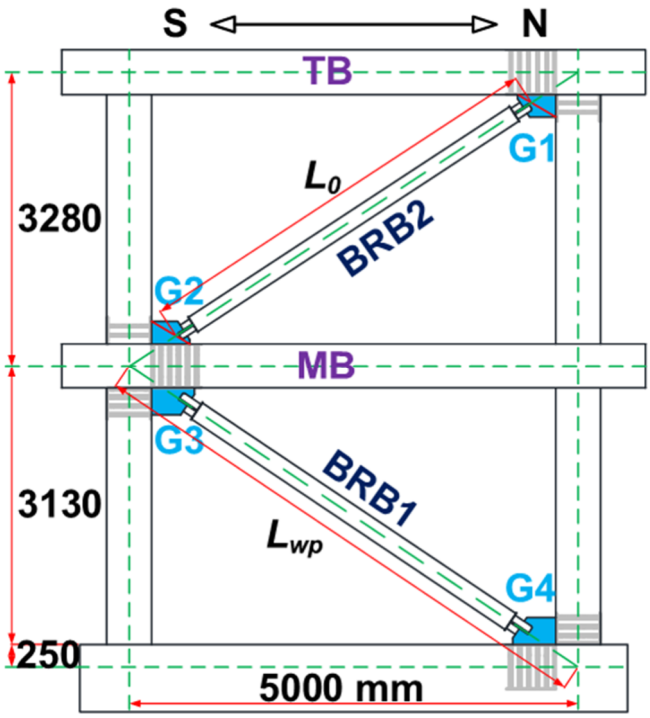

Figure 10: The tested cast-in-place concrete frame of Tsai [12], moment-resisting connections between beam and column members

Precast systems are much closer to pinned conditions assumed by the UFM than these tests. No BRB frame tests with approximate pinned connections that attempted to validate the force distribution assumed by the UFM were found in the literature. Despite the uncertainty of whether frame action would play a significant role in the force distribution for this test, the UFM was chosen for design as it is widely used, recommended by the AISC Steel Construction Manual, and assigned both normal and shear forces to connected interfaces while avoiding undesirable large moments.

Load Path for UFM

It is typical practice to utilize a bearing pad, usually neoprene or random oriented fiber (ROF), at the beam-corbel bearing, so a ¼" ROF bearing pad was included in this

specimen's design. As a result, the beam was raised off the corbel and the connected length of gusset at the column interface was shortened. This gap was increased to ¾" by a difference between the as-built and prescribed design. This needed to be accounted for in the load distribution assigned by UFM. The solution was to assign load to the beam and column using the full length of the gusset at the beam and column interfaces but apply the column vertical and horizontal force components at the center of the connected interface at the column. This induced a small moment at the column interface that is described by the **Equation 1** and shown in **Figure 11**.

$$M_c = V_c e_c + V_b\left(e_c + \frac{l_b}{2}\right) - H_b e_b - H_c\left(e_b + l_g + \frac{l_c - l_g}{2}\right) \quad (1)$$

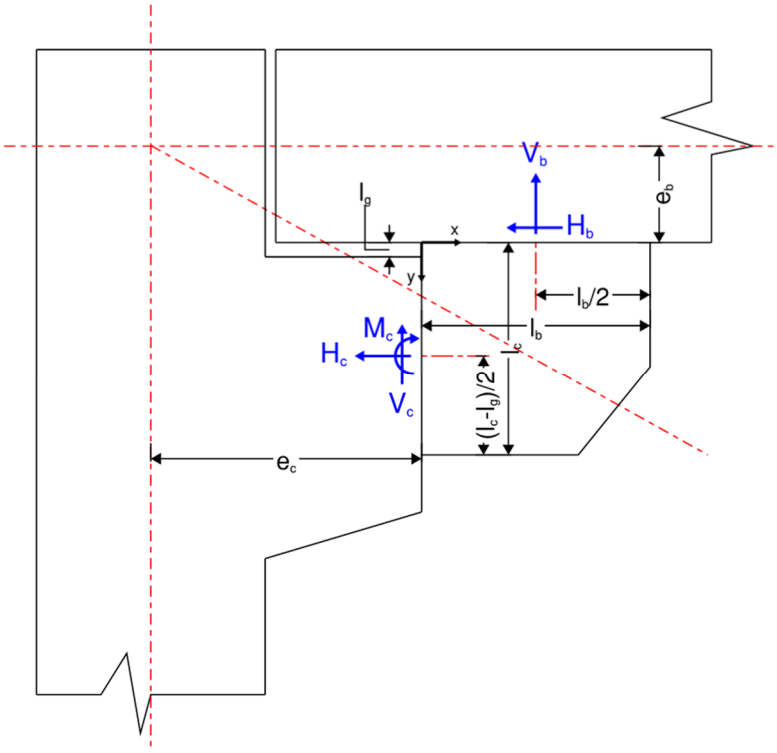

Figure 11: Interface force distribution adjusted for gap between beam and corbel

General load path is displayed for the case where the brace is in tension in **Figure 12**. Red arrows are external forces on the system, blue arrows are internal member forces, and green arrows are external reactions.

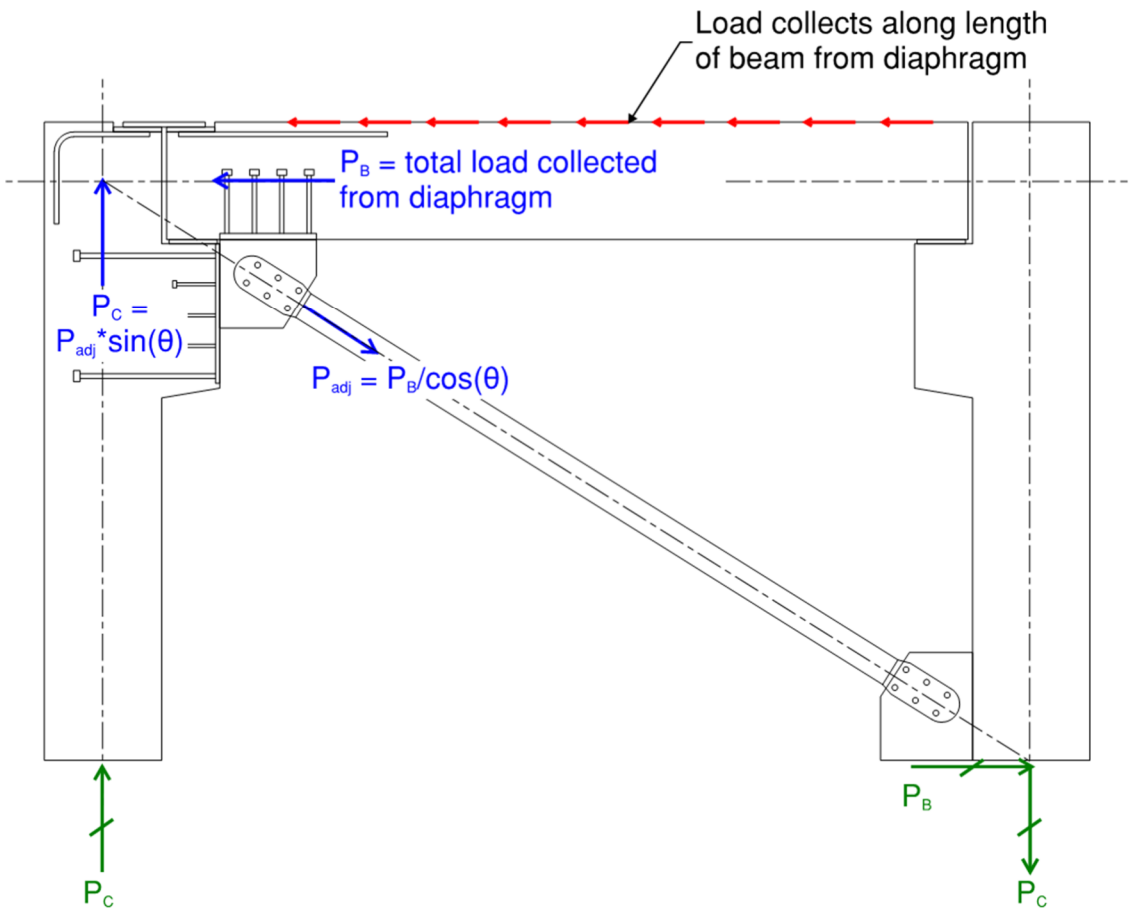

Figure 12: Frame load path, brace in tension

Figures 13 through **16** display the loads as they travel through each of the horizontal force resisting components and vertical force resisting components of both beam-column connections.

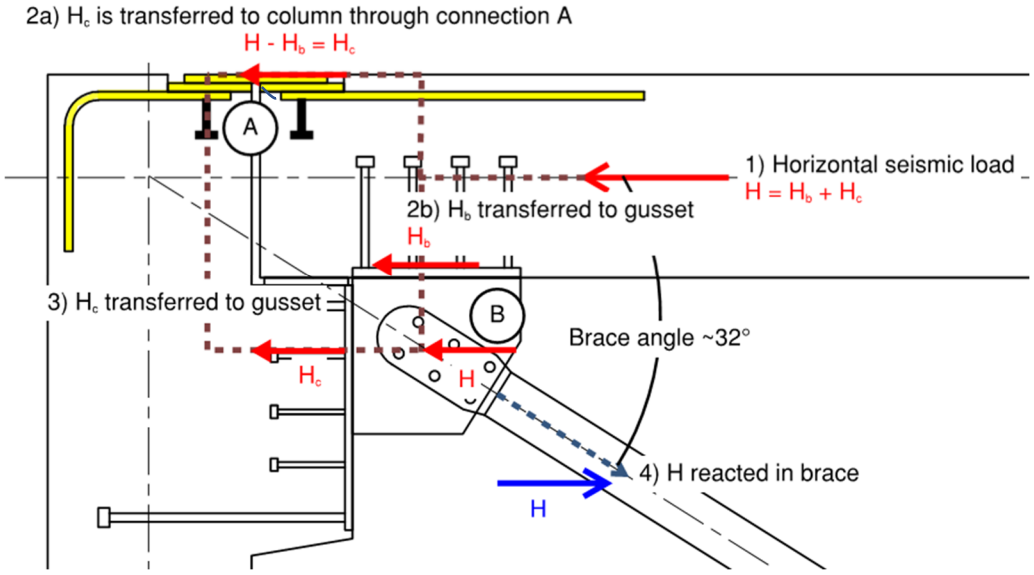

Figure 13: Horizontal load path for beam-column connections, brace in tension

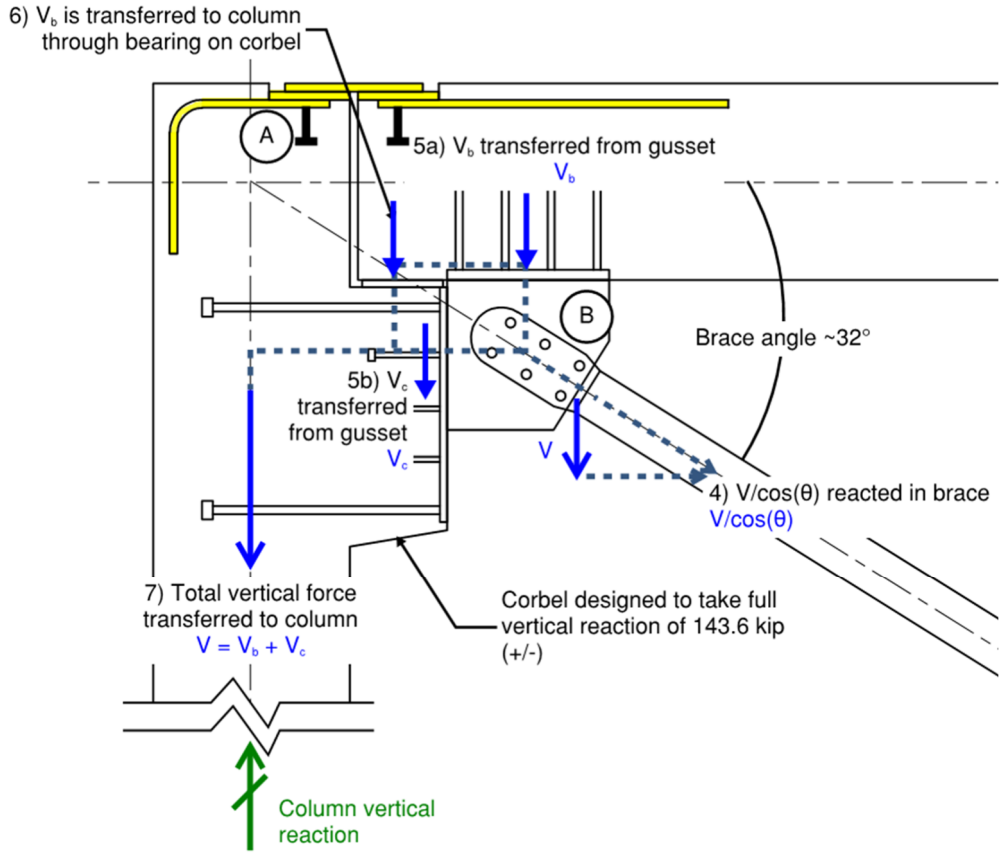

Figure 14: Vertical load path for beam-column connections, brace in tension

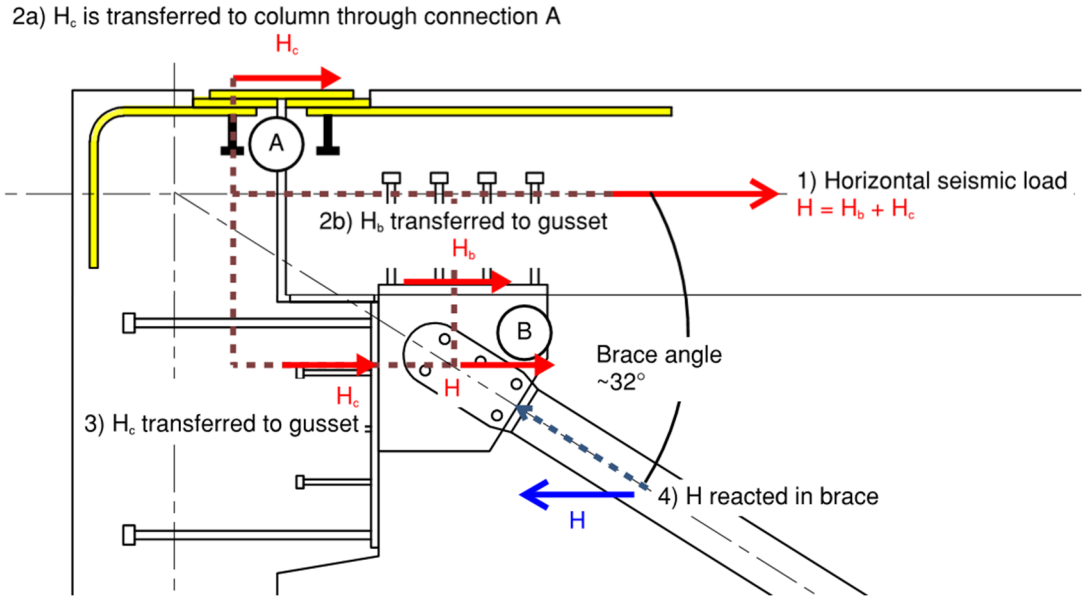

Figure 15：Horizontal load path for beam-column connections, brace in compression

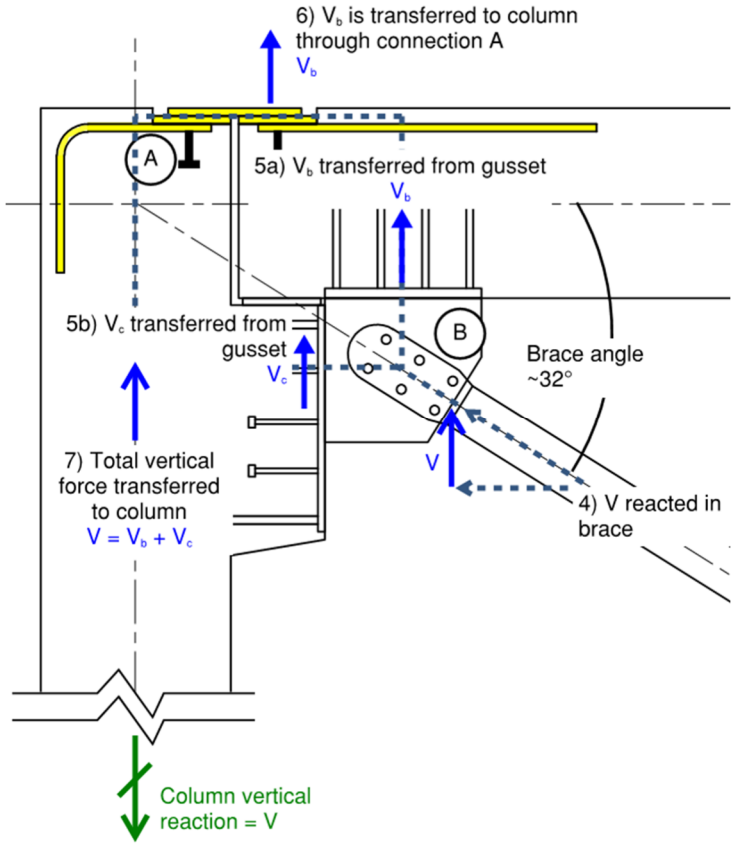

Figure 16: Vertical load path for column connections, brace in compression

Gusset and Jumper Plate Connection Design Methodology

The gusset plate dimensions were sized using the Uniform Force Method as it is outlined in Chapter 13 of the AISC Steel Construction Manual [20]. All relevant gusset, bolt, and weld failure modes were checked in accordance with the corresponding sections of ANSI/AISC 360-16, Specification for Structural Steel Buildings [25] using AISC Steel Design Guide 29 as direction [26]. Yield of embedded plates was checked using finite element models. Bars welded to embedded plates were designed to resist combined shear and tensile forces in accordance with ACI 318-19 Chapter 22 [14]. Details of the gusset plate design are discussed in Chapter 3.

The jumper plate connection was modified from a typical precast beam-column connection provided by Metromont. Combined shear and flexure of the jumper plates was checked in accordance with ANSI/AISC 360-16 [25]. The reinforcing bars welded to the embedded plates of the jumper connection were designed in the same manner as those incorporated in the gusset plate connection.

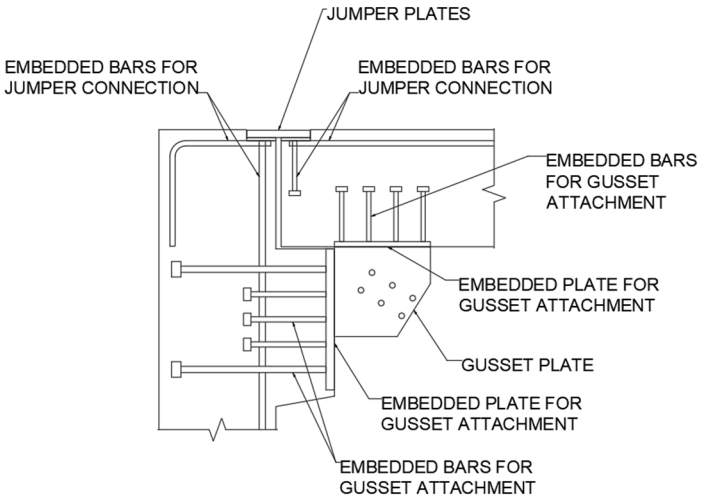

Figure 17: Gusset and jumper connection overview

CHAPTER THREE

PROTOTYPE STRUCTURE AND PRECAST FRAME DESIGN

Prototype Structure

Structure and Site

Through discussions with the advisory board for this project a parking garage structure was determined to be a good candidate structure. BRBFs could be a replacement for the shear walls typically used as the LFRS. A 4-story parking garage (3 elevated levels) was used as the prototype structure for this project. The shear walls for which the BRBFs could act as a replacement were located at the end of the drive aisles, as shown in **Figure 18**. Two bays of BRBFs per story would be required to replace one shear wall. The story height and bay width of 9'-11⅞" and 16'-0", respectively, were chosen as they were representative of an average of the three different example garage projects. The resulting angle between the brace and the beam was approximately 32°.

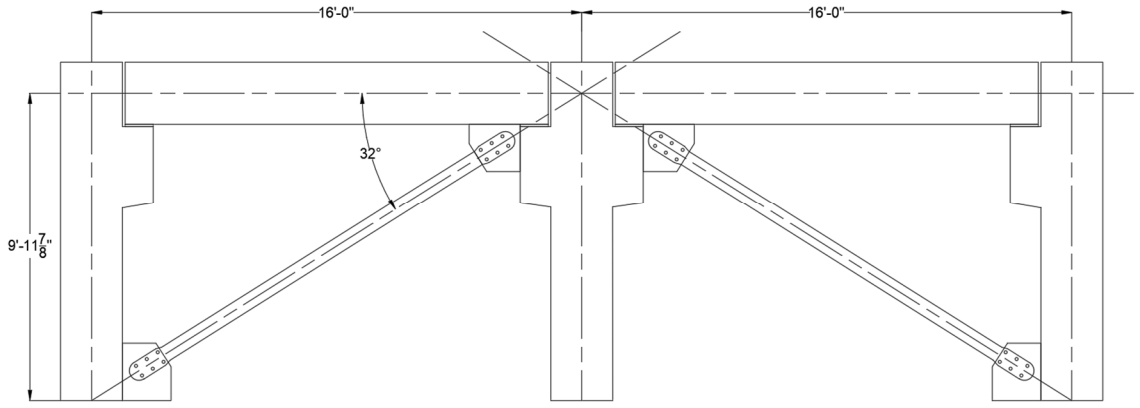

Figure 18: Typical full-scale two bay BRBF and dimensions

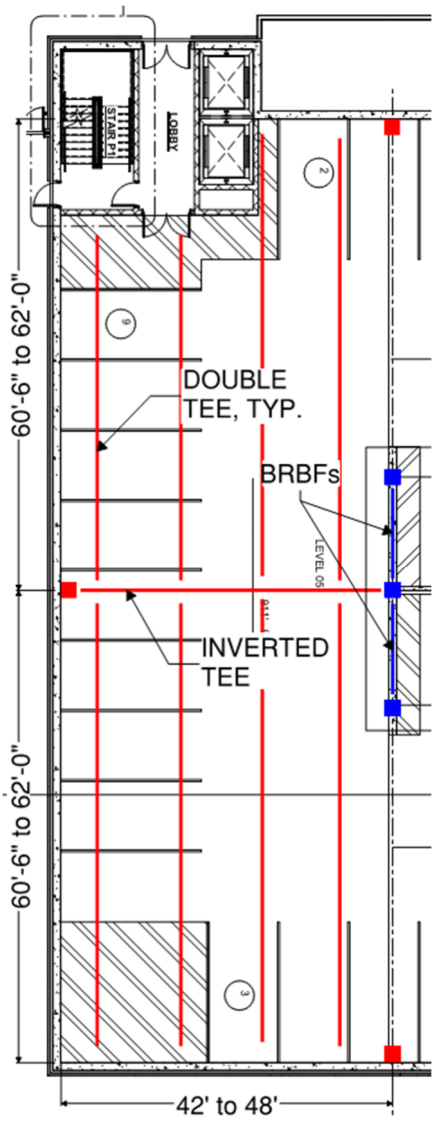

Figure 19: Floor layout of prototype structure, original drawing courtesy of Metromont

Seismic Parameters and Loads

AISC 341-16, Seismic Provisions for Structural Steel Buildings, stipulates a design philosophy for structures utilizing BRBF in Section F4 [27]. First, the factored axial demand from lateral load for the BRB must be determined using an acceptable wind or seismic design procedure. Next, the steel yielding core of the BRB should be sized for its axial load by solving for A_{ysc} in **Equation 2**.

$$P_{ysc} = F_{ysc}A_{ysc} \quad (2)$$

Where:

P_{ysc} = factored axial demand on steel yielding core

F_{ysc} = yield stress of steel yielding core

A_{ysc} = area of steel yielding core

After the area of the yielding core has been determined, the brace's adjusted strength must be determined using **Equation 3**.

$$P_{adj} = \beta\omega R_y P_{ysc} \quad (3)$$

Where:

P_{adj} = adjusted brace force

β = compression strength adjustment factor

ω = strain hardening adjustment factor

R_y = ratio of the expected yield stress to the specified minimum yield stress, F_y

This adjustment is important because all brace connections and members adjoining the brace must be designed to resist this adjusted force. The yield stress specified in ASTM standards is typically a minimum value [28], therefore not adjusting for the β and ω factors described would lead to an unconservative design.

For the purposes of testing the connection from the BRB to the precast column and beam, a hydraulic actuator was used to simulate the force-displacement behavior of a BRB (see Chapter 4 for more details). The operating load of the hydraulic actuators used for this research was a maximum of 100 kips and was limited to 90 kips for safety. This limited the adjusted brace strength that could be simulated during test. To model a larger, more representative load that a BRB in the prototype structure would experience, the test setup and specimens were scaled to one third area scale. Because of this scaling, the maximum adjusted brace force of the full-scale brace could not be more than 270 kips. This 270-kip load was greater than the required brace loads of all floors of a 6-story seismic design category (SDC) B parking garage and all 5 stories of a SDC C parking garage; these real example garages were provided by Metromont Corporation.

Through ETABS modeling, the BRB manufacturer CoreBrace determined a full-scale brace size and overstrength factor that would have a maximum adjusted brace strength of 270 kips in compression at the elongation caused by 2% story drift. This full-scale brace was used A36 steel and was determined to have 170 kips of force at yield, a yielding core area of 4.05 in^2, and a yielding core length of 112.41 in.

This full-scale model was used as qualification for the third-scale model. It was assumed that both scales would achieve the same strain levels, have the same overstrength factor, and the same material properties. All other properties (force, geometry, etc.) were assumed to be scaled such that equivalent stresses were achieved between the scaled and full-scale models. These assumptions were justified because the

specimen was not physically built, but instead only the force-displacement relationship needed to be simulated through use of hydraulic actuators.

A backbone of the hysteresis curve (in terms of force and brace displacement) was provided by CoreBrace for the full-scale brace, see **Figure 20**. This backbone curve included four significant points: force and elongation at yield in tension (P_{yt}, Δ_{byt}), force and elongation at yield in compression (P_{yc}, Δ_{byc}), force and yield in tension at 2% story drift (P_{ut}, Δ_{bmt}), and force and yield in compression at 2% story drift (P_{uc}, Δ_{bmc}).

Because the material properties were assumed to be the same between the scaled brace and the full-scale brace, the force and elongation of the third-scale brace at yield (P_{yt}, Δ_{byt}, P_{yc}, Δ_{byc}) were one-third of the force and elongation of the full-scale brace at yield. Because brace area was assumed to be exactly one-third of those in the full-scale brace and both cores were assumed to achieve the same strain level at 2% story drift, the force and elongation of the third-scale brace at 2% story drift (P_{ut}, Δ_{bmt}, P_{uc}, Δ_{bmc}) were one-third of the force and elongation of the full-scale brace at yield.

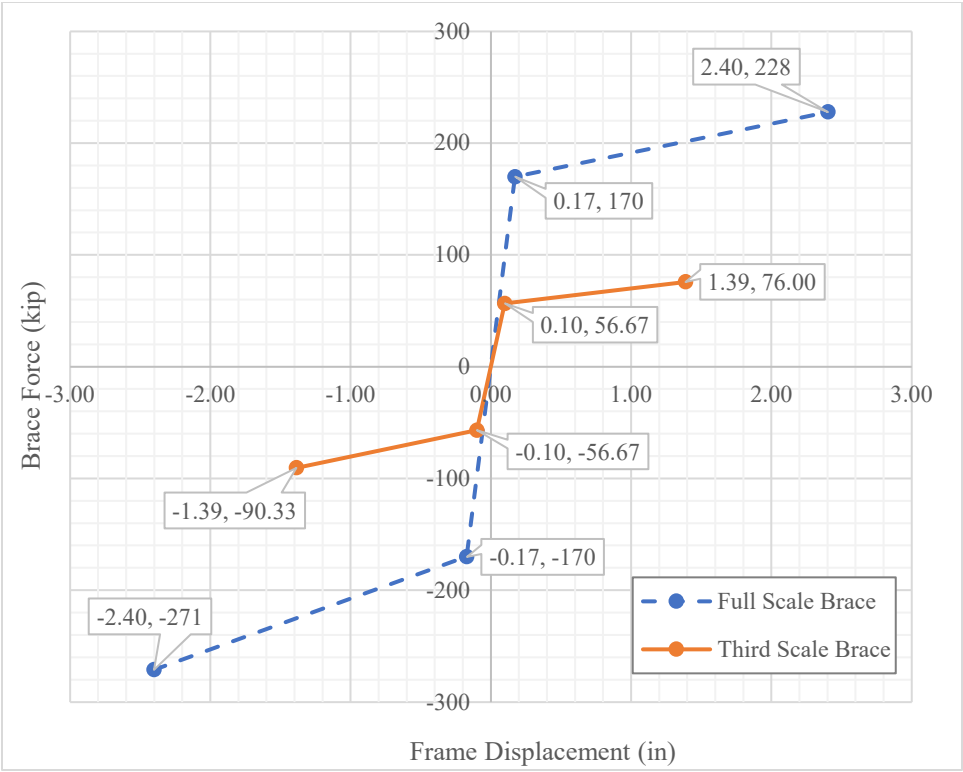

Figure 20: Full-scale backbone of hysteresis provided by CoreBrace and derived scaled backbone curve

Gravity Loads

As previously stated, it was assumed that the BRBs and gussets would be installed in the structure after the floor topping had been poured and cured. This would prevent as much gravity load transfer to the gusset and brace as possible. Gravity load on the beam in the prototype structure was relatively low as the beams in the BRBF ran parallel to the floor double-tee beams, making its tributary area very small (see **Figure 19**). Though there would still be a large amount of gravity load on the column in the event of large lateral loads being applied to the structure, gravity load was neglected in the experimental setup. The primary focus of the experimental work was to characterize load path in the connection, which would be largely unaffected by gravity load in the column. This

permitted the specimen to be tested horizontally. Therefore, gravity load was quantified for the purposes of designing the precast components, but not applied during testing.

A summary of the tributary widths and areas and dead and live loads for the structure is contained in **Table 1**. All tributary areas and dead loads were determined from construction of the example garages provided by Metromont Corporation. The value of S_{DS}; the design; 5% damped, spectral response acceleration parameter at short periods as determined using ASCE 7-16; used in conjunction with load combinations from ASCE 7-16 was taken from the SDC C example garage as it provided the worst-case dead load. Live load was also determined using ASCE 7-16 [29].

Table 1: Summary of tributary widths and areas and dead and live loads

Tributary Width or Area	
Beam Tributary Width	24.25 in
Column Tributary Area	4117.5 ft^2
Dead Load	
Weight of topped double-tees	75 psf
Self-weight of beam and column	150 pcf
S_{DS} from SDC C garage to adjust dead load	0.289
Live Load	
Passenger vehicles only	40 psf

When calculated, the gravity load that would pass through the corbel (1.15 kip) was less than 18% of the vertical portion of the brace load that was estimated to pass through the corbel by the UFM for the lowest load level that would be executed (6.50 kip) and less than 6% of the highest load level that would be executed (20.80 kip). This

was further validation that it was reasonable to neglect gravity load for the objectives of this test.

Precast Frame Design

As previously described, a scale factor of 1/3 was applied to the seismic load so that a more realistic BRBF could be simulated in test. To maintain equivalent stresses between the full-scale and scaled structures a variety of scale factors for geometry and load were derived, these scale factors are presented following in **Table 2**.

Table 2: Scale factors to maintain equivalent stresses between full-scale and scaled models

Area Scale Factor	$\frac{1}{3}$	**Axial/Shear Force Scale Factor**	$\frac{1}{3}$
Length/Width Scale Factor	$\frac{1}{\sqrt{3}}$	**Moment Scale Factor**	$\frac{\sqrt{3}}{9}$

Because the frame was designed as pinned, only a partial frame was tested. **Figure 21** shows the tested partial frame in the context of the full frame. The members of this frame were scaled by the factors shown in **Table 2**, but were of complete scaled length, meaning that a realistic "pinned" column base connection could be tested and realistic beam and column curvature could be monitored.

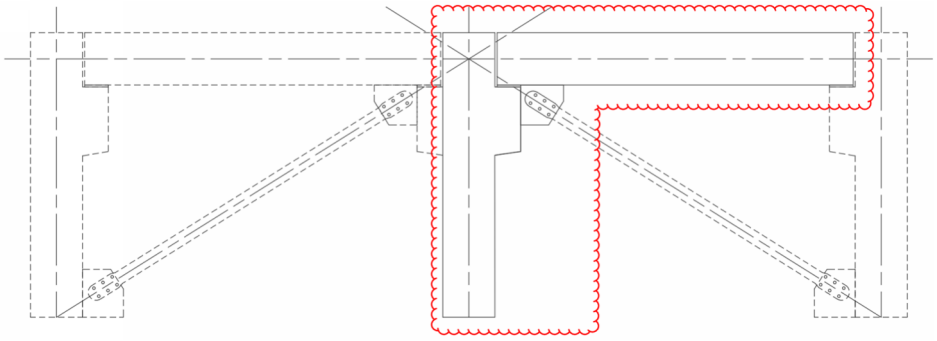

Figure 21: Beam, column, and gusset plate tested with respect to full frame

Beam Design

The beam was designed to meet the requirements of ACI 318-19 Chapter 18.6, "Beams of special moment frames," and detailed in accordance with ACI 318-19. Chapter 25 [14]. Though this frame should have, in theory, been more flexible and not have been required to transmit large moments, this design process was chosen as it provided the most ductility and conservatism for the initial prototype. The resulting scaled beam design specified a 14"x14" cross-section using Grade 60 reinforcing bars and 6000 psi concrete. Typical reinforcing scheme is shown in **Figure 22**.

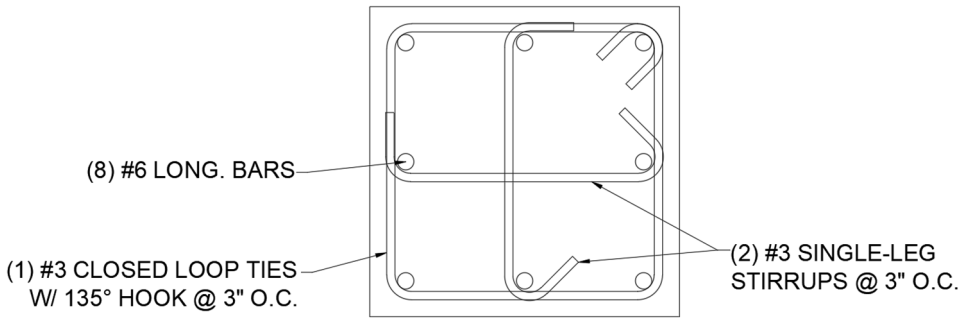

Figure 22: Cross-sectional view of typical beam reinforcing

Column and Corbel Design

The column would have three corbels in the full prototype frame and would be subjected to biaxial bending due to gravity load from members that framed into it, see **Figure 23**. This was neglected as it was outside the scope of this work. The effect of the interaction of the two braces on the column was also neglected in design as only one brace would be simulated in test.

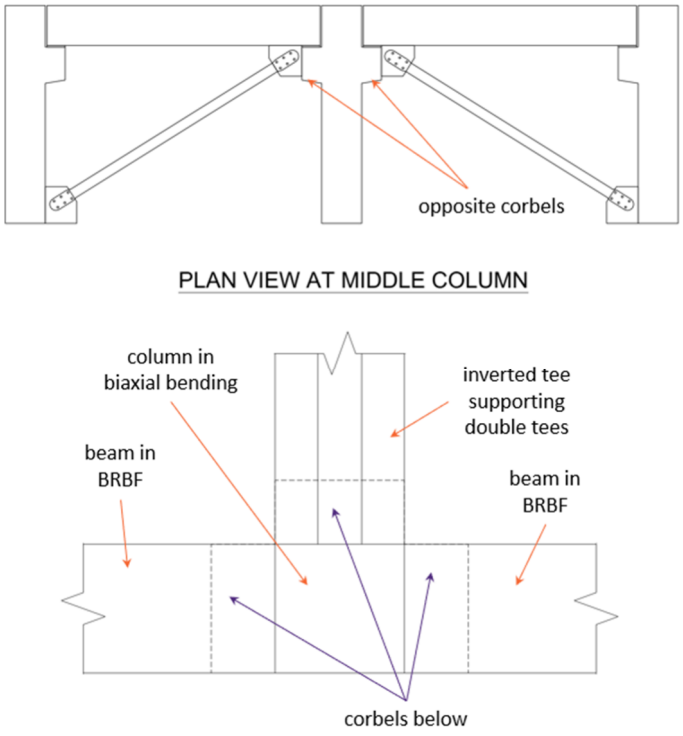

Figure 23: Members framing into middle column

The column was designed to meet the requirements of ACI 318-19 Chapter 18.7, "Columns of special moment frames," and detailed in accordance with ACI 318-19 Chapter 25 [14]. The resulting scaled column design specified a 14"x14" cross-section using Grade 60 reinforcing bars and 6000 psi concrete. Typical reinforcing scheme is shown in **Figure 24**.

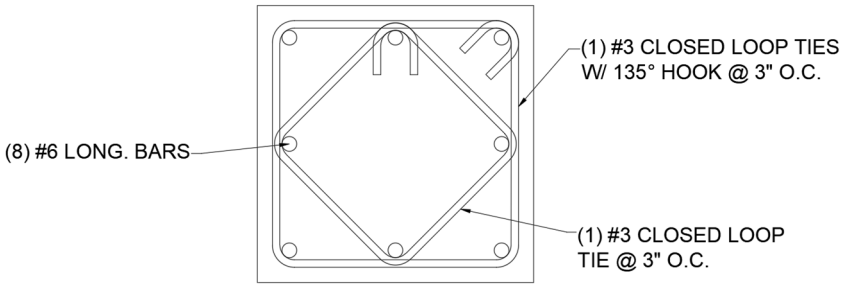

Figure 24: Cross-sectional view of typical column reinforcing

The corbel was designed to meet the requirements of ACI 318-19 Chapter 16.5, "Brackets and Corbels," and detailed in accordance with ACI 318-19 Chapter 25 [14]. The factored normal load on the corbel was greater than the factored shear load, in violation of Sec. 16.5.1.1. The requirement of Sec. 16.5.1.1 is stipulated because the cantilever beam method of design has only been validated for cases where factored normal load is less than factored shear load. It was of interest to the advisory board to use the cantilever beam method of design for this frame because it is more commonly used than the strut-and-tie method (ACI 318-19 Chapter 23) that is required if Sec. 16.5.1.1 is violated. Though not the focus of this thesis, this test could act as a qualification for the cantilever beam method in a case where the factored normal force is greater than the factored shear force. The scaled corbel design specified was 1'-5⅝" deep, used (4) Grade 60 #6 primary tension reinforcing bars top and bottom of corbel, and 6000 psi concrete.

Gusset and Jumper Plate Connections

The gusset plate required was ½" thick and made of A572 Grade 50 steel with dimensions shown in **Figure 25** below. The weld size required at both the beam and column interfaces was the minimum recommended fillet weld size from the AISC Steel Construction Manual [20] of 3/16" using 80 ksi electrodes. On the day of fabrication, however, only 70 ksi electrodes were available and the welds fabricated were 3/8" not 3/16". These deviations ultimately added more conservatism to the system and thus were deemed acceptable. The hole size and pattern in the gusset was designed to match the size and pattern typically prescribed by CoreBrace.

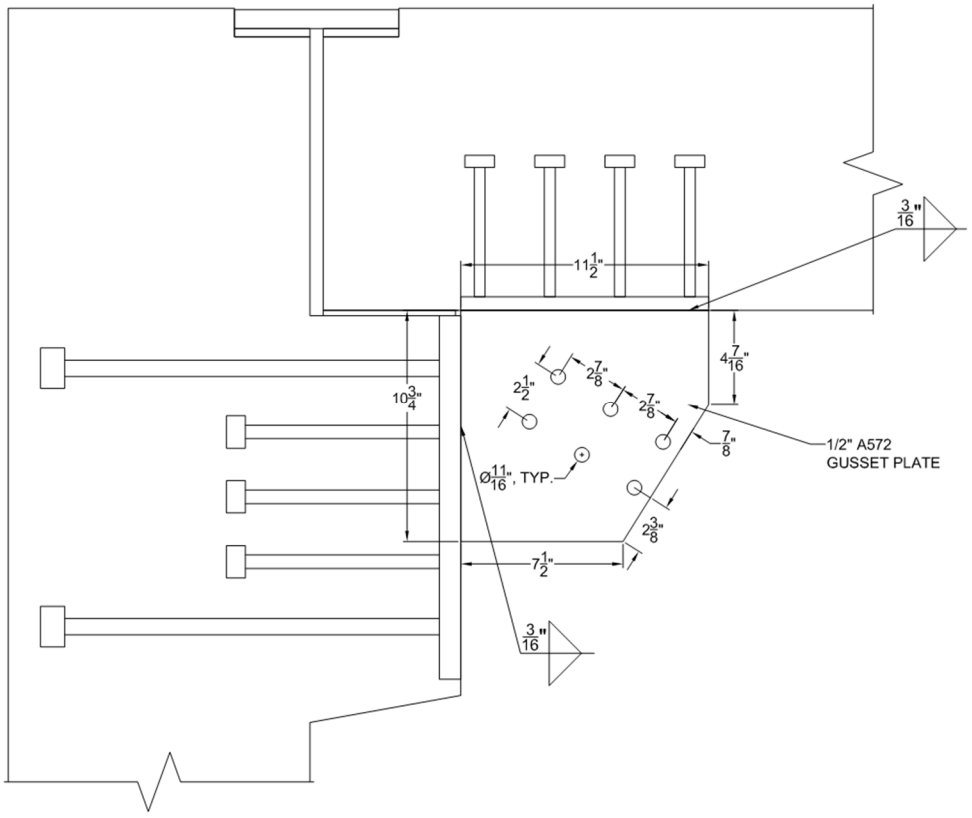

Figure 25: Gusset plate dimensions and welds

The jumper plate connection between the beam and column was composed of two embedded plates (⅜" thick) and three jumper plates (⅞" thick) that were welded to both embedded plates. All plate steel in this connection was specified as ASTM 572 Grade 50. The welds along jumper plate edges were specified as 7/8" fillet welds using 80 ksi electrodes. The design prescribed is shown in **Figure 26**. 80 ksi electrodes were unavailable during fabrication, so 110 ksi electrodes were used instead. The column embedded plate was warped such that there was a ½" difference between the height of the column and beam embedded plates, see **Figure 27**. This was accounted for by using steel shims below the jumper plates with gaps and using a fillet weld with unequal legs. The

root of the weld was adjusted for this geometry and the additional conservatism added by the 110 ksi electrodes made this design acceptable.

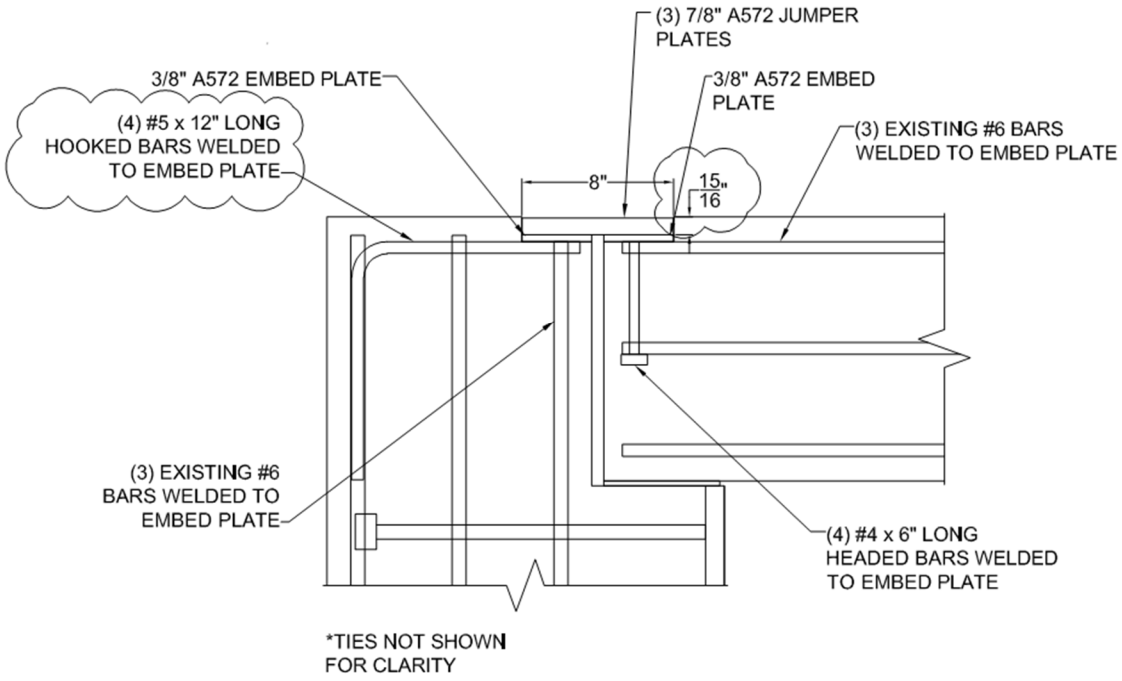

Figure 26: Jumper plate connection detail

Figure 27: As-built condition of jumper plate connection

Precast Connections

A widely used precast pinned column base connection was chosen for this frame. This connection consisted of a base plate that was embedded into the column base using reinforcing bars welded to the plate. The base plate was flush with the outside dimensions of the column, so the four anchor bolts were inset in pockets, see **Figure 28**. The base plate was designed using Chapter 6.11 of the PCI Design Handbook, 8th Edition [6]. The lapped splices between the reinforcing bars welded to the base plate and the longitudinal bars that had to be terminated above the bolt pockets were designed to meet the requirements of ACI 318-19 Section 25.5.2 [14]. Though this was a pinned connection, it would inevitably resist some moment. The bolts were oversized to ensure that the bolts would not fail due to this moment before the peak frame displacement was reached. The base plate used ASTM 572 Grade 50 steel and was 1¼" thick, the reinforcing bars were Grade 60, and the bolts were 1¼" in diameter and of A490 grade. The same connection was used to connect the beam to its actuator.

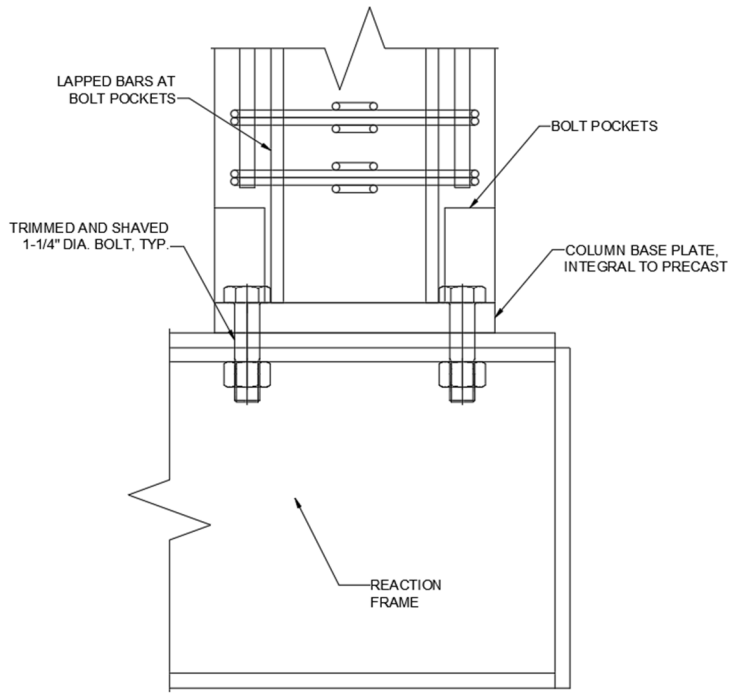

Figure 28: Pinned column base connection

Typically, bolt pockets would be grouted solid after the column is installed and the bolts or threaded rods have been tightened sufficiently. Grouting the bolt pockets for this test would have made removal of the specimen difficult, so the column base was designed not to account for the shear strength of the grout. Because this strength was not accounted for in design, the pockets were left ungrouted on both the column and beam connections. Final reinforcement details are included in Appendix A.

CHAPTER FOUR

EXPERIMENTAL PROGRAM DESIGN

Overview

A partial frame consisting of a beam and single column was deemed to be representative of the whole prototype frame as the prototype was assumed to be pinned. Because it was cost-prohibitive to test using a physical BRB, the behavior of a BRB was simulated using a servo-controlled hydraulic actuator, referred to as the "brace" actuator. This actuator and second actuator, referred to as the "beam" actuator, that induced frame horizontal displacement subjected the precast specimen to a predetermined hysteresis over the course of the test.

This chapter first presents the reaction frame and specimen restraints used during the test. Next, the connections from the test specimen to the beam and brace actuators are described. After the instrumentation plan is discussed. Finally, the test procedure is presented including the derivation of the hysteresis curves used to prescribe the beam displacement and brace force.

Reaction Frame and Specimen Restraints

A frame of sufficient size and capacity was not already available among Clemson University resources, so one was designed for this project and to support similar research in the future. **Figure 29** below shows the frame with precast specimen installed.

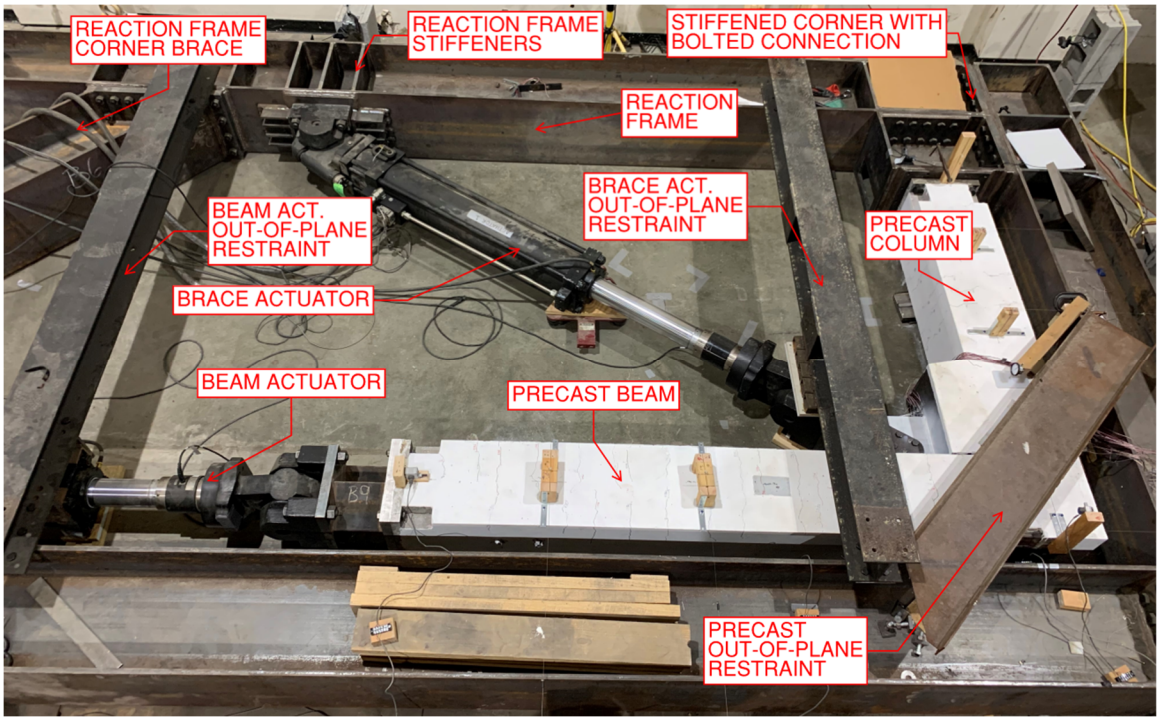

Figure 29: Reaction frame with precast specimen installed

The typical section size was an HP18x135 and stiffeners were added at points where concentrated loads were applied to the frame. The corners were joined by moment-resisting bolted end plate connections for ease of disassembly and reassembly. The maximum utilization ratio for flexure of any frame member from SAP2000 analysis inducing the maximum test loads was 0.432. The maximum displacement under test loads was designed to be 0.6" at the brace actuator's attachment to the frame. The displacement under test would be found to be slightly higher likely due to oversize of frame bolt holes.

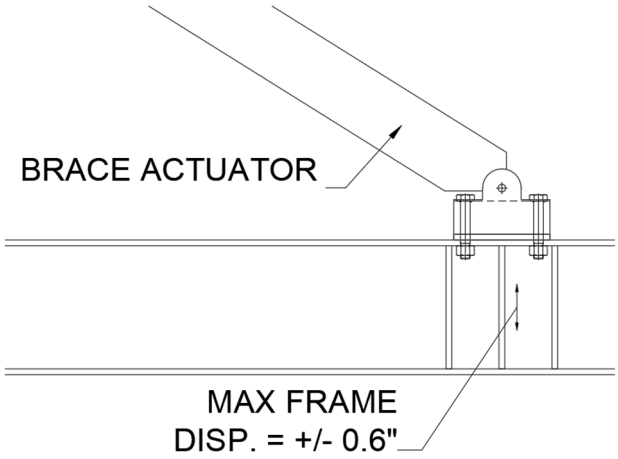

Figure 30: Location of theoretical maximum frame displacement

Three out-of-plane (OOP) restraints were provided to ensure that the specimen could not move significantly in the vertical direction during test: a corner brace against the precast specimen itself, a brace on the beam actuator, and a brace on the brace actuator. These restraints were in contact with the component they were to restrain, but the component could slide using plastic sheets with low coefficients of friction and grease.

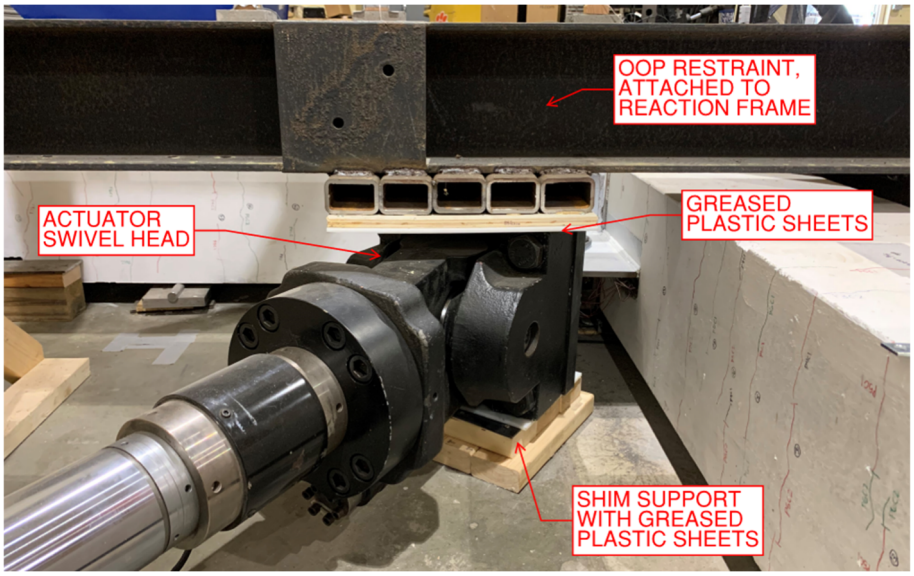

Figure 31: Brace actuator OOP restraint

The precast specimen itself was supported using greased steel rollers shimmed to the correct height.

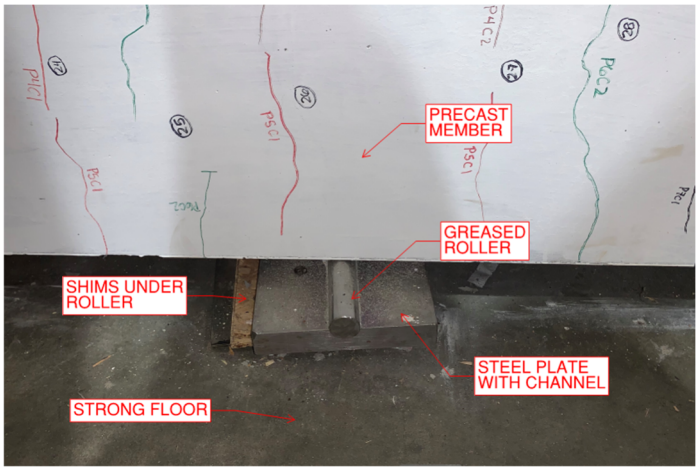

Figure 32: Roller supports for precast specimen

Specimen to Actuator Connections

As previously described, the beam and column were attached to the beam actuator and reaction frame, respectively, using a typical pinned column base connection. The beam required an adapter to attach to the hydraulic actuator as they possessed different bolt patterns. This adapter consisted of a short W8x35 section with two 1¼" thick steel plates welded to its ends.

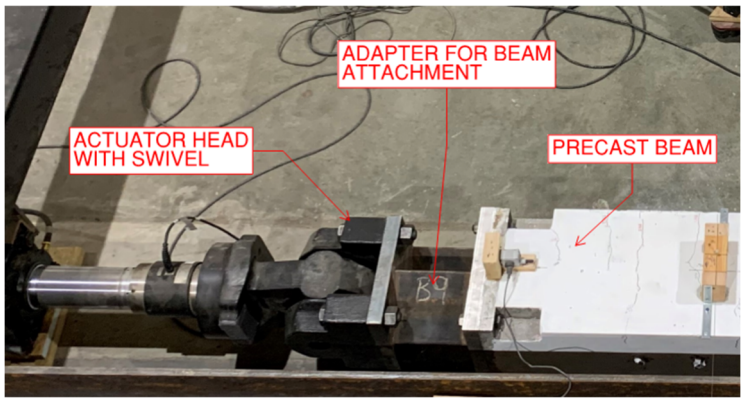

Figure 33: Adapter for attachment of precast beam to hydraulic actuator

The column base plate was warped and had a ⅛" slope over its depth, see **Figure 34**. This caused the two bolts closest to the floor to be in contact with the frame while the two bolts furthest from the floor were not in contact. To rectify this, two ⅛" washers were placed between the base plate and the frame at the top two bolts. This ensured contact in the immediate vicinity of the bolt hole.

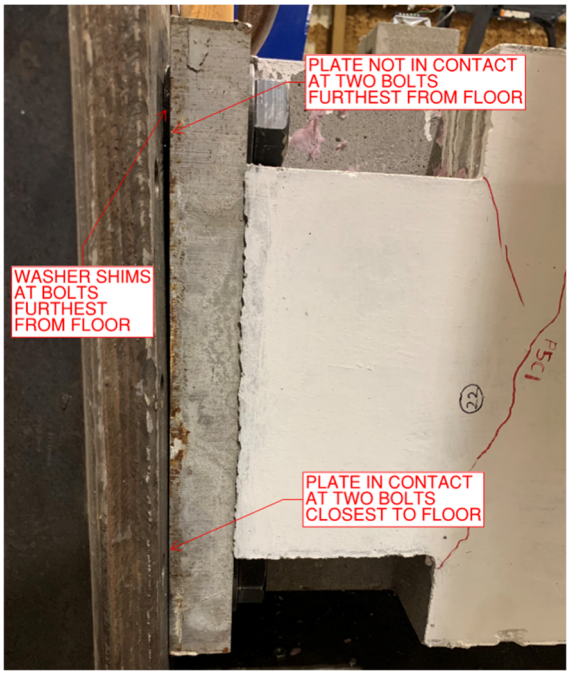

Figure 34: Warping in column base plate

CoreBrace provided a bolt layout and spacing for the full-scale brace that was typical of what is usually prescribed. This layout was scaled to ⅓ area scale. The lug connector from the gusset plate to the brace was designed to put the bolts into double shear and have a large strength margin with respect to the highest brace force that was tested.

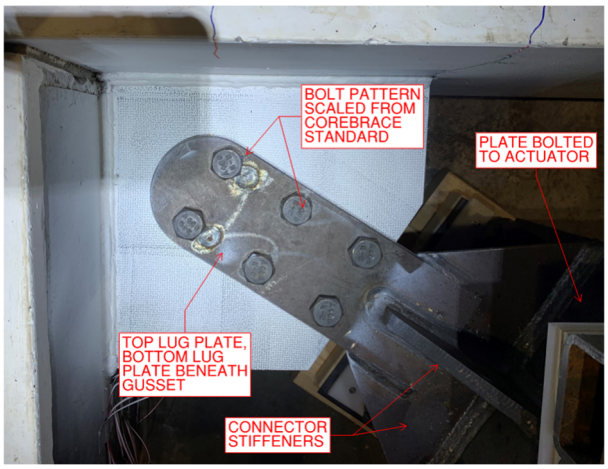

Figure 35: Lug connector from gusset to brace actuator

Instrumentation

Instrumentation for this test was focused on gathering data from four areas of the test specimen and test setup: the gusset plate, the corbel reinforcing bars, the precast frame, and the reaction frame. An overview of the instrumentation plan is shown in **Figure 36**.

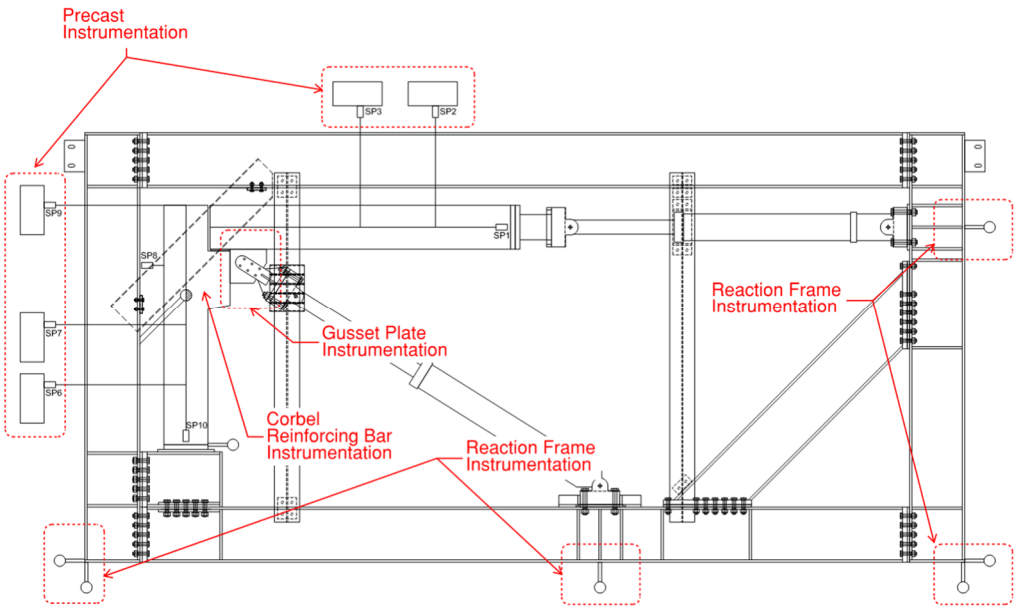

Figure 36: Test instrumentation overview

Gusset Plate Instrumentation

Because the validation of the force distribution between the gusset's connected edges was a main objective of this work, rosette strain gauges were applied along the connected edges. Rectangular rosette gauges allowed for the determination of normal and shear strains along the connected interfaces. The gauges were chosen to be similarly located to other gusset plate tests in the literature that also sought to quantify this force distribution [13, 21, 22]. The gauges were applied to the underside of the plate so they would not interfere with digital image correlation measurements taken on the front of the gusset plate. The application locations are shown in **Figure 37**.

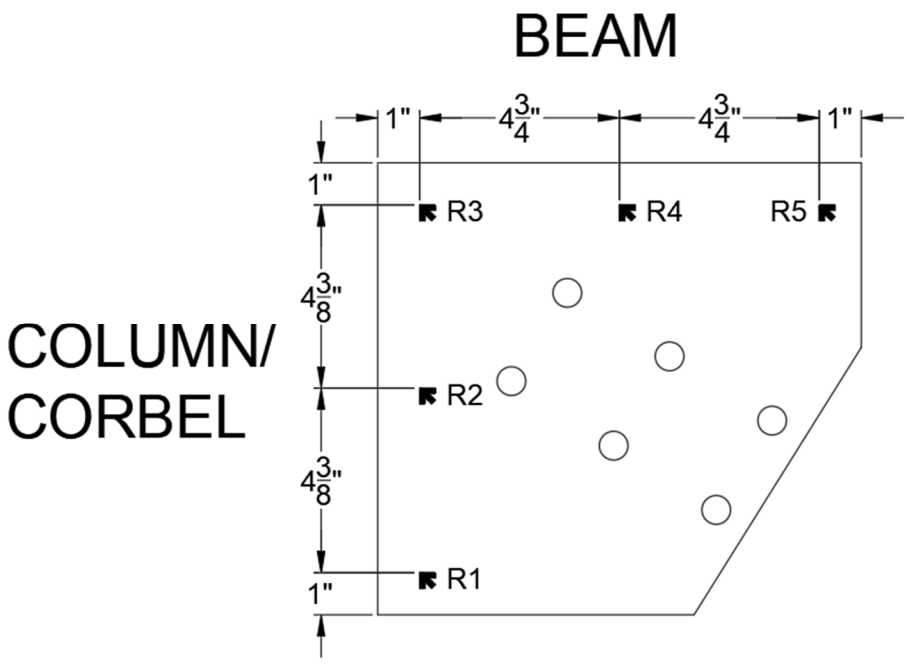

Figure 37: Location of rosette gauges along gusset plate connected edges

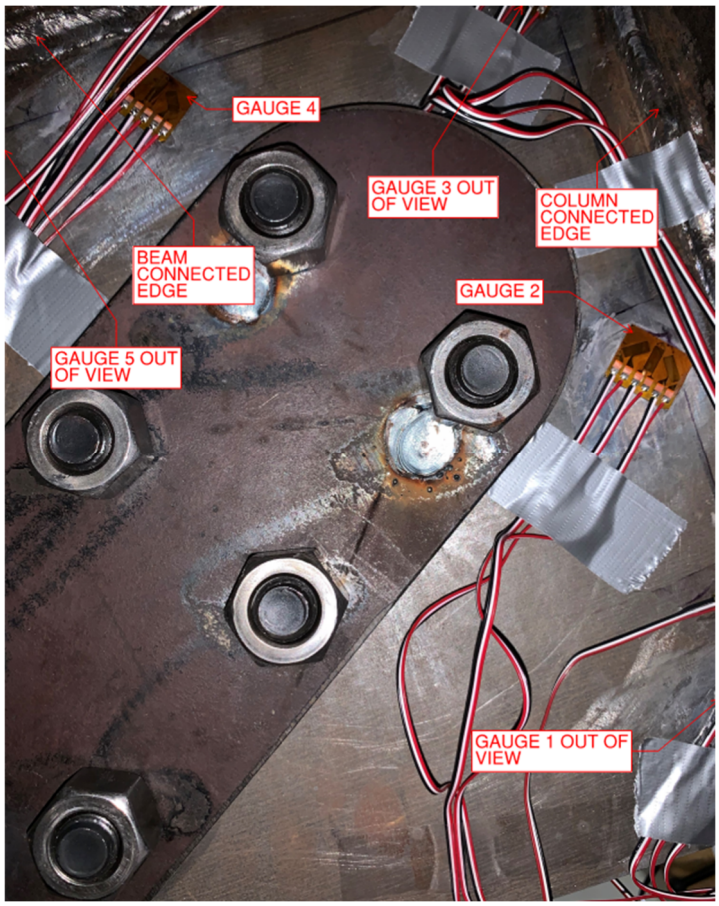

Figure 38: Gauges installed on the underside of the gusset plate

Digital image correlation is a relatively new non-contact strain and displacement measurement technology. 3-D digital image correlation was set up for this test in collaboration with the mechanical engineering department at Clemson University and is not the focus of this thesis. For the purposes of this thesis, the DIC system was used to monitor out-of-plane displacement of the gusset plate during testing.

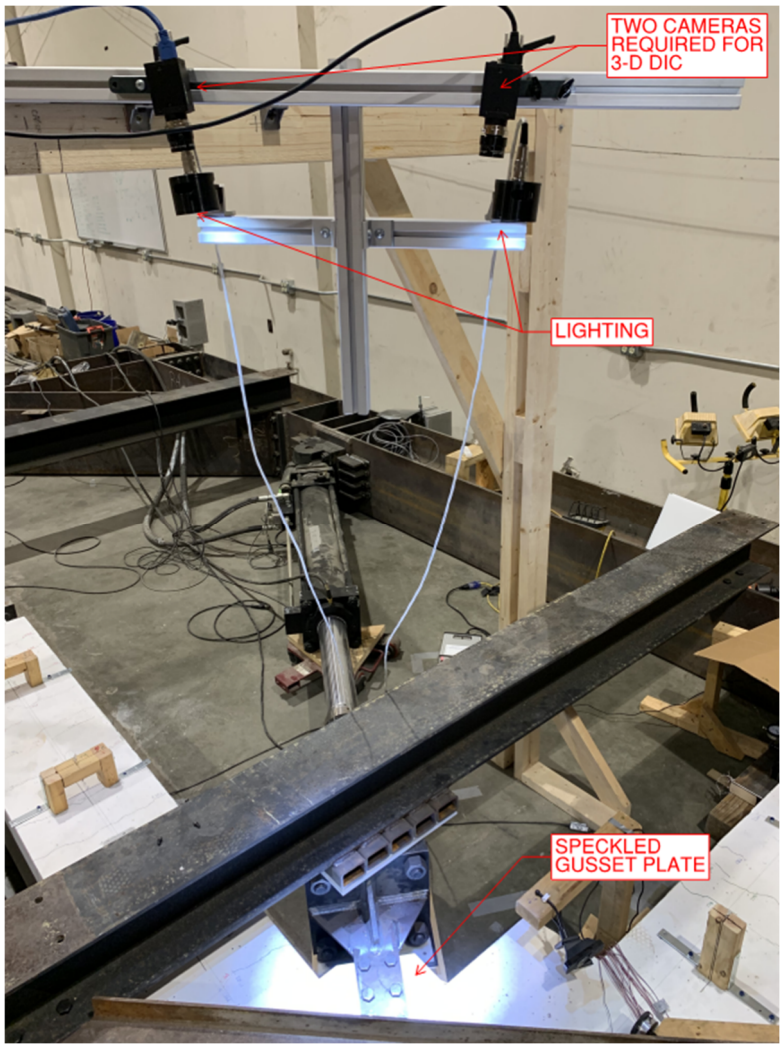

Figure 39: DIC setup

Corbel Reinforcing Bar Instrumentation

During design, the corbel primary tension reinforcing bars were determined to be the weakest link if the assumed load distribution was correct. A linear strain gauge was applied to each of the eight corbel bars at the critical section of the corbel, the theoretical point of highest stress, to determine if any of the bars yielded during testing.

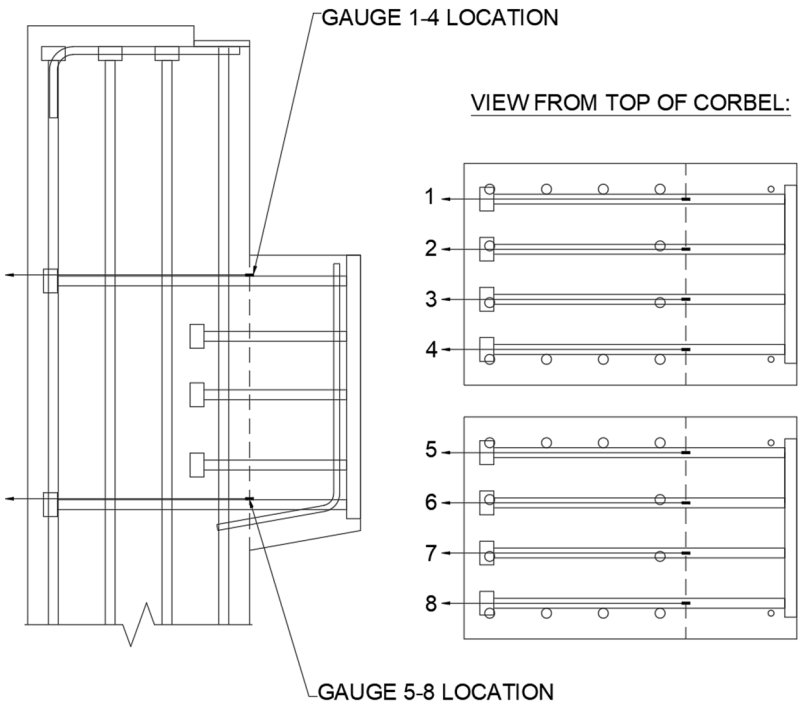

Figure 40: Strain gauge locations on corbel reinforcing bars

Figure 41: Strain gauge applied to corbel reinforcing bar prior to concrete pour

Precast Instrumentation

Each of the two servo-controlled hydraulic actuators was equipped with an integrated load cell and LVDT. These allowed for direct monitoring of internal force in the precast beam and in the simulated brace. The precast frame displacement was analogous to the displacement measured by the LVDT integrated in the beam actuator. See **Figure 29** for locations of beam and brace actuators.

Curvature of the beam and column were monitored using string potentiometers. String potentiometers 1 and 10 were placed along the longitudinal axes of the beam and column and monitored axial deformation. String potentiometers 6-9 were placed perpendicular to the column longitudinal axis at quarter points along the column height to measure curvature. String potentiometers 2 and 3 were placed perpendicular to the beam longitudinal axis at the first two quarter points along the beam length to measure curvature. String potentiometer locations are shown in **Figure 43**. Stroke lengths of the sting potentiometers used ranged from 4.75”-25”. The sensor accuracy of the string potentiometers was 0.25% of their total stroke.

Because of the limited number of channels available in the data acquisition system, voltage measurements for string potentiometers 1-3 were taken manually using a multimeter. These measurements were taken at the tension and compression peak of each cycle, as well as at all points where the slope of the hysteresis curve changed.

One dial gauge was placed at the column base to monitor the slip of the column base, see **Figure 42a**. Another dial gauge was placed at the ⅝ point of the column (measured from its base) to monitor the OOP movement of the precast specimen, see

Figure 42b. All dial gauges used in this test had 1" strokes and 0.01" graduations and were all recorded using cameras mounted with view of their faces.

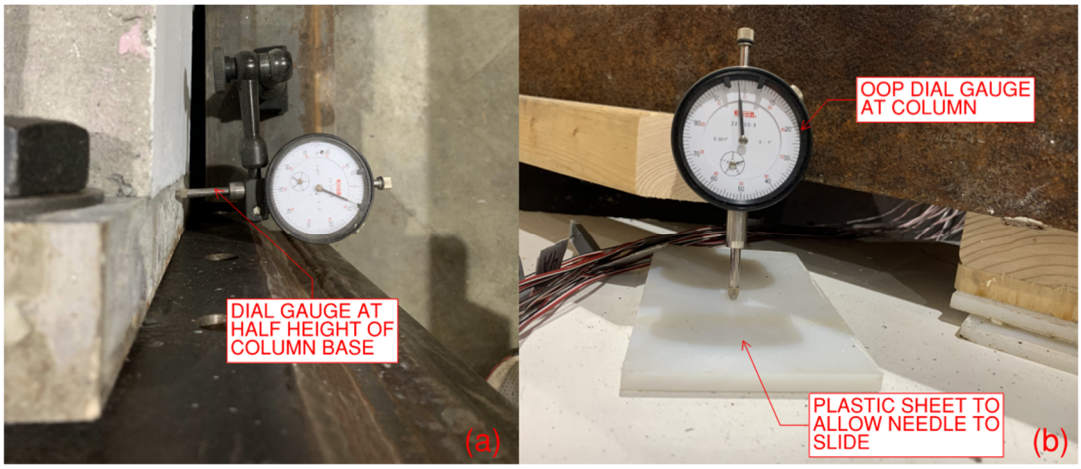

Figure 42: (a) slip dial gauge at column base, (b) OOP dial gauge at column

The precast beam and column were whitewashed to make cracks that formed during testing more visible. After each cycle was completed, the accessible sides of the beam and column were inspected using a flashlight. The length and width of any cracks found during this inspection was measured. After the cracks were measured the crack itself was darkened by marking it. The procedure and cycle number were marked next to the crack. The crack progression for the beam and column can be viewed in Chapter 5.

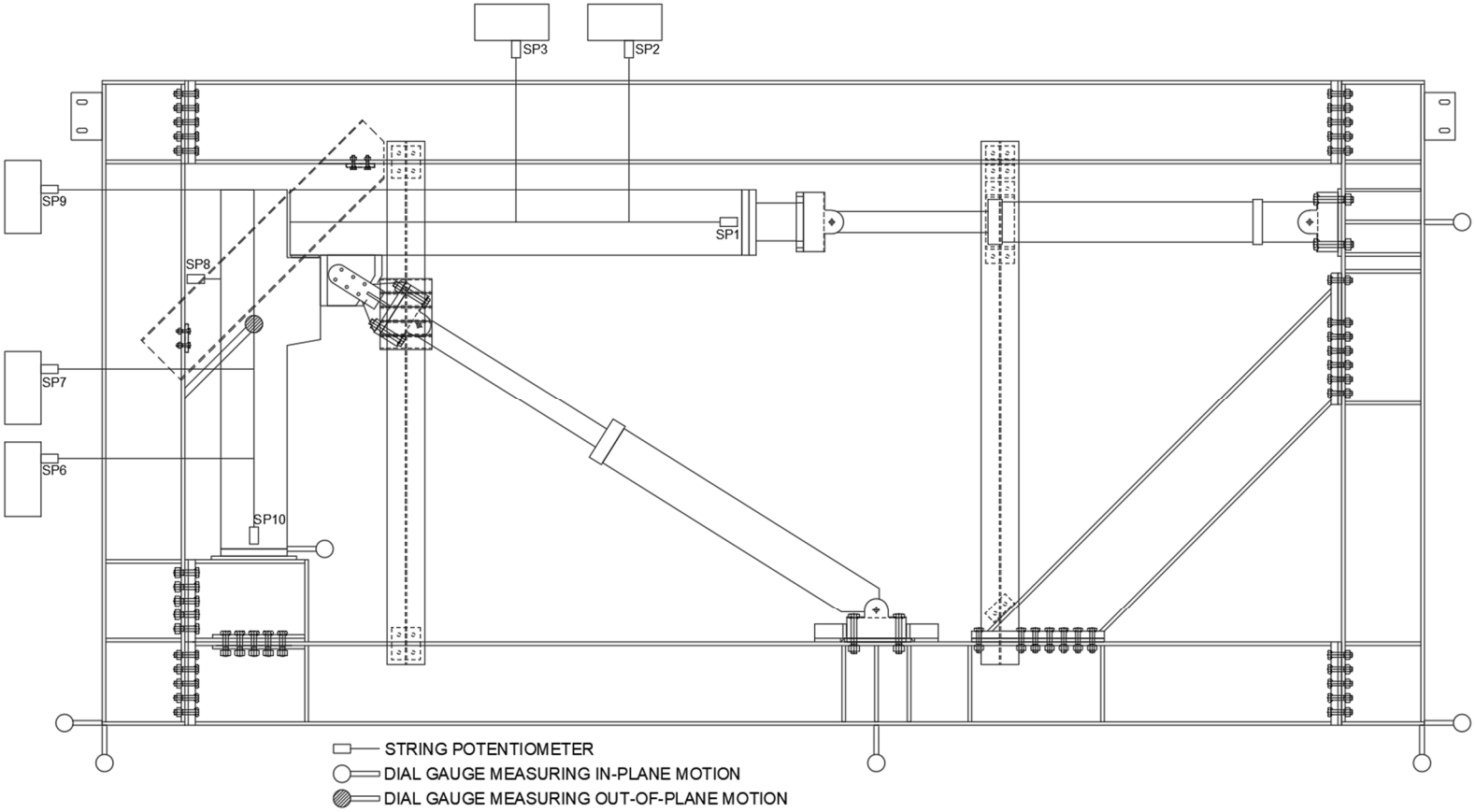

Figure 43: String potentiometer and dial gauge layout

Reaction Frame Instrumentation

The frame in-plane movement was monitored through use of dial gauges of the same stroke and graduation as previously described. These gauges were placed at the free corners of the reaction frame and at the actuator to frame attachment points. Frame dial gauge locations are shown in **Figure 43.**

Test Procedure

Control Hysteresis

Because it was cost-prohibitive to incorporate an actual BRB in this experimental program, the behavior of a BRB was simulated with a servo-controlled hydraulic actuator. Therefore, it was necessary to predict the hysteretic response that the scaled brace would experience. CoreBrace provided a backbone curve of the hysteresis for the full-scale brace that was scaled in the process described in Chapter 3. To predict the full hysteretic response of an untested brace, a procedure involving strain levels and multiple stress-strain relationships was developed based on a procedure detailed by Coy [15]. The goals of this procedure were two-fold: estimate the response of the brace outside the peaks of each loop and estimate the peak load at intermediate strain values outside the provided values at brace yield and 2% story drift.

This methodology was based on the cyclic stress-strain behavior from Kaufmann et al. [31] and known strain hardening relationships [32, 33]. It was validated on tests of CoreBrace G-series braces performed by Newell et al. [4]. Comparison between the test hysteresis and the predicted hysteresis indicated that this method of prediction yielded a satisfactory level of accuracy in predicting strain hardening behavior and the shape of the

hysteresis loops at different strain levels, see **Figure 44**. The full methodology can be viewed in **Appendix A**.

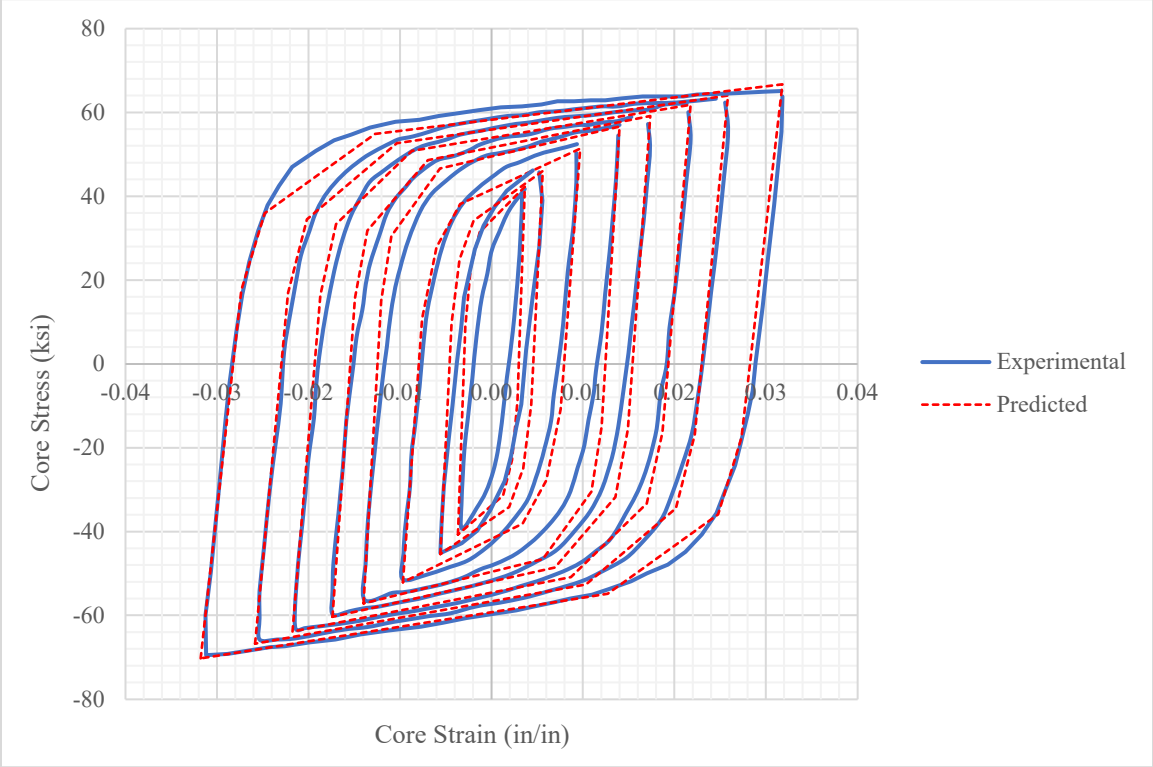

Figure 44: Actual and predicted stress-strain relationship of yielding core for specimen 3G [4]

This process was used to drive hysteresis loops for the scaled brace at the following fractions of the strain in the brace at 2% story drift: ⅛, ¼, ½, ¾, and 1. The "loops" for half yield and yield strain of the brace were also included in this hysteresis but did not need to be determined by this procedure as the brace would remain elastic and unload back to its starting point. These loops were chosen as they corresponded most closely with the first three steps of the loading sequence specified in Section K3.4c of AISC 341-16 for the qualification of buckling restrained braces by cyclic tests [27]. The last three steps of this loading sequence, inducing strains greater than those required to

achieve a 2% story drift, could not be achieved without making the scaling of the precast specimen significantly smaller. Additional scaling was not ideal because scaling reinforcing bar sizes would be difficult, so testing up to 2% story drift only was deemed acceptable. Four additional strain levels between zero and 2% story drift; half yield and ⅛, ¼, and ¾ of 2% story drift; were added to study the behavior of the system at a greater number of points. The hysteresis derived for the scaled specimen is presented below in **Figure 45**.

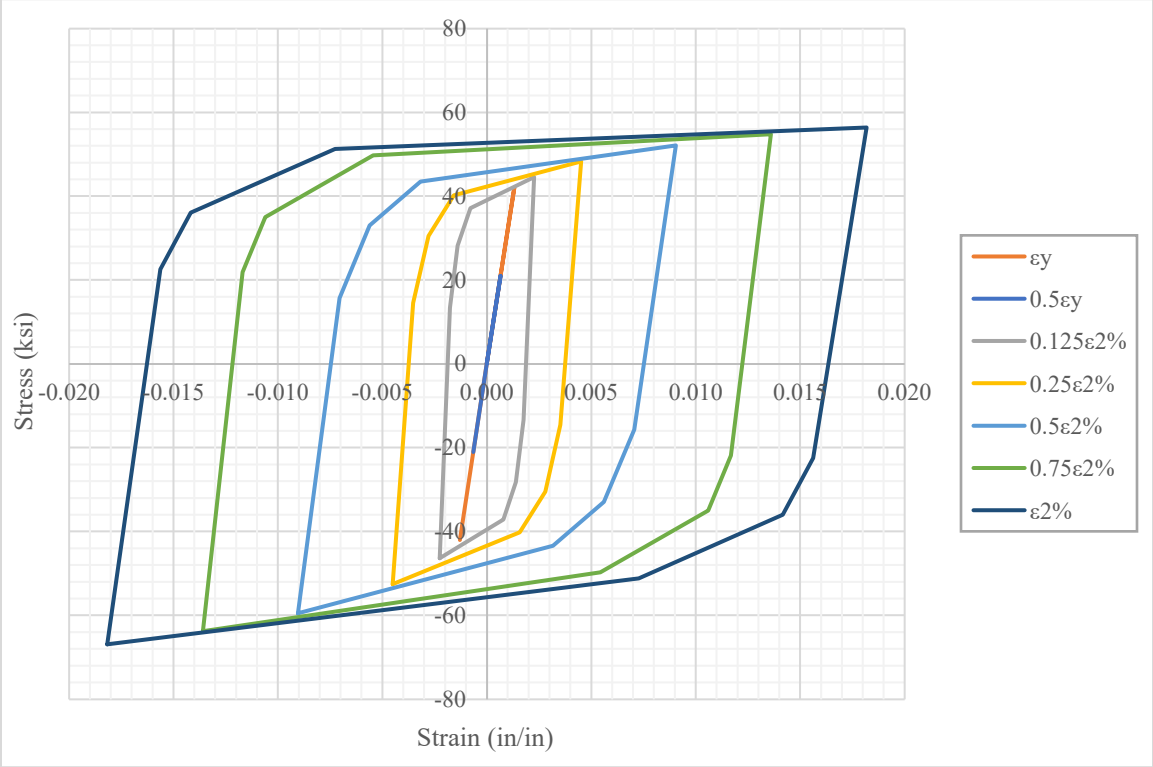

Figure 45: Predicted stress-strain relationship for yielding core of scaled brace

Test Execution

To execute the derived control hysteresis, the brace hysteresis was converted to terms of the frame displacement by the following equations:

$$P_{brace} = A_{sc}\sigma_{brace} \quad (4)$$

Where:

P_{brace} = force in brace corresponding to a given brace stress, kip

A_{sc} = area of brace yielding core, in^2

σ_{brace} = stress in brace at a given point on hysteresis, ksi

$$\Delta_{frame} = \frac{L_{yield}\varepsilon_{brace}}{\cos\theta} \quad (5)$$

Where:

Δ_{frame} = frame horizontal displacement at a given brace strain, in

L_{yield} = length of brace yielding core, in

ε_{brace} = strain in brace at a given point on hysteresis, in/in

θ = angle between brace and beam

The resulting plot of brace force vs. horizontal beam displacement is shown in **Figure 46** and was used to prescribe the motion of the hydraulic actuators. The beam actuator was displaced horizontally by a small increment on the derived hysteresis then the brace actuator was adjusted to the corresponding force value from the derived hysteresis. This stair-stepped process was continued until the entire hysteresis loop had been traveled by the specimen as shown in **Figure 47**.

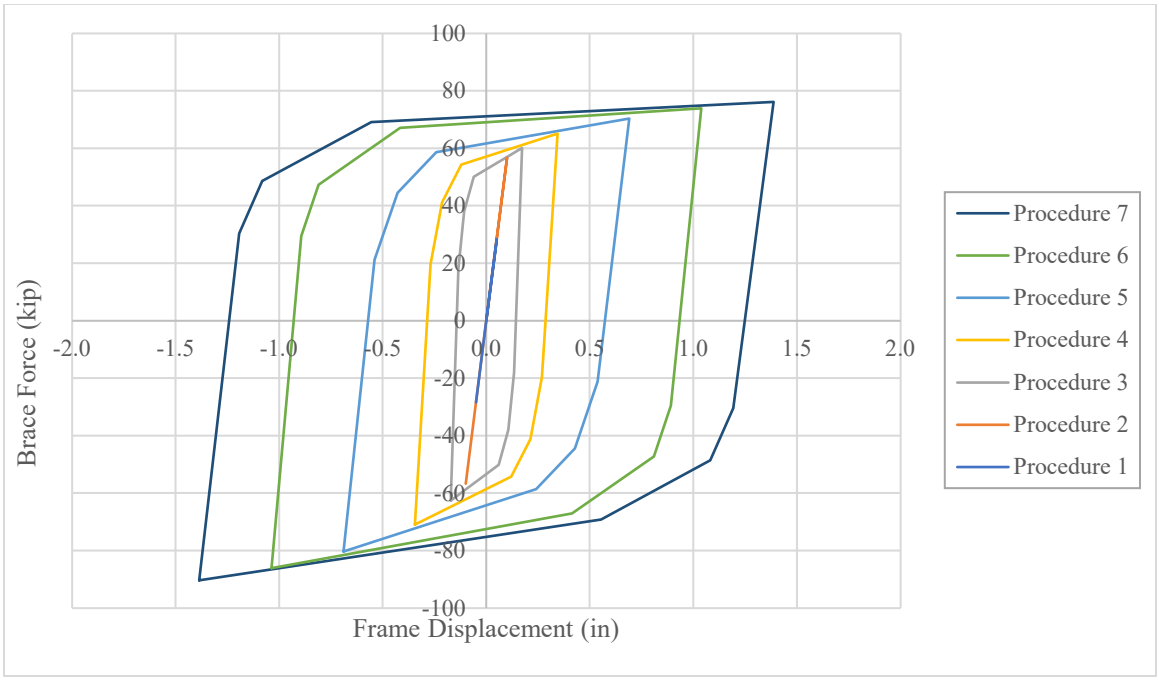

Figure 46: Hysteresis in terms of frame displacement and brace force

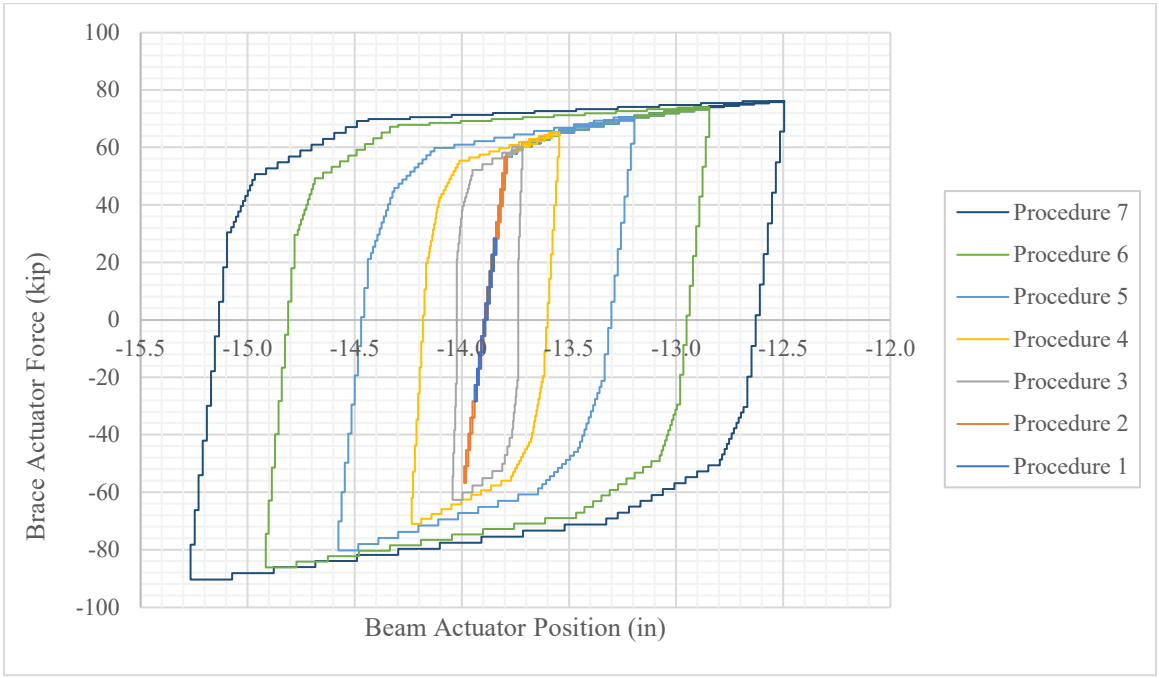

Figure 47: Prescribed hysteresis and its procedures

Because this process was time-consuming, the entire hysteresis was split into seven different procedures so that the test could be completed over multiple days. Each procedure corresponded to a level of brace strain in the previously described hysteresis and are designated by the colors of **Figure 47**. Because the test was completed over multiple days, each procedure was designed to return to the unloaded state after each cycle. Two cycles of each procedure were to be completed. The generalized test procedure with enumerated steps is shown below in **Figures 48** and **49**.

Test sequence for Procedures 1-2:

1. Load to the tension peak
2. Pause to check OOP instruments and take string potentiometer manual measurements
3. Unload to zero force and zero displacement
4. Pause to check OOP instruments and take string potentiometer manual measurements
5. Load to the compression peak
6. Pause to check OOP instruments and take string potentiometer manual measurements
7. Unload to zero force and zero displacement following the backbone of the hysteresis curve
8. Inspect specimen for cracking. If found color and mark ends of crack with cycle number
9. Repeat steps 1-8 for second cycle

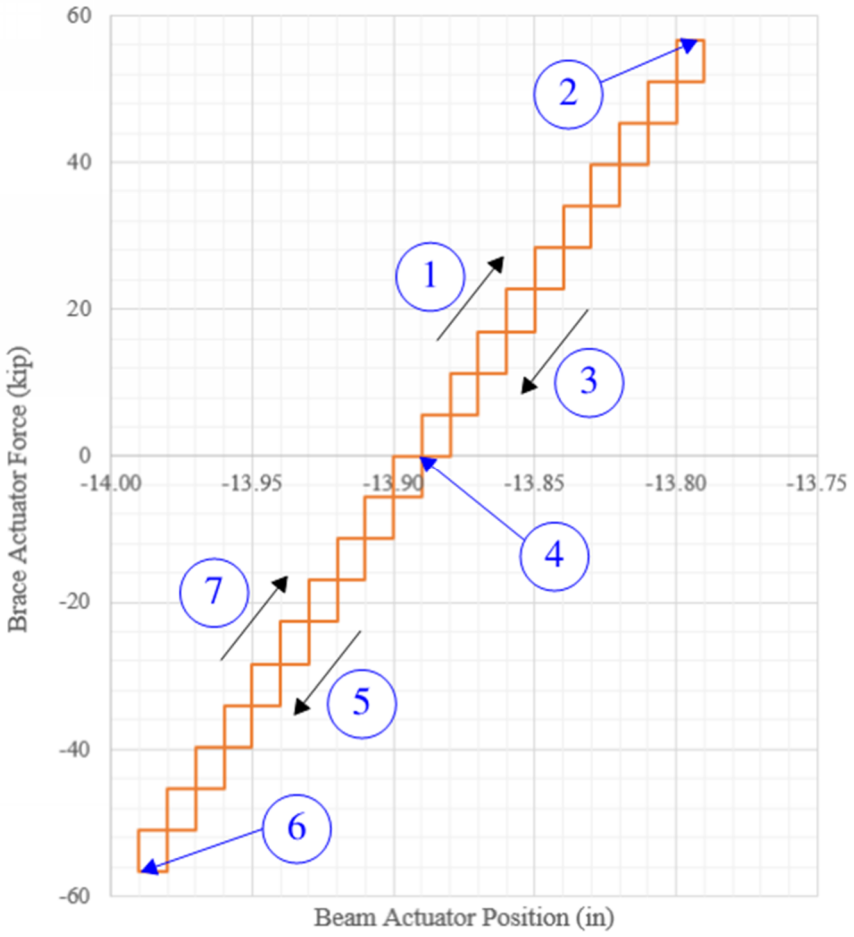

Figure 48: Test sequence for Procedures 1-2

Test sequence for Procedures 3-7:

1. Load to the tension peak following the backbone of the hysteresis curve
2. Pause to check OOP instruments and take string potentiometer manual measurements
3. Load to next change in slope of hysteresis curve
4. Pause to check OOP instruments and take string potentiometer manual measurements
5. Repeat steps 3-4 until tension peak is reached again following the hysteresis curve

6. Unload to zero force and zero displacement following the backbone of the hysteresis curve
7. Inspect specimen for cracking. If found color and mark ends of crack with cycle number
8. Repeat steps 1-7 for second cycle

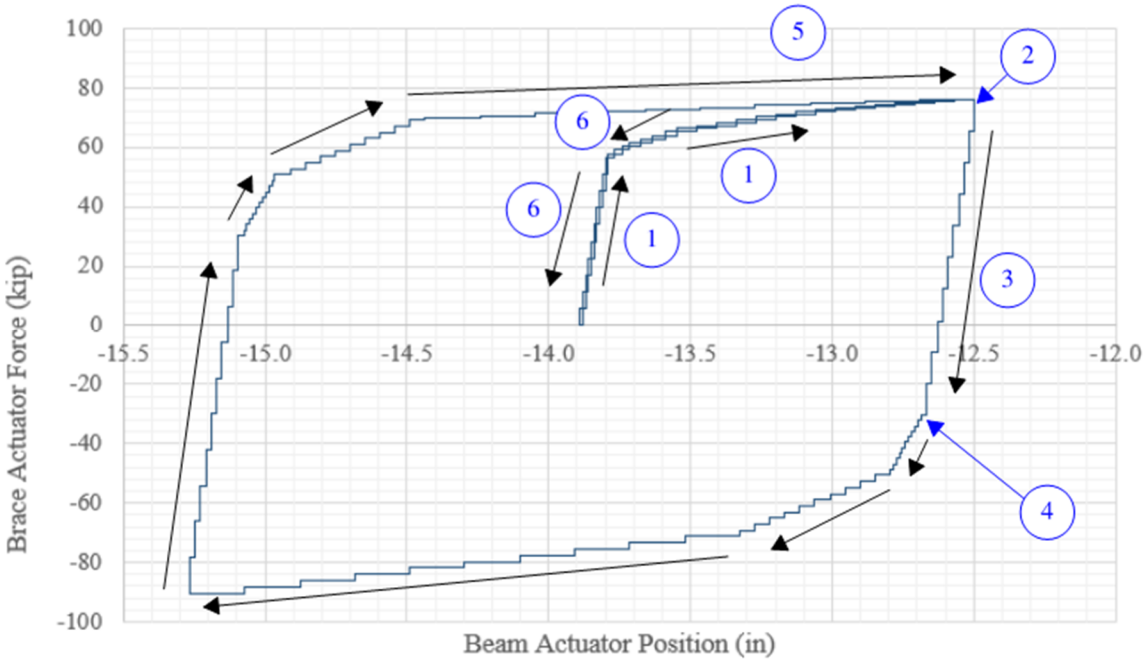

Figure 49: Test sequence for Procedures 3-7

CHAPTER FIVE

RESULTS AND DISCUSSION

Overview

Data sources monitored during this test included: beam and brace actuator position and force, out of plane motion, column base slip, column curvature, crack patterns, corbel reinforcing bar strains, and gusset plate strains.

The results show that the interface force distribution assumed by the UFM is not accurate for this specimen and the interface force distribution changed significantly with increased frame displacement. Much of the variation from the UFM can likely be attributed to frame action, which is the addition of shear and normal forces to the gusset interfaces from the opening and closing of the angle between the beam and column. Lin [11] showed that frame action forces from fixed frames should always be additive to the interface shear force and subtractive to the interface normal forces computed using the UFM. Although the test specimen had much more flexible connections than the fixed frames tested by Lin, the results of this study are shown to generally agree with his findings regarding interface forces.

It will also be shown that the pinned frame assumption is not accurate for this specimen. It is believed that the fixity of its base increases with increasing frame displacement. This change in apparent fixity is likely attributed to room for movement in the system from the oversized holes necessary for tolerancing. This is likely a cause for some of the deviation of member forces from the pinned distribution assumption and the attraction of more load to the column interface with increased frame displacement.

Further validation of this theory is demonstrated through the results of a simplistic finite element model correlated to the force-displacement behavior of the test specimen.

Prescribed Brace Force Hysteresis

Except for Procedure 7, both cycles of each procedure were executed and achieved behavior very close to the desired hysteresis. The distribution of force between the members did not follow the UFM distribution or the pinned assumption made in design, with the beam attracting much more force than expected. This deviation caused the beam actuator to hit the safety limit on its tension capacity, 98 kips, just shy of Procedure 7's peak in tension. **Figure 50** shows the experimental hysteresis for one cycle of each procedure, along with the point at which the actuator safety limit was hit; **Figure 51** compares the prescribed and experimental hysteresis for Procedure 6 and Procedure 7.

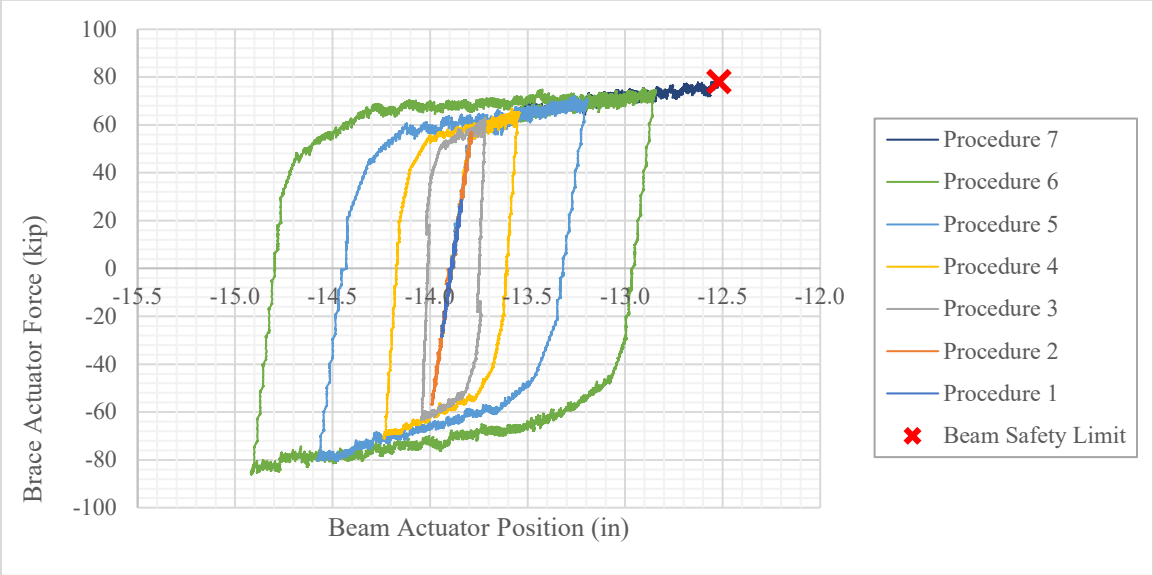

Figure 50: Experimental hysteresis, one cycle shown for each procedure

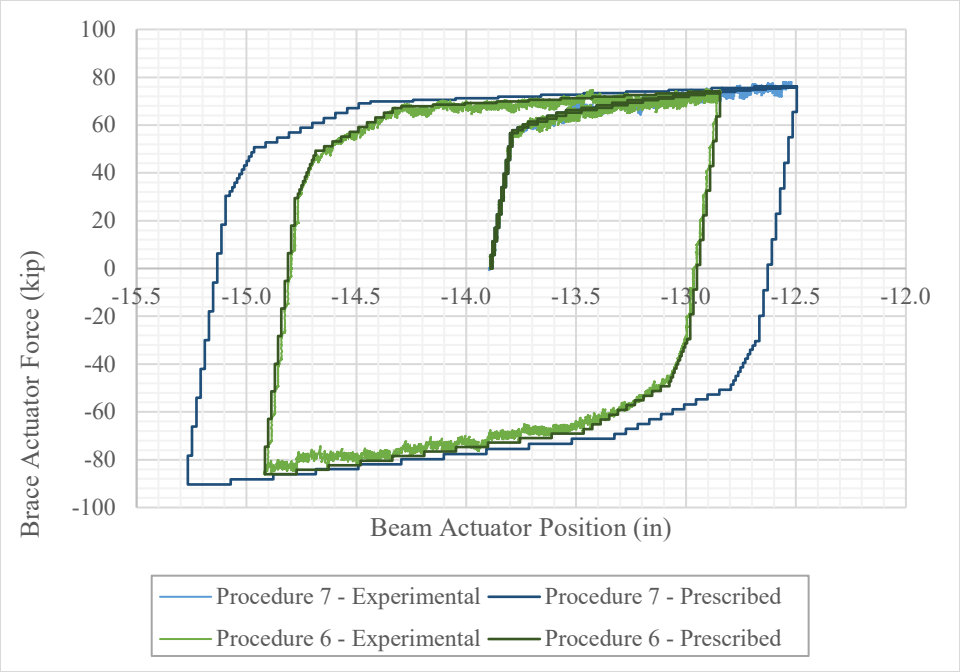

Figure 51: Comparison between prescribed and experimental hysteresis for Procedure 6

Concrete Member Forces

As discussed previously, the precast BRBF was assumed to be fully pinned. As the magnitude of prescribed brace force increased, the measured beam force generally started to deviate more from the theoretical (calculated from the fully pinned assumption), see **Table 3** and **Figure 52**. This deviation begins to be particularly significant in Procedure 5, with a frame displacement corresponding to $0.5\Delta h_{2\%}$.

Table 3: Percent error between experimental and theoretical (fully pinned) beam forces

Procedure	% Error, Brace in Tension	% Error, Brace in Compression
1	1.22%	3.79%
2	3.42%	3.70%
3	3.97%	3.78%
4	7.66%	6.15%
5	20.18%	10.24%
6	34.41%	15.83%
7	46.51%	-

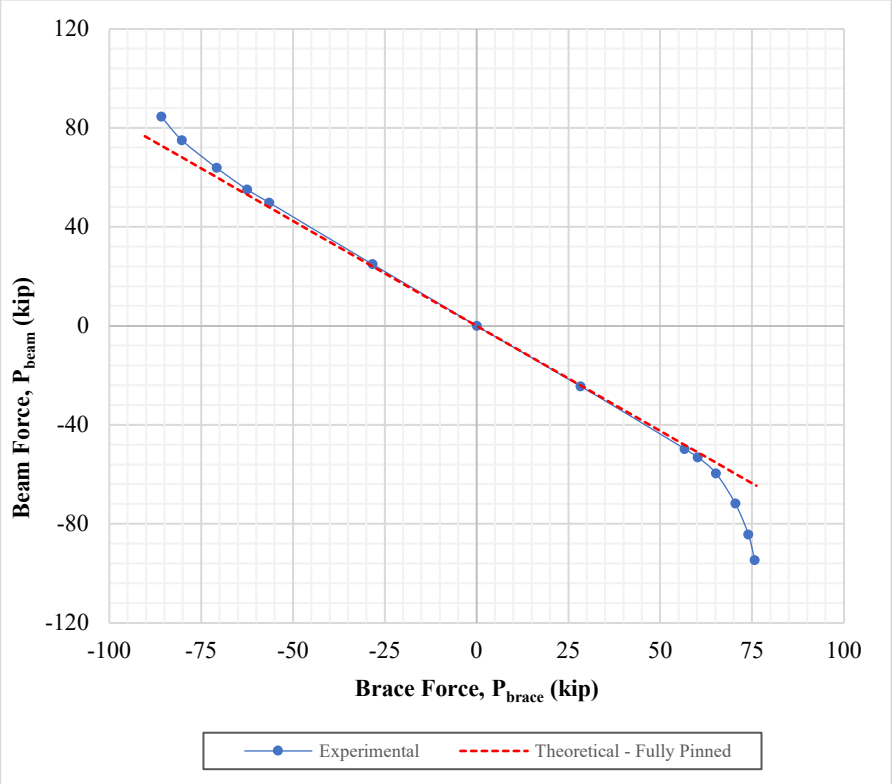

Figure 52: Beam internal force vs. brace internal force, theoretical (fully pinned) and experimental

Column internal forces were not measured directly. Under the fully pinned frame assumption the column force could be calculated using **Equation 4**.

$$P_{column} = P_{beam} \tan(\theta) \tag{4}$$

Where:

P_{column} = calculated internal axial force in column (kip)

P_{beam} = measured internal axial force in beam (kip)

θ = angle between beam and brace

Because the tested beam forces deviated significantly from the fully pinned frame assumption the original plan of estimating the column forces **Equation 4** was abandoned. Instead, a finite element model was created to simulate the frame behavior observed during testing. Through this model, more accurate estimates of column force were made. This model and its results are described in detail in the "Finite Element Frame Model" section at the end of the chapter.

Global Motion: Column Curvature, System Slip, and Out of Plane Motion

Four string potentiometers along the length of the column monitored its curvature perpendicular to its longitudinal axis. A dial gauge at the base of the column monitored the movement of the base perpendicular to its longitudinal axis. One string potentiometer along the column's longitudinal axis measured its axial deformation. **Figure 53** shows the deformed shape of the column as measured by string potentiometers at selected procedures while the brace was in tension. **Figure 54** shows beam actuator LVDT measurements overlaid with the deformed shape of the column. The tension cycles were

primarily used to answer questions regarding the force distribution because out of plane (OOP) motion of the gusset was minimized. Procedure 1 was excluded from **Figures 53** and **54** because one or more of the measured values was smaller than the string potentiometer accuracy (0.25% of potentiometer total stroke).

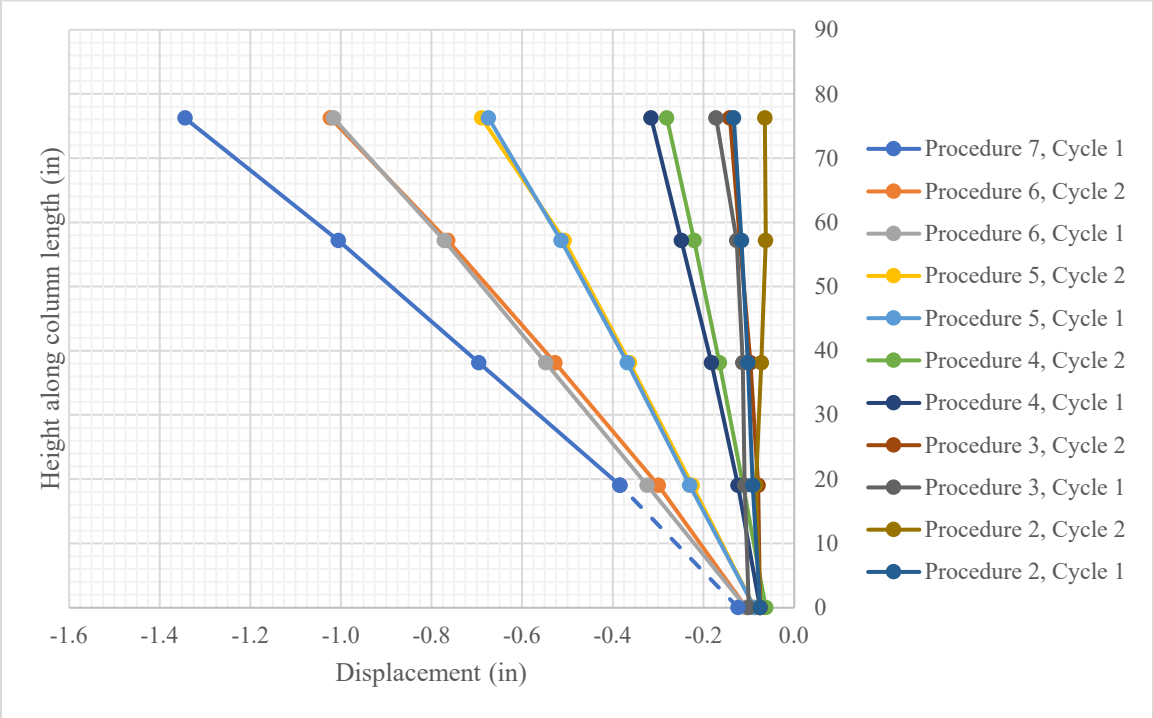

Figure 53: Column curvature while the brace was in tension

The value of displacement measured at the column base for Procedure 7, Cycle 1 was linearly interpolated from the displacements measured for Procedure 6 and Procedure 5 because a camera malfunctioned, therefore this value was not recorded. In general, slip was significant compared to overall system displacement for the first two procedures (1/2 of elastic brace force and elastic brace force) as shown in **Figure 53**.

The displacements at the column were consistent with the LVDT measurements from the beam actuator. If the curvature plots in **Figure 53** are extrapolated to the

displacement at the centerline of the beam the average error between the beam actuator LVDT displacement and extrapolated column string pot measurements is 17% for procedures 2 -7 and a maximum of 24% at Procedure 4.

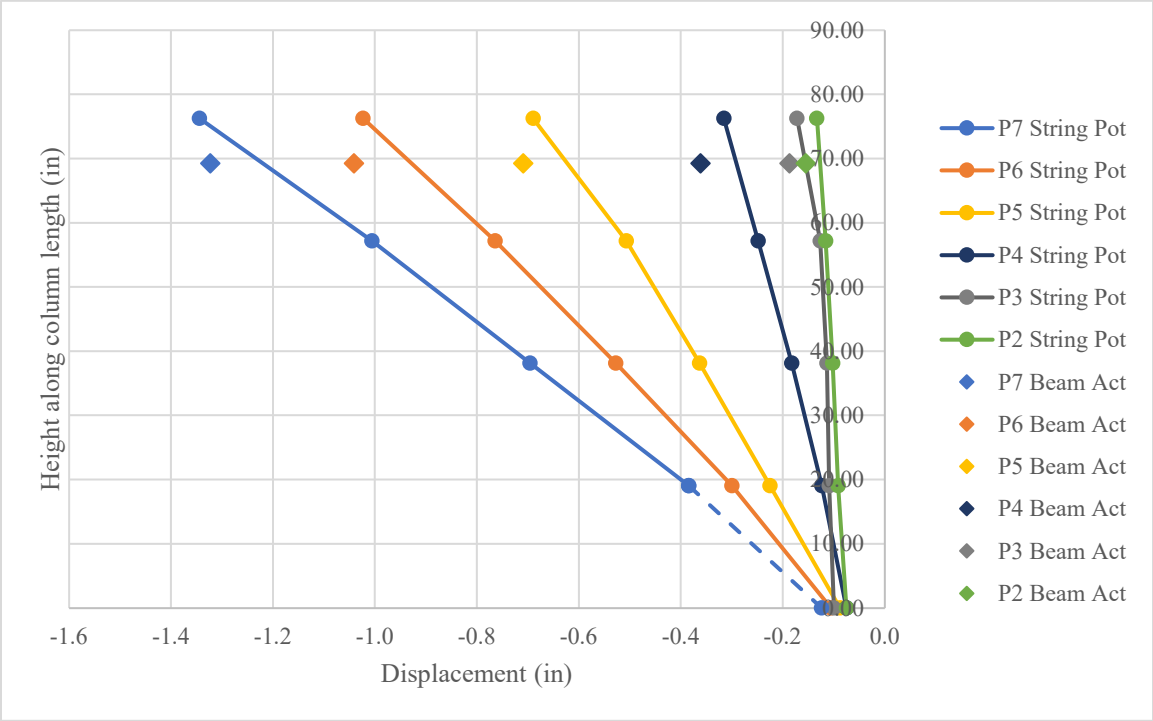

Figure 54: Column curvature while the brace was in tension compared to beam actuator LVDT measurements

System OOP motion was monitored by a dial gauge at the ⅝ point of the column measured from its base. The maximum OOP motion of the column measured by this dial gauge was 0.022". In addition, the OOP motion of the gusset plate was monitored by the digital image correlation (DIC) system, which measured a maximum gusset OOP motion of 0.031". **Table 4** summarizes the maximum OOP motion for each procedure. As mentioned previously, OOP motion of the gusset plate is generally less significant in the tension cycles, thus for the purposes of calculating interface forces from the strain gauges on gusset plate the tension cycles were considered the most accurate.

Table 4 Maximum OOP motion for procedures 1-7

	Max. Column OOP Movement (in)		Max. Average Gusset OOP Movement (in)	
	Tension	**Compression**	**Tension**	**Compression**
Procedure 1	0.003	-0.003	0.001	0.007
Procedure 2	0.004	-0.003	-	0.011
Procedure 3	0.005	-0.006	-	-
Procedure 4	0.016	-0.006	0.008	0.010
Procedure 5	0.019	-0.007	-	-
Procedure 6	0.022	-0.011	0.010	0.031
Procedure 7	0.010	-	0.022	-

Bar Strains and Crack Patterns

Corbel Reinforcing Bar Strains

Linear strain gauges were installed on reinforcing bars at the top and the bottom of the corbel. Four strain gauges were responsive, gauges 3, 4, 7, and 8. Gauges 3 and 4 were in the top layer of reinforcing and 7 and 8 were in the bottom layer of reinforcing, as shown in **Figure 40.** The maximum bar strain at each location for each procedure is provided in **Table 5** and **Figure 55**. All corbel reinforcement remained in the elastic range with the largest recorded strain being 6% of yield strain.

Table 5: Maximum absolute value of strain observed in corbel reinforcing bars

Max. Absolute Value of Longitudinal Strain (in/in)								
Procedure	**Gauge 3**	**% of Yield**	**Gauge 4**	**% of Yield**	**Gauge 7**	**% of Yield**	**Gauge 8**	**% of Yield**
1	3.76E-05	1.8%	8.00E-06	0.4%	8.75E-06	0.4%	6.14E-06	0.3%
2	7.04E-05	3.4%	1.20E-05	0.6%	1.87E-05	0.9%	5.72E-06	0.3%
3	7.20E-05	3.5%	1.45E-05	0.7%	2.91E-05	1.4%	9.57E-06	0.5%
4	8.23E-05	4.0%	1.25E-05	0.6%	4.08E-05	2.0%	9.38E-06	0.5%
5	8.98E-05	4.3%	1.70E-05	0.8%	6.26E-05	3.0%	1.68E-05	0.8%
6	1.24E-04	6.0%	2.85E-05	1.4%	8.95E-05	4.3%	2.51E-05	1.2%
7	7.66E-05	3.7%	2.00E-05	1.0%	8.31E-05	4.0%	1.27E-05	0.6%

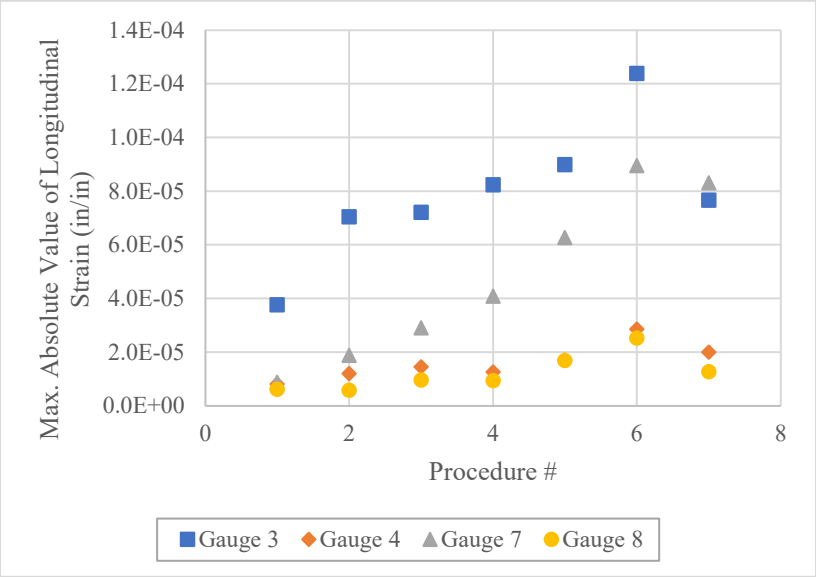

Figure 55: Maximum absolute value of strain observed in corbel reinforcing bar

Strains in the corbel reinforcing bars gauged were significantly lower than what was expected. There are several likely causes for these very low strain gauge readings. First, though only the (8) #6 corbel primary tension reinforcing bars were assumed to carry interface force in design, it is likely that the supplemental (6) #5 bars provided to prevent undesirable embedded plate bending also carried some of the interface forces. See **Figure 56** for location of the supplemental #5 bars. Second, the strain gauges were adhered along the longitudinal axis of the bars, and therefore would have only effectively measured tension or compression in this direction. Shear interface force would have been carried primarily by dowel action, which would have been difficult to observe using the strain gauges as oriented in this test. The observed interface normal force was much lower than the UFM prediction and the observed interface shear force was much higher

than the UFM prediction, see “Gusset Plate Interface Forces” section following. This much higher shear would not have been easily observed with the strain gauges applied.

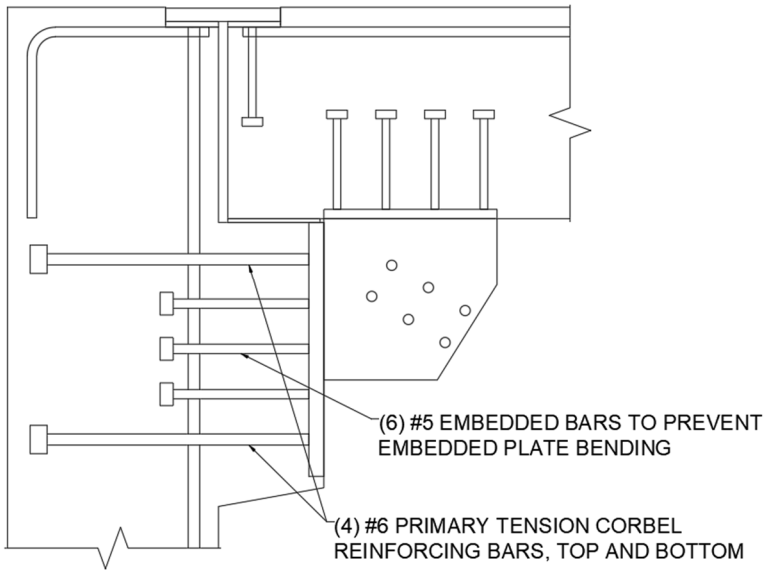

Figure 56: Reinforcing bars resisting column interface forces

Beam and Column Longitudinal Bar Estimated Strains

Due to limitations of how many instruments could be input to the data acquisition system, strains in the beam and column longitudinal reinforcing were not monitored by strain gauges. Instead, cracks were tracked and marked each cycle and an estimate of longitudinal bar strains was calculated from crack data. After all procedures and cycles were completed, all crack locations and widths were measured. These measurements were taken while the specimen was unloaded for safety reasons.

Most of the cracks observed ran perpendicular to the longitudinal axis of the beam and column. The width and spacing between these perpendicular cracks were used to approximate strain in the longitudinal bars for each procedure using **Equations 5** and **6**. There are several sources of error that make calculations using these equations only

estimates of the bar strains. First, the crack widths in the loaded condition, more representative of the state of stress at that time, would in theory be larger than those measured in the unloaded state. This causes the calculated strains at the crack location to be unconservative.

Second, this method of estimation assumes a constant strain, and therefore stress, in the bars over the spacing between the cracks, L_{gage}. This is not truly the stress state in the bars when the concrete is cracked. The tensile force in the bar is higher at the cracked section than in the uncracked section. A representation of this is shown in **Figure 57** below [30]. This also causes the calculated strains at the crack location to be lower than the true bar strains.

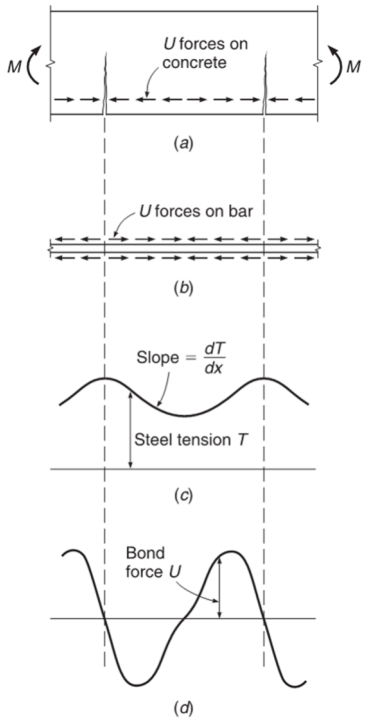

Figure 57: "Variation of steel and bond forces in a reinforced concrete member subject to pure bending: (a) cracked concrete segment; (b) bond forces acting on reinforcing bar; (c) variation of tensile force in steel; and (d) variation of bond force along steel" [30]

Although the estimates for strain are likely lower than true strain values, the yield stress of the bars is likely higher than the minimum of 60 ksi specified in the corresponding ASTM standard and therefore the bars have additional strain capacity beyond 0.00207. Though only estimates, these values are still informative for understanding system behavior and relative deformations between the beam and column.

$$L_{gage} = \frac{d_{next} - d_{last}}{2} \tag{5}$$

Where:

L_{gage} = "undeformed" length of beam or column considered

d_{next} = distance from crack of interest to the next nearest crack

d_{last} = distance from crack of interest to previous nearest crack

$$\varepsilon_{bar} = \frac{w_{crack}}{L_{gage}} \tag{6}$$

Where:

ε_{bar} = strain in longitudinal bars

w_{crack} = crack width perpendicular to beam or column longitudinal axis

L_{gage} = "undeformed" length of beam or column considered

The maximum estimated strains calculated for the beam and the column for all cycles indicate that the longitudinal bars likely remained elastic for the duration of testing. The maximum estimated strain, its location, and crack number for each procedure can be found in **Table 6** for the beam and **Table 7** for the column.

The maximum estimated strain observed between the beam and column calculated from the cracks in their unloaded state was 77% of the lower bound yield strain of the Grade 60 reinforcing bars used (0.00207). From this data we cannot definitively claim the beam longitudinal reinforcement did not yield in Procedures 6 and 7. However, the observed crack widths would need to be 25% wider (0.004 in width to 0.005 in width) in their loaded state to indicate bar yielding for rebar of minimum allowable strength.

Table 6: Maximum beam bar longitudinal strain calculated from cracking

Procedure	Max. Beam Bar Longitudinal Strain (in/in)	Estimated Percent of Yield Strain	Crack Number	Location Measured from Beam Right End (in)
4	0.000552	27%	9	35
5	0.001333	64%	8	32
6	0.001600	77%	10	37.5
7	0.001600	77%	10	37.5

Table 7: Maximum column bar longitudinal strain calculated from cracking

Procedure	Max. Column Bar Longitudinal Strain (in/in)	Estimated Percent of Yield Strain	Crack Number	Location Measured from Column Base (in)
4	0.000640	31%	26	20
5	0.000640	31%	24	14
6	0.001333	64%	25	17
7	0.001333	64%	24	14

Figures 58 and **59** show the crack progression for the beam and column. No cracks were noted in the beam or column until Procedure 4. The beam and column had similar crack spacings by the end of all procedures, an average of 3.93” and 4.38”, respectively. The first beam cracks were noted near its midspan; cracks in subsequent cycles generally progressed toward its ends. The first column cracks were noted near its base; cracks in subsequent cycles generally progressed toward the corbel.

Figure 58: Beam crack progression, (a) Procedure 4 - Cycle 1, (b) Procedure 4 – Cycle 2, (c) Procedure 5 – Cycle 1, (d) Procedure 5 – Cycle 2, (e) Procedure 6 – Cycle 1, (f) Procedure 6 – Cycle 2, (g) Procedure 7 – Cycle 1

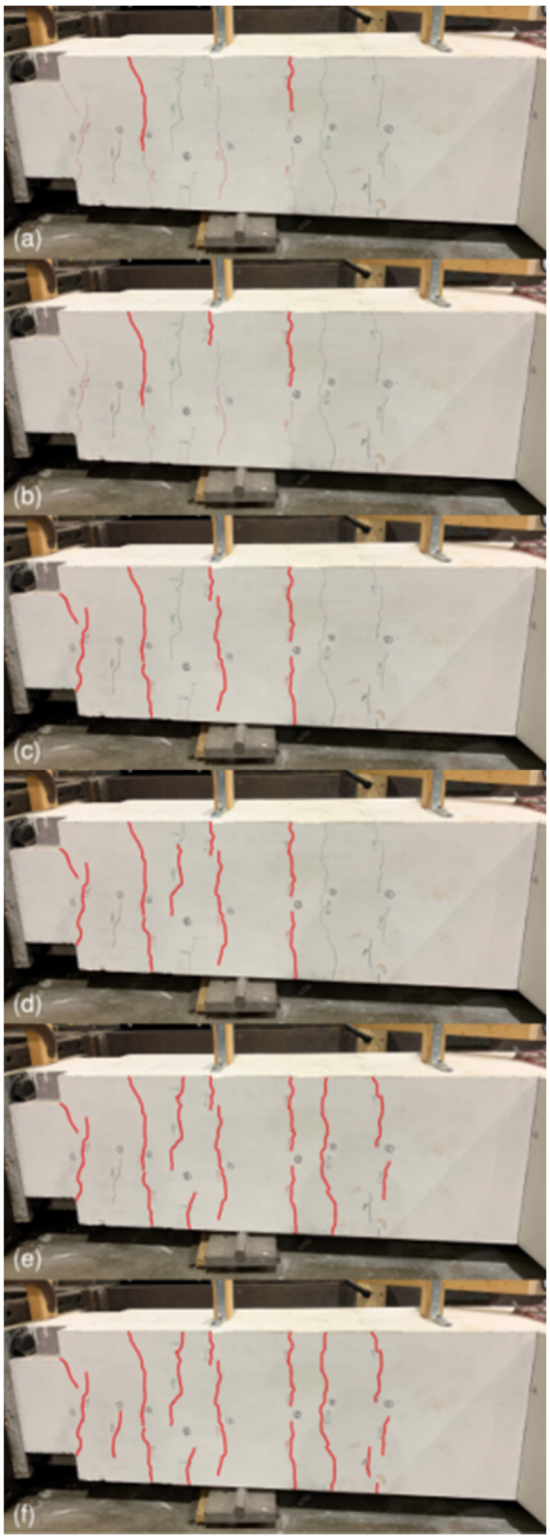

Figure 59: Column crack progression, (a) Procedure 4 - Cycle 1, (b) Procedure 4 – Cycle 2, (c) Procedure 5 – Cycle 1, (d) Procedure 6 – Cycle 1, (e) Procedure 6 – Cycle 2, (f) Procedure 7 – Cycle 1

Gusset Plate Interface Forces

Determination of Experimental Interface Forces

Experimental interface forces were determined using data from the rectangular strain rosettes that were placed along the gusset plate's connected edges. Because the strains measured on the gusset plate remained elastic throughout the duration of the test, the stresses at each gauge location could be determined using the elastic and shear moduli of the plate through **Equations 7** and **8**.

$$\sigma_{exp} = \varepsilon_{exp} * E \tag{7}$$

Where:

σ_{exp} = experimental normal stress (ksi)

ε_{exp} = normal strain at beam or column connected interface from strain gauge (in/in)

E = plate elastic modulus (ksi)

$$\tau_{exp} = \gamma_{exp} * G \tag{8}$$

Where:

τ_{exp} = experimental shear stress (ksi)

γ_{exp} = shear strain at beam or column connected interface from strain gauge (in/in)

G = plate shear modulus (ksi)

Sign convention and anticipated signs of interface forces and stresses for the states where the brace is in tension and compression are described in **Figures 60** and **61**.

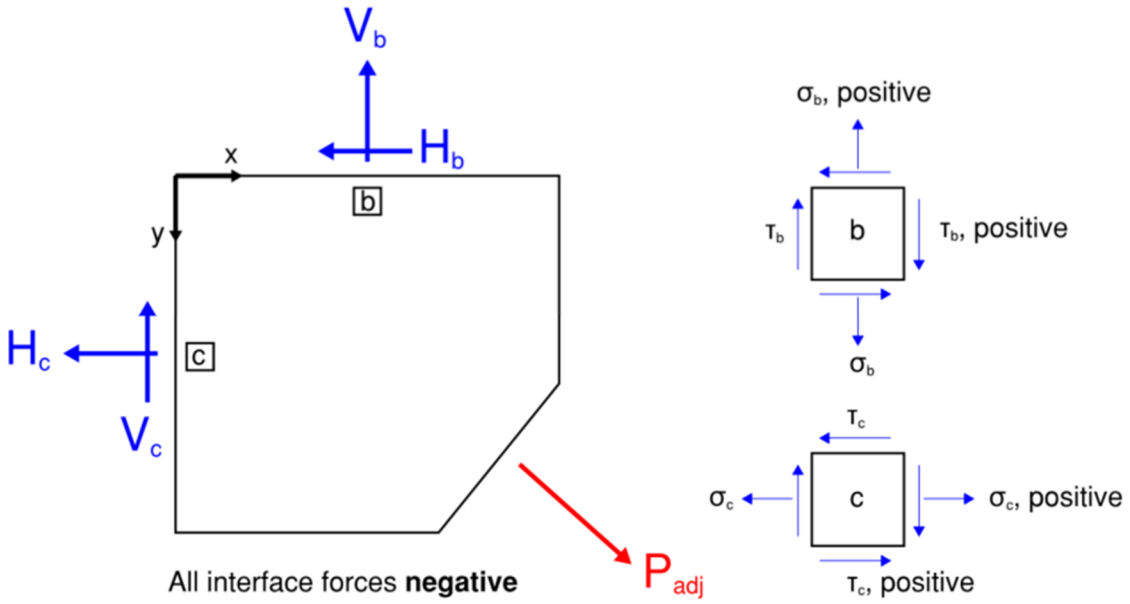

Figure 60: Expected force and stress signs when brace is in tension

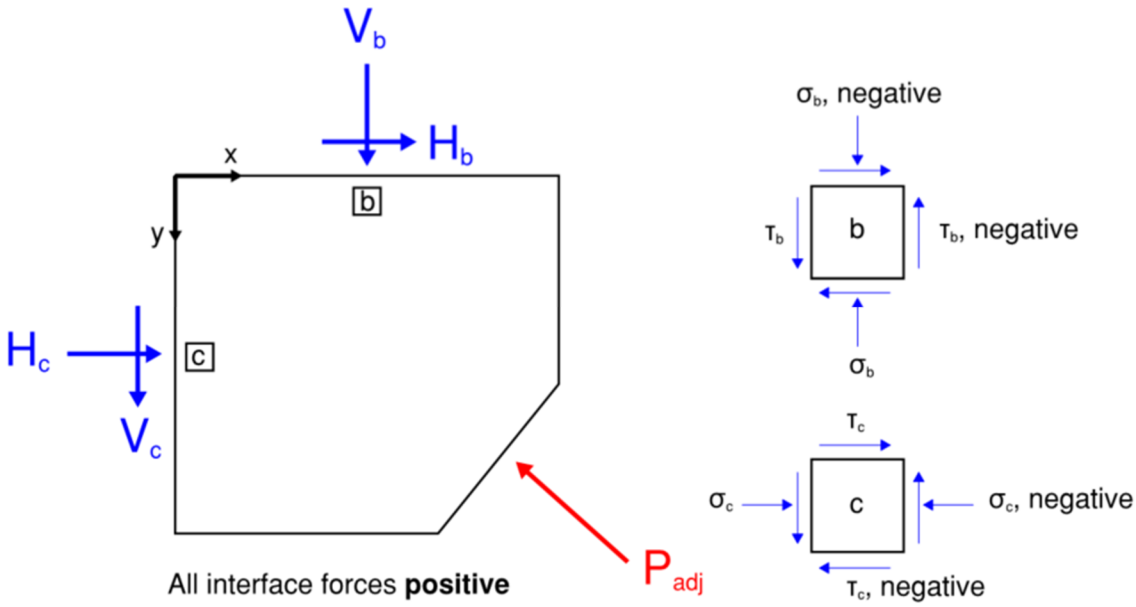

Figure 61: Expected force and stress signs when brace is in compression

Experimental normal stress distributions along the beam and column connected edges are shown in **Figures 62** and **63** and experimental shear stress distributions are shown in **Figures 64** and **65**. The variation of normal stress along the beam and column connected edges suggests some moment has developed at both interfaces. The assumption that only the column connected interface would see moment because of the gap at the beam-corbel bearing is likely incorrect. The gap at the beam-corbel bearing also cannot be isolated as the only source of interface moments.

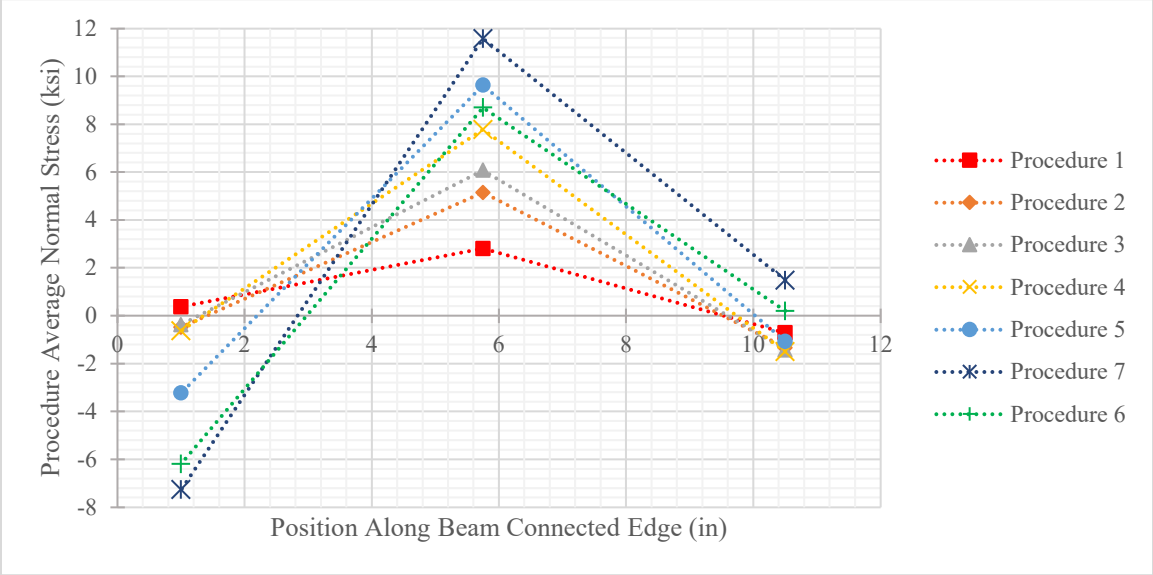

Figure 62: Beam edge experimental normal stress distribution

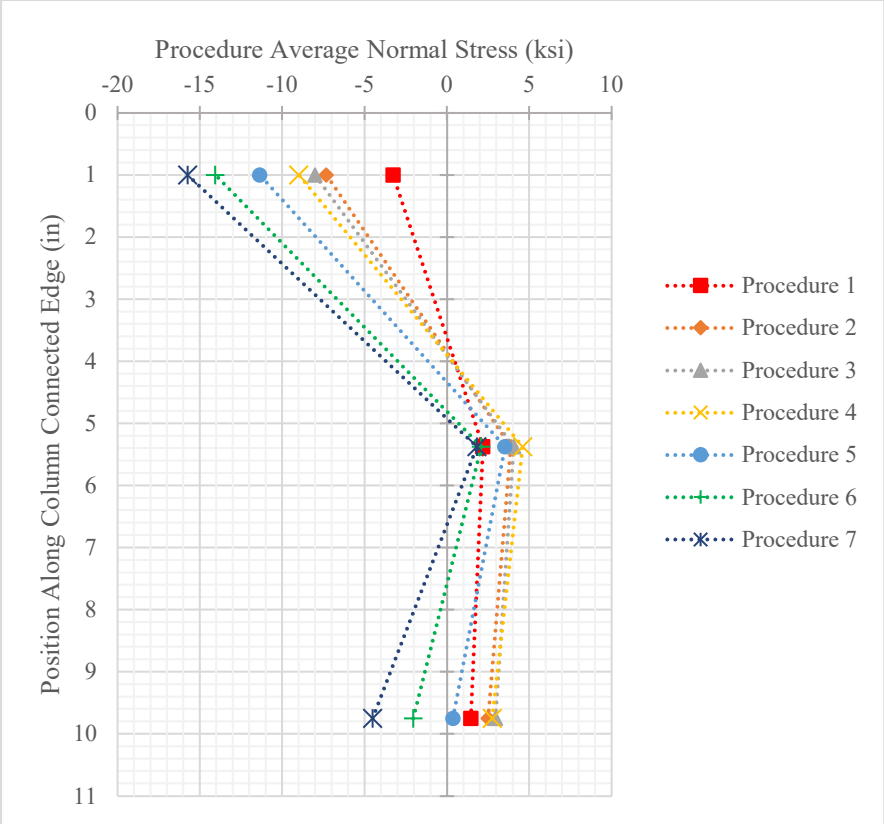

Figure 63: Column edge experimental normal stress distribution

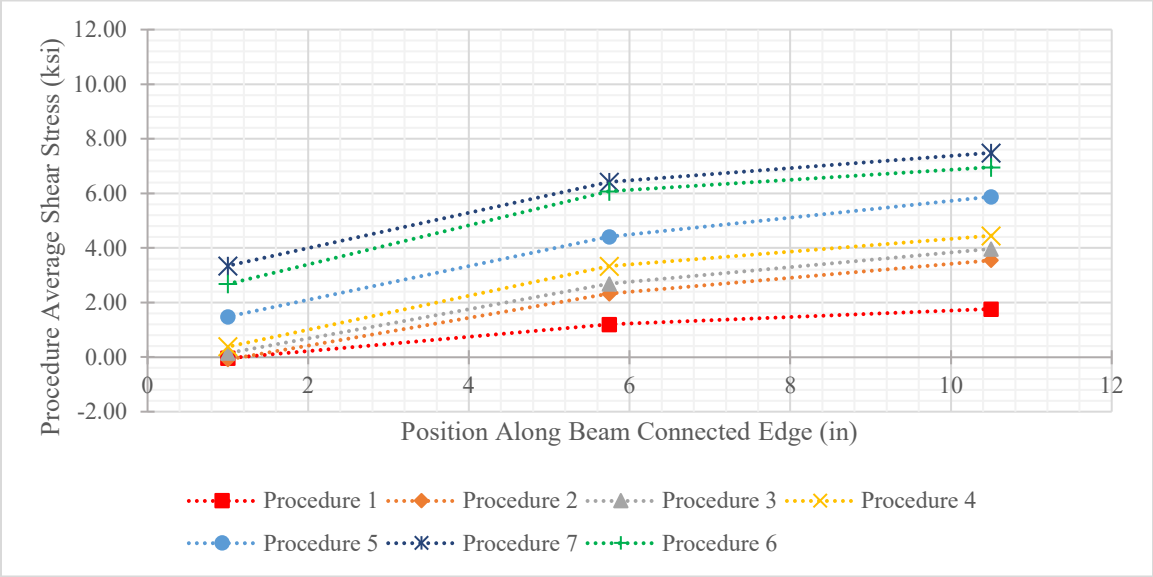

Figure 64: Beam edge experimental shear stress distribution

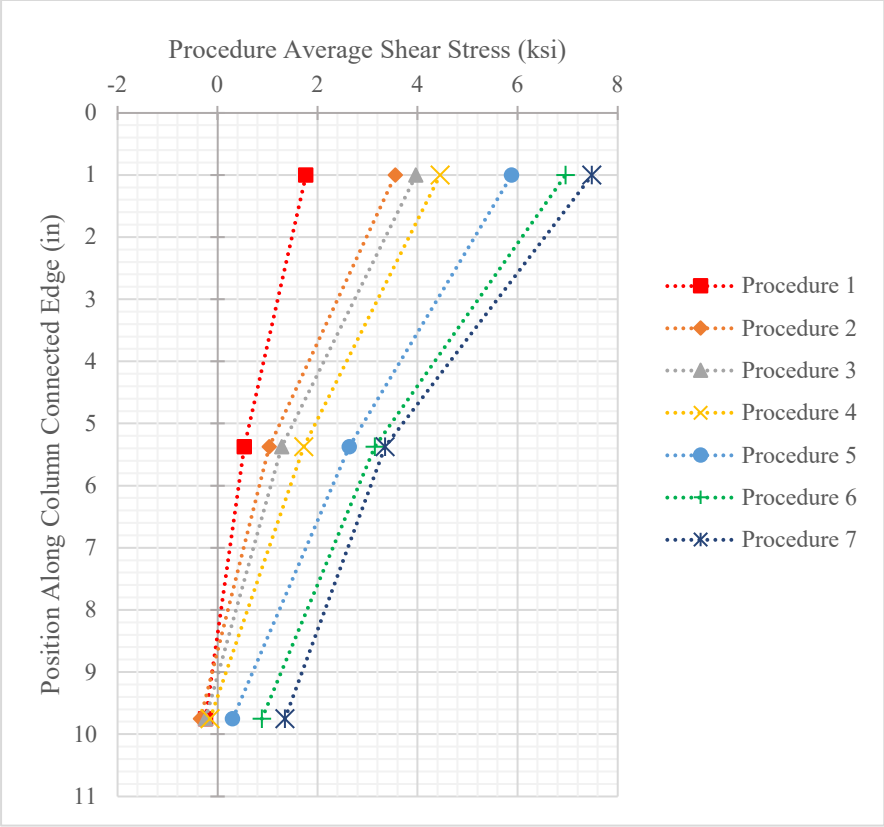

Figure 65: Column edge experimental shear stress distribution

The beam and column interfaces each had three gauges in contact with them; gauges 1-3 at the column and gauges 3-5 at the beam. To determine interface forces, an average was taken of normal and shear stress from the readings of all three gauges.

These stresses were then used to calculate the interface forces using **Equations 9-12**.

$$V_b = \sigma_{b,exp} * t_g * l_b \tag{9}$$

$$H_b = \tau_{b,exp} * t_g * l_b \tag{10}$$

$$V_c = \tau_{c,exp} * t_g * (l_c - l_g) \tag{11}$$

$$H_c = \sigma_{c,exp} * t_g * (l_c - l_g) \tag{12}$$

Where t_g, l_b, l_c, and l_g are defined in **Figure 66**.

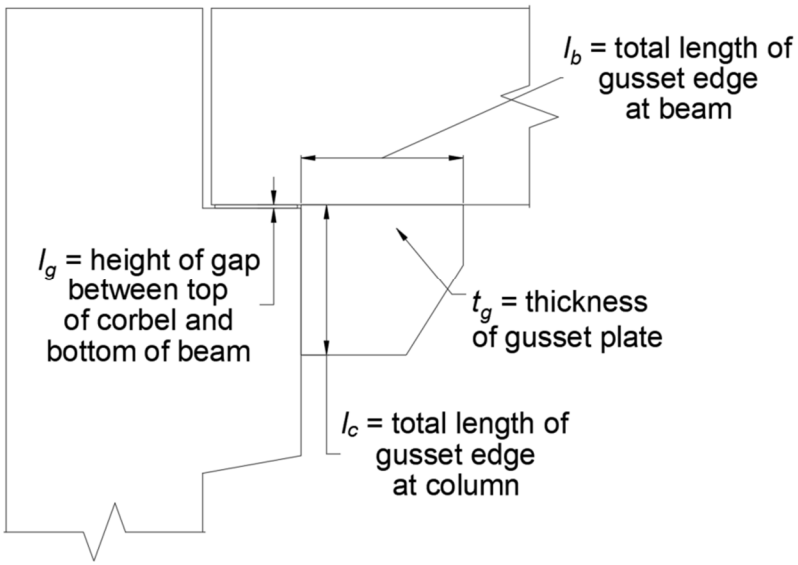

Figure 66: Variable definitions for determination of experimental interface forces

Comparison of Experimental and UFM Theoretical Interface Forces

A summary of interface forces derived from experimental strain gauge data and their theoretical companions derived from the UFM is provided in **Table 8**. There is

some error inherent to between the values even in the earliest procedures. This error occurs even in cycles where the brace is in tension, during which plate is least likely to experience OOP bending that would affect gauge readings. Generally, the average percent error increases as procedure number increases. Through all cycles the beam has higher forces along its longitudinal axis (shear) than the column (H_b vs V_c). However, the beam initially has more normal interface force than the column, but by the latter cycles the column has more normal loads than the beam (V_b vs H_c).

Table 8: Interface forces derived from experimental strain gauge data, brace in tension: red indicates negative percent error and blue indicates positive percent error.

	Procedure 1, Cycle 1			Procedure 1, Cycle 2			Procedure 2, Cycle 1		
	Th.	**Exp.**	**% Error**	**Th.**	**Exp.**	**% Error**	**Th.**	**Exp.**	**% Error**
V_b (kip)	-8.49	-4.86	**-42.8%**	-8.51	-4.69	**-44.9%**	-17.00	-8.74	**-48.6%**
H_b (kip)	-6.97	-11.23	**61.1%**	-6.99	-11.38	**62.8%**	-13.97	-23.43	**67.7%**
V_c (kip)	-6.52	-6.95	**6.5%**	-6.53	-6.82	**4.4%**	-13.06	-15.70	**20.2%**
H_c (kip)	-16.98	-0.66	**-96.1%**	-17.01	-0.54	**-96.8%**	-34.01	0.88	**-102.6%**
	Procedure 2, Cycle 2			**Procedure 3, Cycle 1**			**Procedure 3, Cycle 2**		
V_b (kip)	-17.00	-4.12	**-75.8%**	-18.08	-4.88	**-73.0%**	-18.09	-11.64	**-35.7%**
H_b (kip)	-13.96	-21.33	**52.8%**	-14.85	-25.76	**73.5%**	-14.86	-26.71	**79.7%**
V_c (kip)	-13.05	-12.64	**-3.1%**	-13.88	-15.66	**12.8%**	-13.89	-17.79	**28.1%**
H_c (kip)	-34.00	2.29	**-106.7%**	-36.15	4.47	**-112.4%**	-36.17	-1.16	**-96.8%**
	Procedure 4, Cycle 1			**Procedure 4, Cycle 2**			**Procedure 5, Cycle 1**		
V_b (kip)	-19.55	-11.87	**-39.3%**	-19.55	-9.98	**-49.0%**	-21.14	-11.51	**-45.6%**
H_b (kip)	-16.06	-31.19	**94.2%**	-16.06	-31.84	**98.2%**	-17.37	-45.43	**161.6%**
V_c (kip)	-15.01	-20.27	**35.0%**	-15.01	-19.93	**32.7%**	-16.24	-29.68	**82.8%**
H_c (kip)	-39.10	1.06	**-102.7%**	-39.10	4.40	**-111.2%**	-42.29	11.88	**-128.1%**
	Procedure 5, Cycle 2			**Procedure 6, Cycle 1**			**Procedure 6, Cycle 2**		
V_b (kip)	-21.17	-9.07	**-57.1%**	-22.21	-9.31	**-58.1%**	-22.21	-1.18	**-94.7%**
H_b (kip)	-17.39	-45.31	**160.6%**	-18.24	-57.77	**216.7%**	-18.25	-63.42	**247.6%**
V_c (kip)	-16.25	-29.07	**78.9%**	-17.05	-38.78	**127.4%**	-17.06	-34.52	**102.3%**
H_c (kip)	-42.34	13.01	**-130.7%**	-44.42	23.76	**-153.5%**	-44.43	22.96	**-151.7%**
	Procedure 7, Cycle 1								
V_b (kip)	-22.74	-11.17	**-50.9%**						
H_b (kip)	-18.68	-66.50	**256.1%**						
V_c (kip)	-17.46	-40.62	**132.7%**						
H_c (kip)	-45.47	30.71	**-167.5%**						

Frame action has been noted to have a significant impact on the magnitude of force that is observed at the gusset interfaces of steel and cast-in-place reinforced concrete fixed frames by Lin et al. [11], Tsai et al. [12], and Cui et al. [13]. Lin also noted that shear forces due to frame action should be additive to the shear components of brace load at an interface and normal forces due to frame action should be subtractive to the shear components of brace load at an interface. This phenomenon is observed in the experimental results of this test. Generally, H_b and V_c (the shear interface force components) have a positive percent error when compared to theoretical and V_b and H_c (the normal interface force components) have a negative percent error when compared to theoretical. This suggests that like these fixed frame tests from existing literature, the gusset in this test also sees significant impact from frame action of this "pinned" frame.

Distribution of Load Between Beam and Column

The vertical and horizontal force distributions to the beam and column are expressed as ratios and plotted for each procedure in **Figures 67-70**.

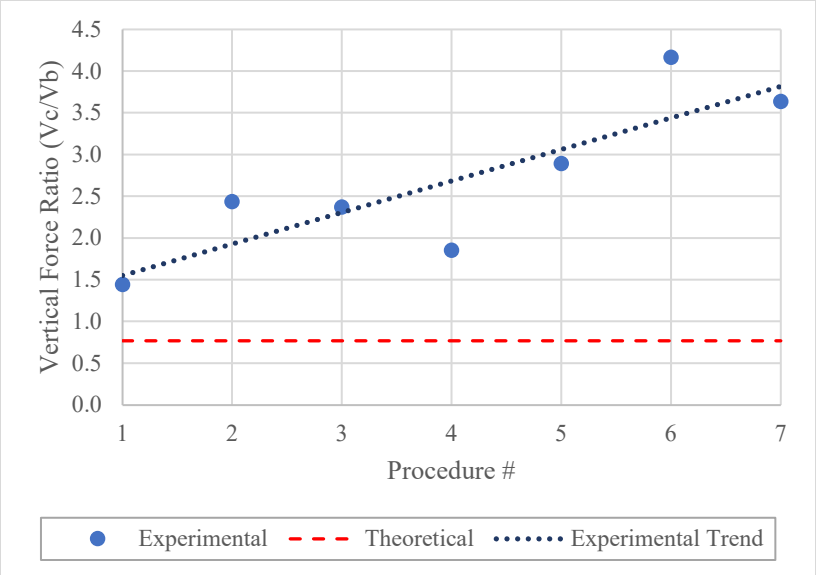

Figure 67: Distribution of vertical force between beam and column while brace is in tension

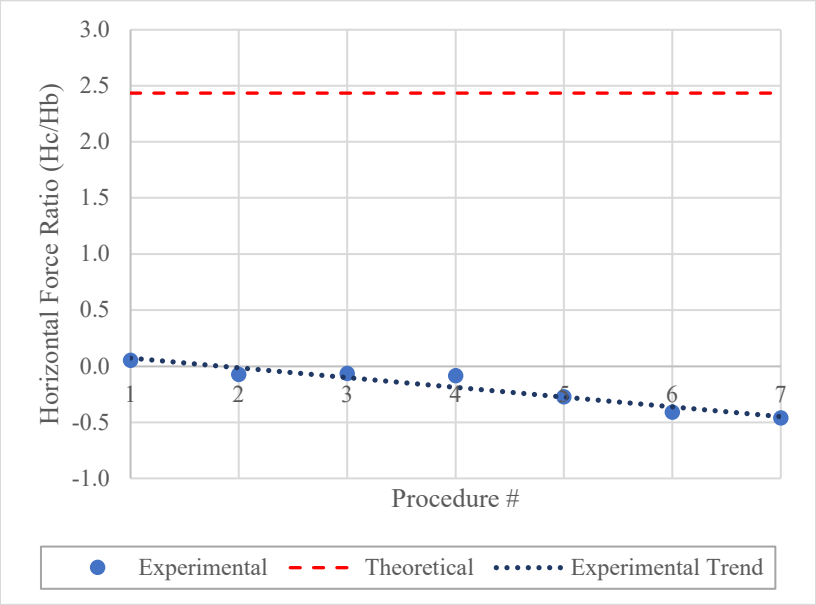

Figure 68: Distribution of horizontal force between beam and column while brace is in tension

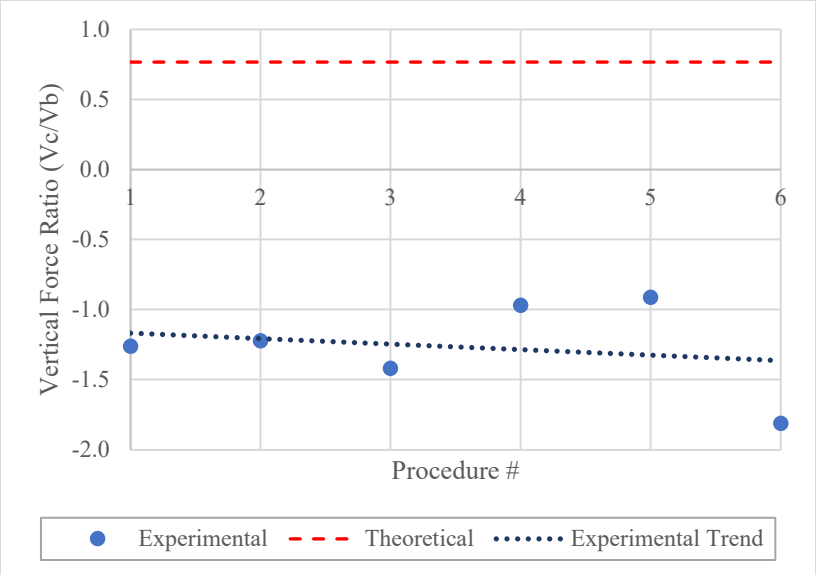

Figure 69: Distribution of vertical force between beam and column while brace is in compression

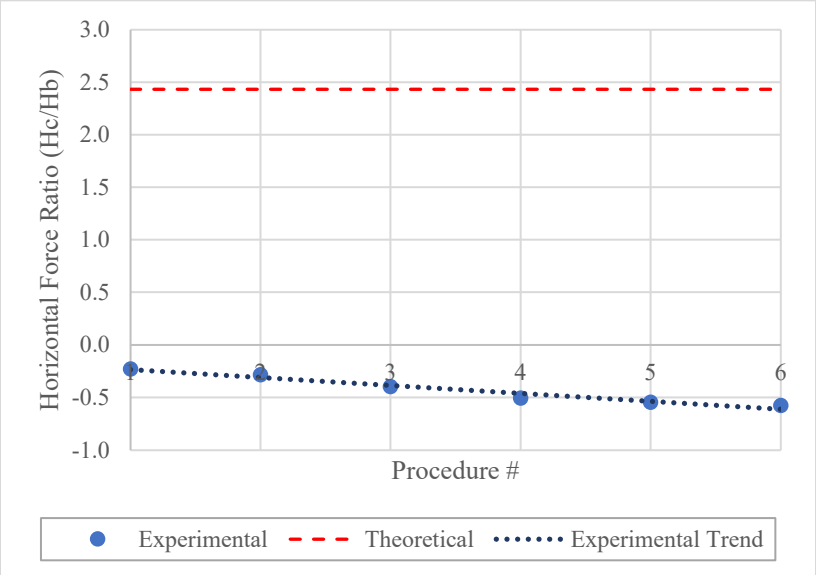

Figure 70: Distribution of horizontal force between beam and column while brace is in compression

Generally, the magnitude of the ratios of V_c/V_b and H_c/H_b increase with increasing brace load and frame displacement; implying that the column is attracting more load in higher procedures. In addition, compared to the UFM the beam is carrying a significantly higher ratio of the horizontal loads from even the onset of testing. Conversely, the beam carries slightly lower proportion of vertical force than predicted by UFM at the onset of testing.

Finite Element Frame Model

An increase in column base fixity with increasing brace load and frame displacement magnitude could be an explanation for the increase in percent error between the theoretical and experimental beam force and the increase in magnitude of V_c/V_b and H_c/H_b ratios. A change in column fixity is reasonable given the column connection was not an idealized true pin, but reflective of typical "pinned" precast connections and tolerancing permitted some initial movement at the connection. Another possibility is the frame has a partial fixity, but the interface force distribution changes with change in relative cracking between the beam and column. However, the relative amount of cracking observed in the beam compared to the column does not follow a consistent trend through the procedures, with the damage initially being more similar, then occurring more on the beam, and finally approaching more similar damage. Both column base partial fixity and differential stiffness between the beam and the column due to cracking could be causes for these discrepancies.

As a preliminary investigation to determine if changing column fixity would explain the difference in beam forces from the theoretical forced based on a pinned

frame, a simplistic finite element model was created using Hyperworks and ABAQUS initially neglecting the effects of the hairline cracking observed in the frame during testing. Future modeling efforts will include the examination of the influence of member cracking with higher fidelity models.

Model Description

A simplified frame model was constructed in ABAQUS. The frame members were modeled using 2-node linear B21 beam elements that neglect shear deformation. This approximation has some inherent error as the test data indicated that hairline cracking occurred in both the beam and column, but not likely enough to indicate bar yielding. Additionally, the strains in the corbel reinforcement did not indicate yielding. Fixity at the column base was modeled using a 1-node SPRING1 element. The restraints and releases of the frame are shown in **Figure 71**.

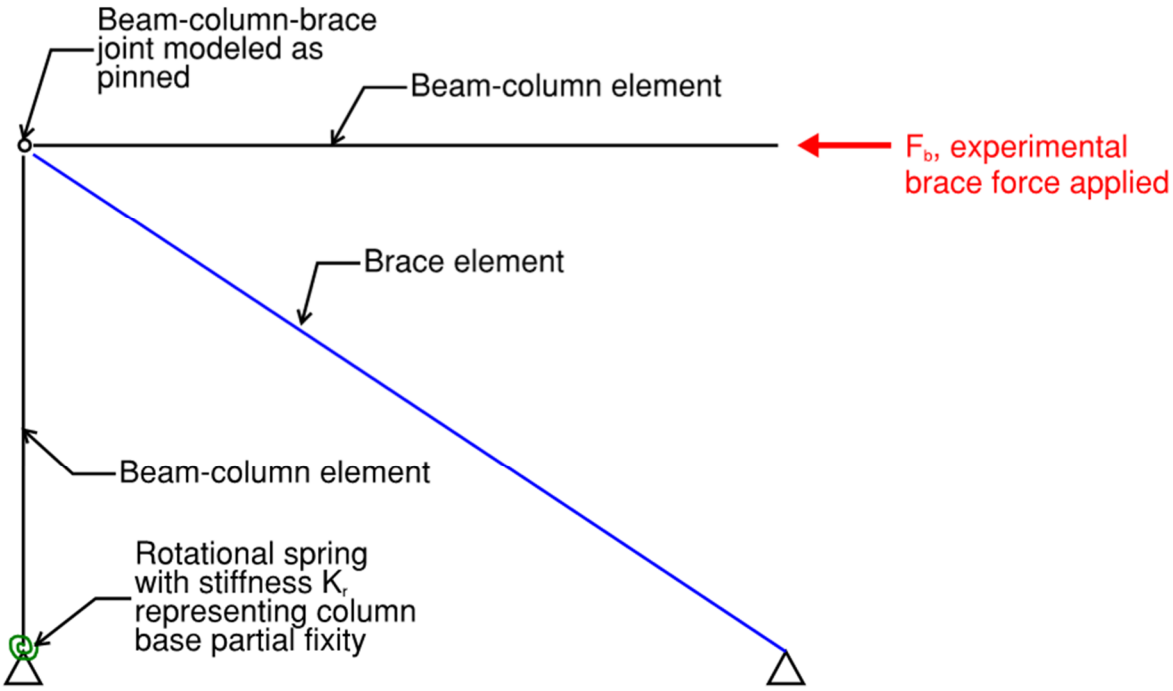

Figure 71: Depiction of model element, release, and applied load locations

The brace element was assigned a fictitious plastic stress-strain relationship and modulus of elasticity to induce the experimental brace force at the experimental frame displacement. Direct tension was applied longitudinally to a model of a single brace element to validate this approach. The stress-strain curve output from this model matched the prescribed stress-strain curves well (see **Figures 72** and **73**), so this approach was used for the full-frame model.

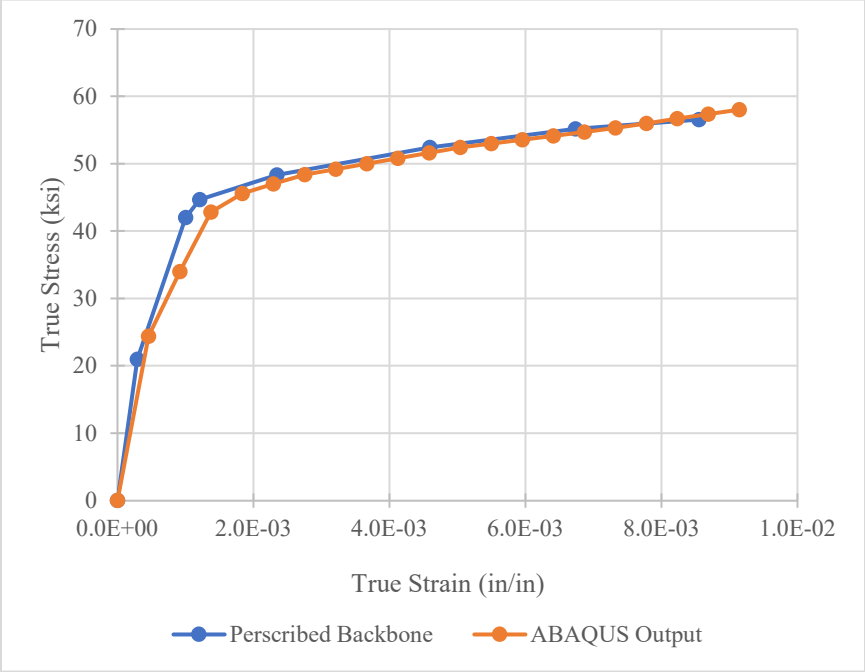

Figure 72: Prescribed true stress-true strain backbone (based on experimental backbone) in tension and ABAQUS output

A model was created for each point on the experimental backbone curve shown in **Figure 73**.

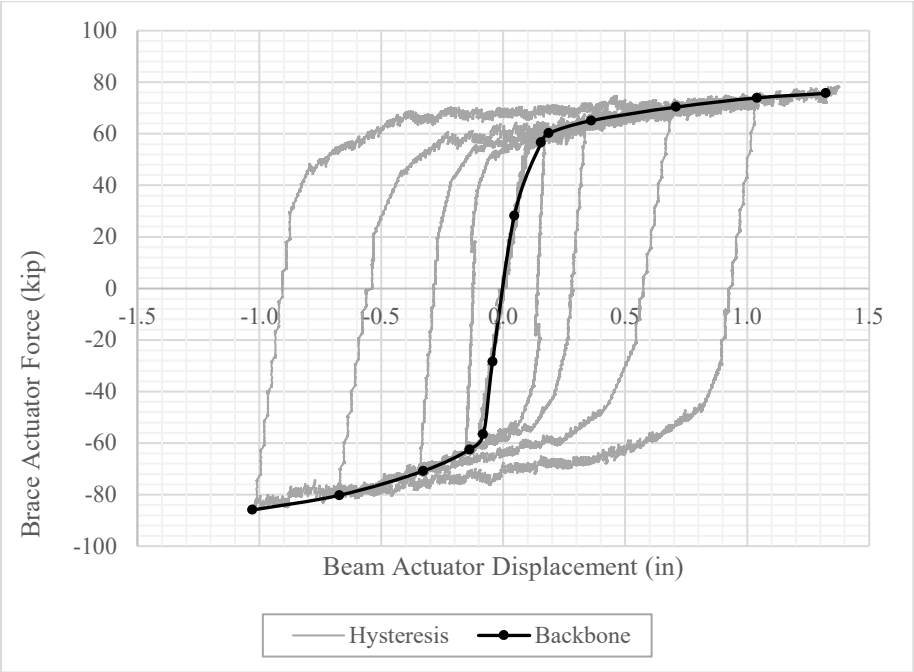

Figure 73: Experimental backbone curve compared to hysteresis

The stiffness of the column base, K_r, was varied until a satisfactory match to experimental results was found. A match to experimental beam force, experimental brace force, and frame displacement was desired, but the stiffness value was biased to the experimental brace force value as the displacement measurement contained the highest error due to system slip.

Model Results

Table 9 presents the stiffness associated with the column base for each procedure in tension.

Table 9: Column base stiffness derived from FEM tuned to frame experimental force-displacement behavior

Procedure	Column base stiffness (kip-in/rad)
1, Tension	20000
2, Tension	40000
3, Tension	50000
4, Tension	60000
5, Tension	100000
6, Tension	110000
7, Tension	130000

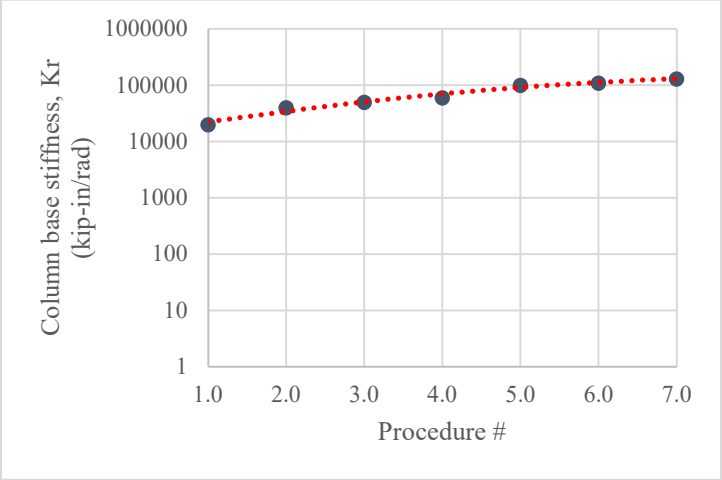

Figure 74: Column base stiffness from FEM tuned to frame experimental force-displacement behavior vs. procedure number

Procedures 1 through 3 were highly dependent of the slip observed at the bottom of the column, which is likely a cause for some of the error between the model and the experimental results at these lower frame displacement levels. Average and maximum

error between model and experimental results are presented in **Table 10** and **11**. **Table 10** includes all procedures; **Table 11** excludes Procedure 1-3.

Table 10: Average and maximum percent error, including all procedures

	% Difference Between Experimental and Model Beam Force	**% Difference Between Experimental and Model Brace Force**	**% Difference Between Experimental and Model Frame Displacement**
Average	0.006%	0.62%	10.60%
Maximum	0.029%	1.37%	37.29%

Table 11: Average and maximum percent error, excluding procedures 1-3

	% Difference Between Experimental and Model Beam Force	**% Difference Between Experimental and Model Brace Force**	**% Difference Between Experimental and Model Frame Displacement**
Average	0.005%	0.63%	5.68%
Maximum	0.013%	1.37%	15.76%

CHAPTER SIX

CONCLUSIONS AND RECOMMENDATIONS

Conclusions

The first objective of this research was to examine candidate design options for the connections of BRB to precast concrete frame members and their impacts on the design of the precast beams and columns. This objective was satisfied by examining a series of designs for various connection types; noting the implications on the design of the precast members for demands that would be induced by a BRB; and by satisfying the special moment frame detailing requirements of ACI 318-19 [14]. The designs can be divided into two categories: traditional gusset plate connections and connections aimed at eliminating gravity load transfer through the connection to the brace. **Table 12** summarizes the advantages and disadvantages of the UFM and KISS methods of force distribution. **Table 13** summarizes each of connection types examined that prevented gravity load transfer. Ultimately the gusset plate connection designed by UFM was selected for further investigation through the experimental program.

Table 12: Summary of gusset force distribution methodologies

Traditional Gusset Plate Connections		
Type	Advantages	Disadvantages
UFM	-Maintains moment equilibrium about work point without interface moments -Simple to implement -Recommended in AISC Steel Construction Manual	-Geometric constraints can cause oddly shaped or large gussets -Does not include effects of frame action
KISS	-Maintains moment equilibrium about work point -Simple to implement	-Requires large moments at interfaces for equilibrium -Can lead to over-conservative gussets -Does not include effects of frame action

Table 13: Summary of gravity load transfer eliminating connections

Connections to Eliminate Gravity Load Transfer		
Type	Advantages	Disadvantages
Slotted hole/air gap connections	-Eliminate gravity load transfer to connection and BRB -Use standard parts	-Air gaps lead to combined shear and bending in bolts, not generally recommended -Slotted holes allow bolts to be engaged at different times, could lead to earliest engaged bolts undergoing higher plastic deformation
Brace welded to bottom of corbel	-Circumvents attaching to beam entirely -Eliminates gravity load transfer -Compatible with narrower bays	-Not compatible with wider bays
Lug connection attached to corbel only	-Circumvents attaching to beam entirely -Eliminates gravity load transfer -Deterministic -Compatible with lug ended BRBs manufactured by CoreBrace	-Requires a large amount of corbel reinforcing, may cause constructability issues -Requires tighter erection tolerances

The second objective of this research was to determine the adequacy of the force distribution assumed by the UFM with a physical test on a connection within the precast BRBF identified. A physical specimen was fabricated that represented one bay of a BRBF within a 4-story parking garage structure in seismic design category B or C. The dimensions of the precast frame were selected to close to the average values from three different real example garages. Additionally, the precast members tested were full-length and the member connections to the reaction frame were very similar to what would be detailed as pinned in practice. The test specimen was subjected to a hysteresis derived from a BRB hysteresis backbone generated by CoreBrace. The hysteresis was imposed using two servo-controlled actuators: one inducing a horizonal displacement at the beam and one simulating the appropriate force response of the brace. Monitored strains along the gusset plate connected edges were used to generate stress distributions and interface forces. Additionally, out-of-plane motion of the precast specimen, curvature of the precast column, cracking in the precast members, strains in the corbel primary reinforcing bars, and in plane movement of the reaction frame were monitored.

From the results presented, it can be concluded that the precast BRBF tested was not close enough to the idealized pinned connections from Bjorhovde and Chakrabarti [22] and Gross and Cheok [21] that the UFM was verified with to assume this distribution. The idealized tests completed by Bjorhovde and Chakrabarti on steel connections and those completed by Maheri and Yazdani [23] on concrete connections did not include the effects of frame action and their boundary conditions were highly idealized. During the precast connection test, there was a positive percent error between

the theoretical and experimental shear interface forces and the negative percent error between the theoretical and experimental normal interface forces. This agrees with statements made by Lin [11] from tests on fixed frames that shear force induced by frame action is additive to interface brace force and normal force induced by frame action is subtractive. This implies that frame action has a significant effect of the distribution of forces at the gusset interfaces, even though the tested frame has more flexibility than the fixed frames tested in [10-13].

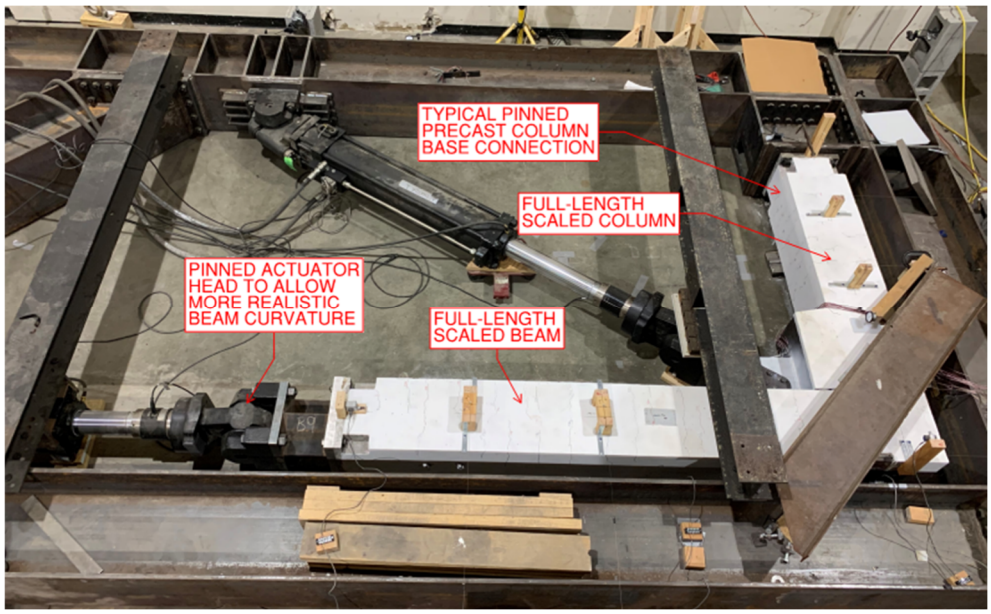

Figure 75: Realistic properties of precast BRBF tested

The connection designed and fabricated was robust enough to prevent failure despite the variation in load distribution from what was predicted by the UFM. At the maximum brace force tested, the beam and column saw 256% and 133% more shear load than was predicted by the UFM, respectively. The limiting component for shear at both the beam and column interfaces was the bars at their respective embedded plates. The factored capacities of all connection components that transmitted shear are listed in **Table**

14. The reduction factor for the embedded bars was 0.75 and the reduction factor for the welds was 0.9.

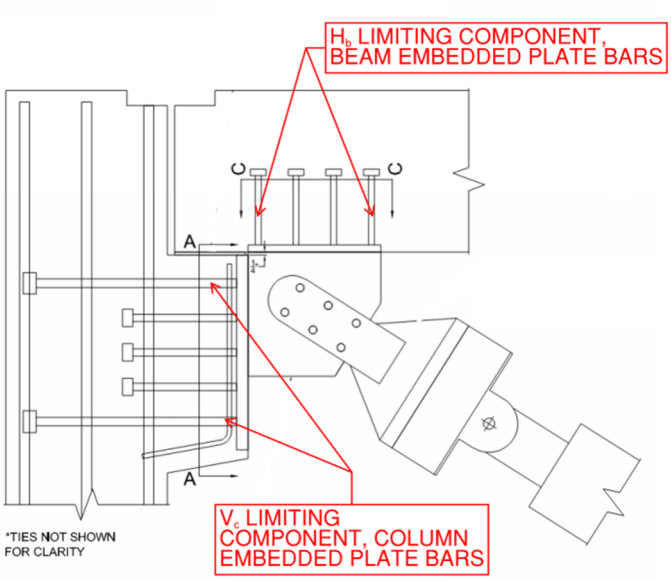

Figure 76: Components limiting capacity for transfer of H_b and V_c

Table 14: Summary of maximum error with respect to UFM predictions

Connection Component	UFM Force Component	Demand/Capacity Ratio	Th. UFM Force Resulting from Max. Brace Load in Tension (kip)	Exp. Force Resulting from Max. Brace Load in Tension (kip)	% Error	Component Factored Capacity (kip)
Beam embedded plate reinforcing bars	H_b	0.924	18.68	66.5	256%	72
Beam edge weld	H_b	0.516	18.68	66.5	256%	257
Column embedded plate reinforcing bars	V_c	0.257	17.46	40.62	133%	158
Column edge weld	V_c	0.339	17.46	40.62	133%	241

A failure may have occurred at the beam interface if connection components had been designed closer to the force expected from the UFM distribution. An unintentional source of conservatism was the beam and column welds being fabricated as 3/8” and not

3/16". It appears that typical design practices, such as using the minimum recommended fillet weld size in the AISC Steel Construction Manual and limiting embedded bar capacity by μ shear friction factor from ACI 318-19, may permit enough robustness in the design. However, designing to the capacity required per UFM alone would not have resulted in a sufficient design.

A simplistic finite element model was constructed the column base stiffness was tuned to match experimental member forces and displacements. The model was used to show that the changing distribution of forces to the beam and column could be explained by changes in column connection stiffness as the frame undergoes larger horizontal displacements, see **Figure 77** below.

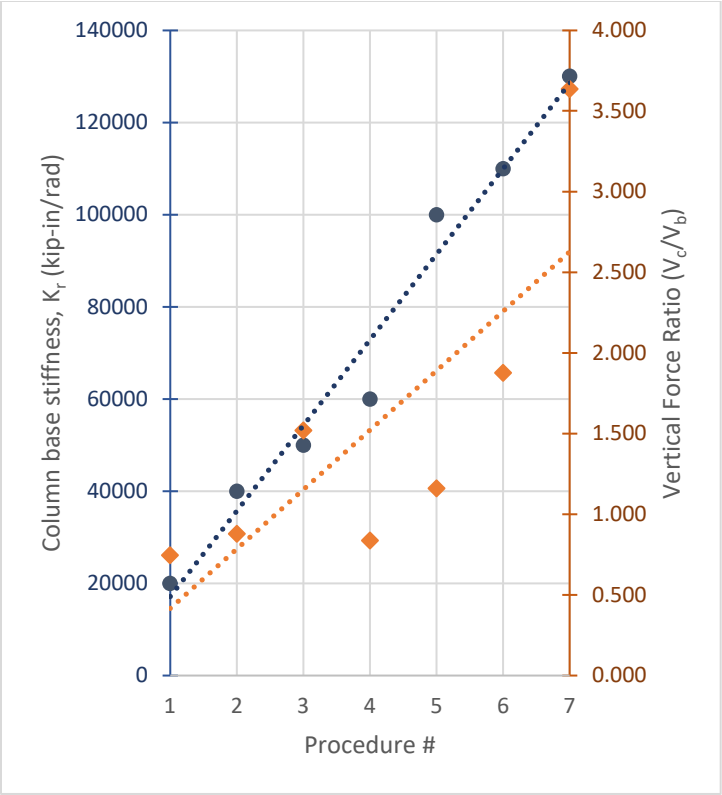

Figure 77: Increase of vertical force seen in column with increase in column base fixity from finite element model tuned to experimental frame response

Recommendations

Though this test is the first step in codifying the use of precast BRBFs, the singular specimen tested in this program is not enough to inform a robust design methodology on its own. Based on the results of this research, two paths for future work are proposed:

The first path would be to revisit the most promising deterministic connection, the lug connected only to the corbel, presented in Chapter 2 of this thesis. Preliminary analyses described in Chapter 3 showed that this connection is viable, but deeper consideration would need to be made regarding constructability. After the viability of this connection for both strength and constructability has been assessed, a connection could be designed and validated through testing. If such a connection is feasible, this would likely be the quickest and lowest risk path to adoption of precast BRBFs into building codes as it would require the fewest number of tests to fully validate.

The second path would be a more complex test program to understand how forces distribute through a gusset plate connection. This path would have two objectives: first, determine a methodology for distribution of forces to the precast members according to member stiffnesses; and second, quantify the effects of frame action on gusset plate interface force distribution in precast BRBFs. If this path is taken, designs that leverage standard cross-sections, member sizes, and connections could be codified. This path would likely require more experimental tests and time than development of the lug connection but would allow the use of common construction methods and material grades. The proposed steps of this test plan are detailed below and shown in **Figure 78**.

- Test initial precast specimen. Observe trends and deviations from assumptions of UFM. Determine possible reasons for these trends and deviations. This step has been completed as a part of this thesis.
- Create a simplistic finite element model neglecting effects of hairline cracks, correlated to experimental results of first test to begin to understand sources of discrepancy between UFM and physical test specimen. This step has been completed as a part of this thesis.
- FEA parametric study to inform general behavior with simple FEM3
- Create a simplistic finite element model including effects of hairline cracks, fixity at column base, and fixity at beam-column-brace joint correlated to experimental results of first test to further understand sources of discrepancy between UFM and physical test specimen. This step is ongoing.
    - This relationship between frame force-displacement response and column base stiffness could be used in a parametric study where the simplistic model is changed to include different brace angles and beam and column cross-sections. This could be useful in the creation of some preliminary recommendations for distribution of frame loads.
- Create more detailed finite element models correlated to the results of this test. Separate models could account for the effects of only frame action and only brace force, like the process of [10-13].
- Vary parameters in detailed finite element model such as column and corbel geometry, span, and reinforcing; beam geometry, span, and reinforcing; gusset

size; jumper plate connection size and layout; and gusset to BRB bolt size and pattern

- Identify setups most desirable for experimental testing from varied detailed finite element models
- Test these key setups experimentally
- Use the new experimental results to refine detailed finite element model results
- Observe trends in experimental and analytical data. Draw conclusions from these trends to inform robust design methodology for precast BRBFs

Figure 78: Detailed steps for understanding behavior of precast BRBFs using standard member sizes and connections. shaded steps completed in this thesis

APPENDICES

Appendix A

Hysteretic Stress-Strain Relationships of Untested Buckling-Restrained Braces

Strain Thresholds

Coy defined a set of equations to represent the shape of the hysteretic response of a BRB at each of four "strain thresholds." These strain thresholds were based on the cyclic stress-strain behavior of an A36 steel specimen taken from Kaufmann et al. [31]. Strain thresholds defined by Coy are as follows in **Table 15**:

Table 15: Strain thresholds as defined by Coy [15]

Level of Strain	**Strain Threshold**
Initial	0.005 in/in
Low	0.020 in/in
Medium	0.035 in/in
High	0.050 in/in

Strain thresholds were redefined to better fit the CoreBrace G Series test data that was used as a validation for this method of hysteresis prediction (see validation following). The new strain thresholds are as follows in **Table 16**:

Table 16: Adjusted strain thresholds

Level of Strain	**Strain Threshold**
Elastic	0.0014 in/in
Low	0.0130 in/in
Medium	0.0400 in/in
High	0.0500 in/in

The maximum strain for a given hysteresis loop determined what "level" of strain the loop was in and therefore what equations should be used to generate the shape of that loop. For example, a loop with a maximum strain of +/-0.01 would fall into the "low"

level of strain and the relationships associated with that level would be used to generate a hysteretic loop.

Initial Strain Relationships at Each Level

Coy does not provide the relationships he derived for each strain level. Using the same data his relationships were based on [31], relationships were reconstructed for each strain level.

The use of these reconstructed relationships is predicated on the ability to extract the strain hardening parameters (K_C, n_C, K_T, and n_T) from the max strain and stress of several different hysteresis loops for the brace in question. Because CoreBrace provided backbone curves (indicating only the max strain and stress in tension and compression for each loop) for the full-scale and scaled experimental braces, these parameters were able to be extracted.

Ramberg-Osgood and Strain Hardening Parameters

The Ramberg-Osgood equation is commonly used to represent the true stress-true strain behavior of ductile materials.

$$\tilde{\varepsilon} = \frac{\tilde{\sigma}}{E} + \left(\frac{\tilde{\sigma}}{K}\right)^n$$

The total true strain is composed of two parts, elastic strain, and plastic strain.

$$\tilde{\varepsilon} = \tilde{\varepsilon_e} + \tilde{\varepsilon_p}$$

The strain hardening parameters, *K* and *n* can be extracted for a given material if two or more stress and strain values are known in its plastic strain range. For two known stress and strain values, *K* and *n* can be determined by:

$$n = \frac{\log\left(\frac{\sigma_2}{\sigma_1}\right)}{\log\left(\frac{\varepsilon_2}{\varepsilon_1}\right)}$$

$$K = \frac{\sigma_1}{\varepsilon_1^n}$$

Relative Hysteresis Loop Shape Based on Strain Range

The strain hardening parameters for use in Hollomon's equation were determined for the A36 test specimen in Kaufmann's research. First, the engineering stresses and strains at the "tips" of each cycle were converted to true stress and strain by using the following equations.

$$\tilde{\varepsilon} = \ln(1 + \varepsilon)$$

$$\tilde{\sigma} = \sigma(1 + \varepsilon)$$

These equations above are only applicable before the advent of necking, reduction in stress after ultimate stress is reached. The A36 test specimen from Kaufmann's research and the G-series CoreBrace specimens that will be used to verify the estimation method presented in this paper do not experience necking in the region from which the strain hardening parameters were determined.

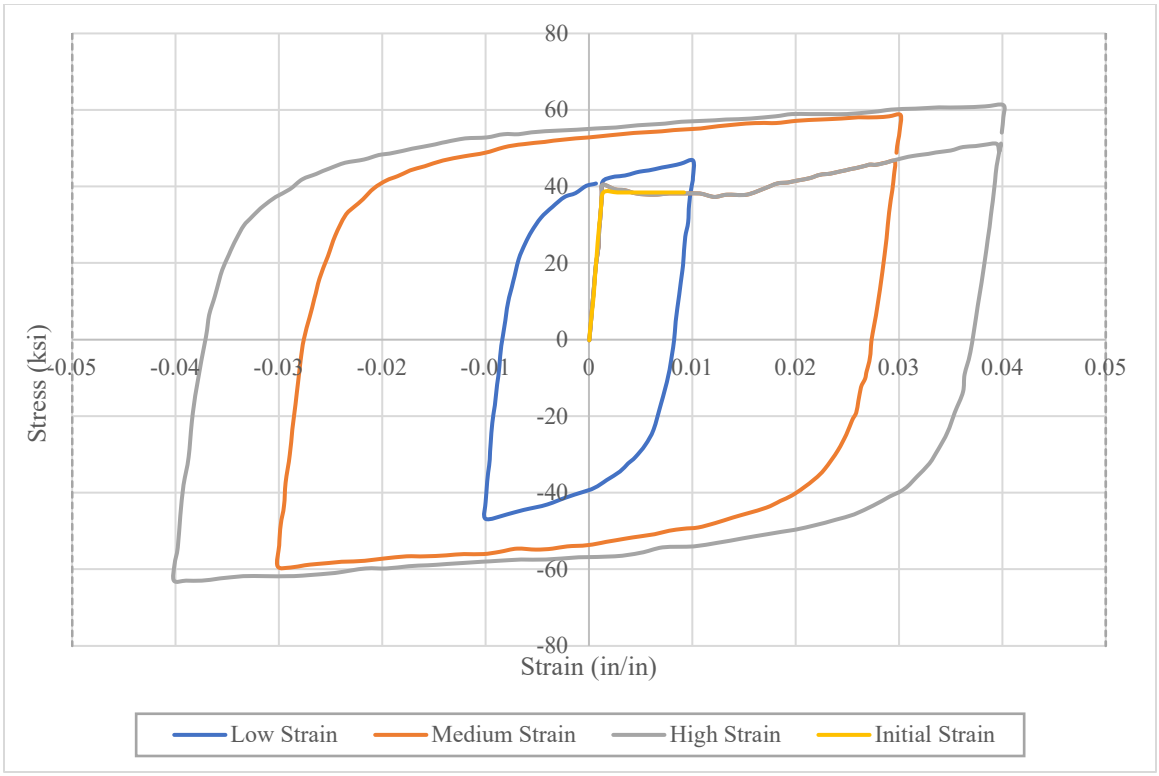

Figure 79: Cyclic test data from A36 specimen [30], strain ranges shown

Strain hardening parameters were determined for this A36 specimen by fitting a power regression through the "tips" (points of maximum stress and strain) for each cycle (both in tension and compression). See **Figures 77** and **78** following.

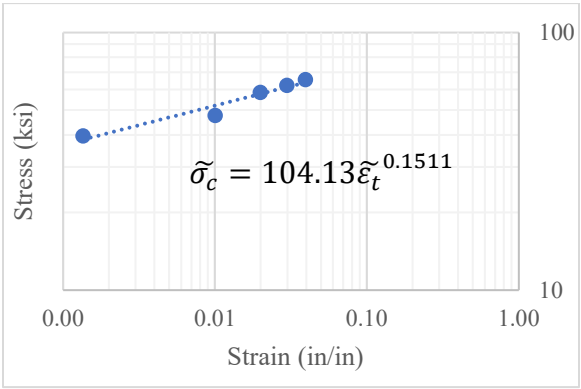

Figure 80: Strain hardening parameters extracted for A36 steel compression half-cycles, extracted from Kaufmann's data

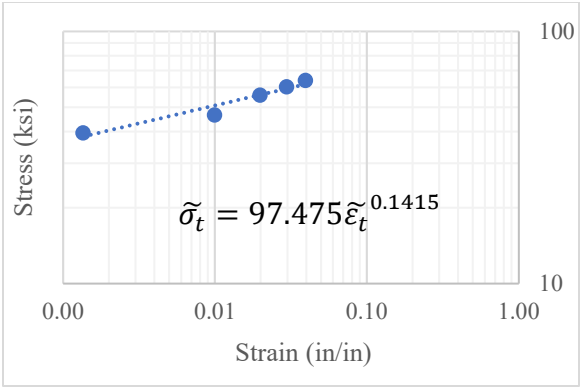

Figure 81: Strain hardening parameters extracted for A36 steel tension half-cycles, extracted from Kaufmann's data

The hysteresis loop at each strain level was broken into two symmetric half cycles and each half cycle was broken into four linear relationships. Four relationships were deemed to be representative enough of the curved portion of each half cycle. The bounds of these linear relationships were picked to best mimic the shape of the curved portion of each half cycle. The bounds were then expressed as percentages of max strain (ε_{max}), maximum compressive stress ($\sigma_{max,C}$), and maximum tensile stress ($\sigma_{max,T}$) and linear relationships were fit between each set of bounds (see **Figure 79** following).

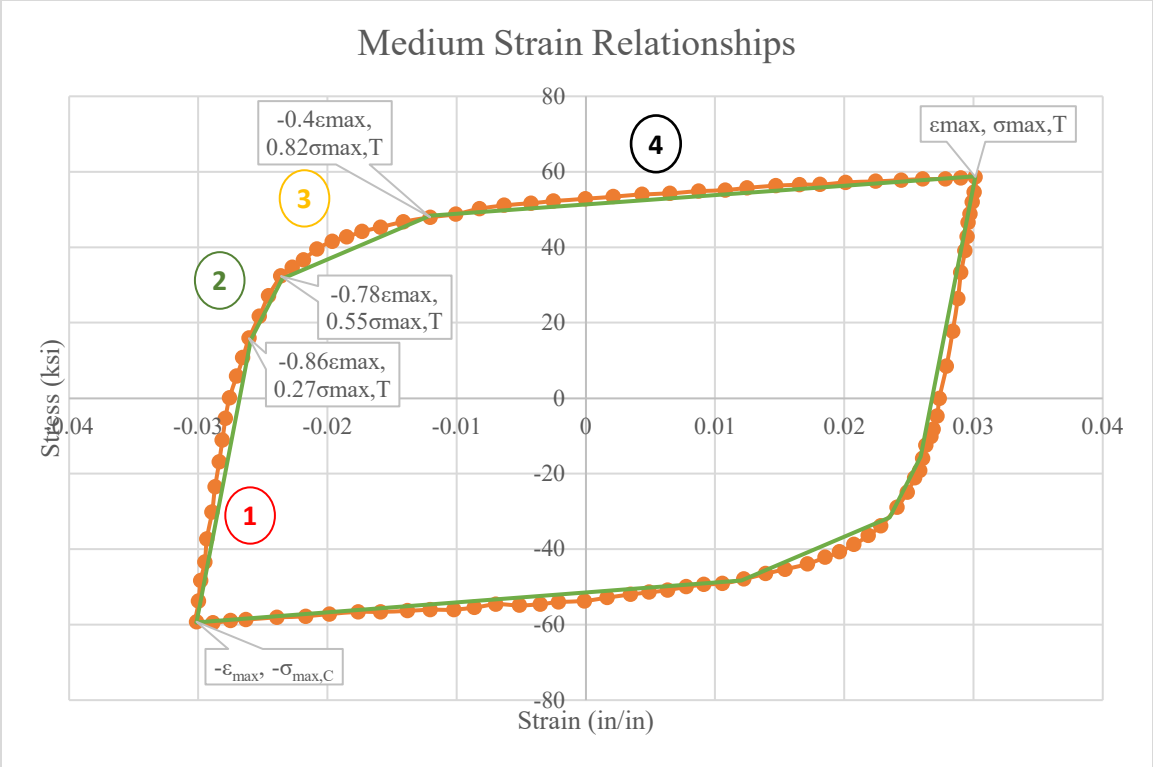

Figure 82: Strain and stress at bounds as percentages of max strain, max compressive stress, and max tensile stress

The initially determined relationships are as follows in **Table 17**.

Table 17: Initial version of multiple stress-strain relationships for each strain level

Level of Strain	**Stress-Strain Relationship(s)***
Elastic	For $\varepsilon \leq 0.0014$: $\sigma = \varepsilon E$
Low	$\sigma_{max,C} = K_C * \varepsilon_{max}^{n_C}$ $\sigma_{max,T} = K_T * \varepsilon_{max}^{n_T}$ Segment 1: from $-\varepsilon_{max}$ to $-0.78\varepsilon_{max}$: $\sigma = \left(\frac{0.21\sigma_{max,T} + \sigma_{max,C}}{0.22\varepsilon_{max}}\right)(\varepsilon + \varepsilon_{max}) - \sigma_{max,C}$ Segment 2: from $-0.78\varepsilon_{max}$ to $-0.62\varepsilon_{max}$: $\sigma = \left(\frac{2.06\sigma_{max,T}}{\varepsilon_{max}}\right)(\varepsilon + 0.78\varepsilon_{max}) + 0.21\sigma_{max,T}$ Segment 3: from $-0.62\varepsilon_{max}$ to $-0.35\varepsilon_{max}$: $\sigma = \left(\frac{0.74\sigma_{max,T}}{\varepsilon_{max}}\right)(\varepsilon + 0.62\varepsilon_{max}) + 0.54\sigma_{max,T}$ Segment 4: from $-0.35\varepsilon_{max}$ to ε_{max}: $\sigma = \left(\frac{0.19\sigma_{max,T}}{\varepsilon_{max}}\right)(\varepsilon + 0.35\varepsilon_{max}) + 0.74\sigma_{max,T}$
Medium	$\sigma_{max,C} = K_C * \varepsilon_{max}^{n_C}$ $\sigma_{max,T} = K_T * \varepsilon_{max}^{n_T}$ Segment 1: from $-\varepsilon_{max}$ to $-0.86\varepsilon_{max}$: $\sigma = \left(\frac{0.27\sigma_{max,T} + \sigma_{max,C}}{0.14\varepsilon_{max}}\right)(\varepsilon + \varepsilon_{max}) - \sigma_{max,C}$ Segment 2: from $-0.86\varepsilon_{max}$ to $-0.78\varepsilon_{max}$: $\sigma = \left(\frac{3.5\sigma_{max,T}}{\varepsilon_{max}}\right)(\varepsilon + 0.86\varepsilon_{max}) + 0.27\sigma_{max,T}$ Segment 3: from $-0.78\varepsilon_{max}$ to $-0.4\varepsilon_{max}$: $\sigma = \left(\frac{0.71\sigma_{max,T}}{\varepsilon_{max}}\right)(\varepsilon + 0.78\varepsilon_{max}) + 0.55\sigma_{max,T}$ Segment 4: from $-0.4\varepsilon_{max}$ to ε_{max}: $\sigma = \left(\frac{0.13\sigma_{max,T}}{\varepsilon_{max}}\right)(\varepsilon + 0.4\varepsilon_{max}) + 0.82\sigma_{max,T}$
High	$\sigma_{max,C} = K_C * \varepsilon_{max}^{n_C}$ $\sigma_{max,T} = K_T * \varepsilon_{max}^{n_T}$ Segment 1: from $-\varepsilon_{max}$ to $-0.90\varepsilon_{max}$: $\sigma = \left(\frac{0.18\sigma_{max,T} + \sigma_{max,C}}{0.1\varepsilon_{max}}\right)(\varepsilon + \varepsilon_{max}) - \sigma_{max,C}$ Segment 2: from $-0.9\varepsilon_{max}$ to $-0.75\varepsilon_{max}$: $\sigma = \left(\frac{2.87\sigma_{max,T}}{\varepsilon_{max}}\right)(\varepsilon + 0.9\varepsilon_{max}) + 0.18\sigma_{max,T}$ Segment 3: from $-0.75\varepsilon_{max}$ to $-0.51\varepsilon_{max}$: $\sigma = \left(\frac{0.75\sigma_{max,T}}{\varepsilon_{max}}\right)(\varepsilon + 0.75\varepsilon_{max}) + 0.61\sigma_{max,T}$ Segment 4: from $-0.51\varepsilon_{max}$ to ε_{max}: $\sigma = \left(\frac{0.14\sigma_{max,T}}{\varepsilon_{max}}\right)(\varepsilon + 0.51\varepsilon_{max}) + 0.79\sigma_{max,T}$

*Relationships written out for one half-cycle

Validation of Initial Relationships on CoreBrace G Series Tests

To validate the new relationships, they were applied to existing test data from four CoreBrace G Series braces. Two specimens (1G and 2G) had cores with 12 sq. in. cross-sectional areas and yielding core lengths of 132-1/2 in. The other two specimens (3G and 4G) had 27 sq. in. cross-sectional areas and yielding core lengths of 144-7/16 in.

The strain hardening parameters were determined for each of the four braces and the strain relationships for the corresponding strain level were applied to each loop. The actual hysteresis for each brace (solid line) and predicted hysteresis (dashed line) are presented following in **Figures 80** through **83**.

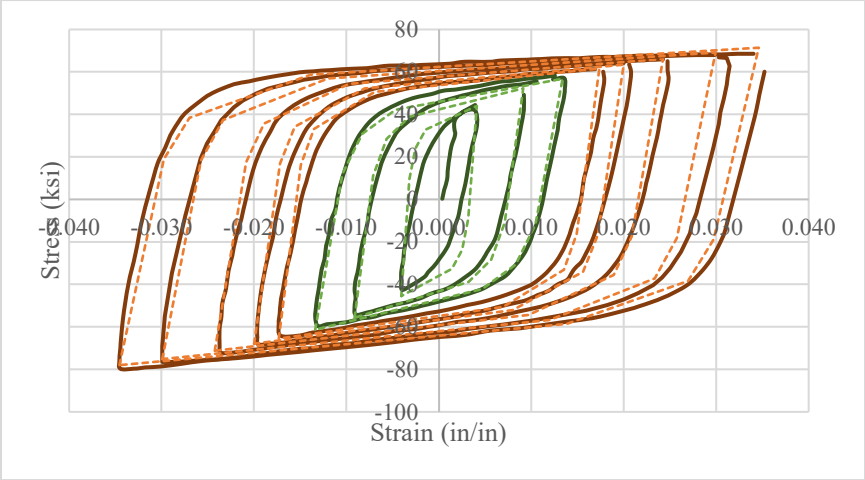

Figure 83: Actual and predicted stress-strain relationship for specimen 1G

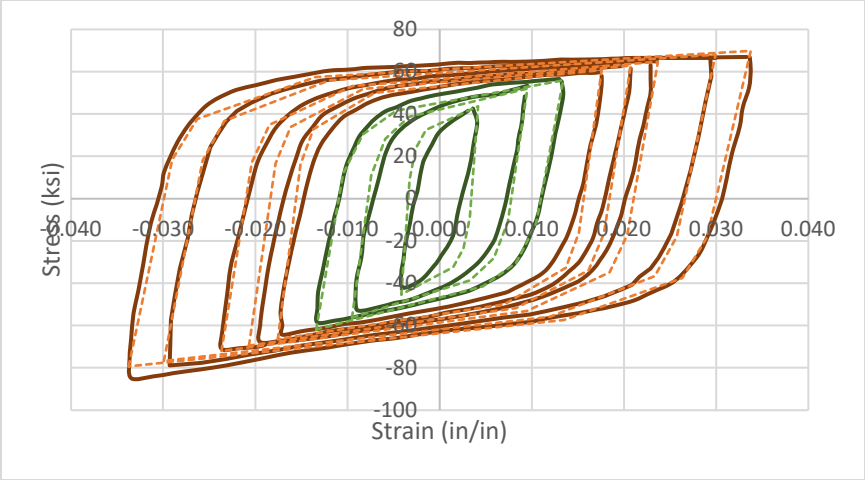

Figure 84: Actual and predicted stress-strain relationship for specimen 2G

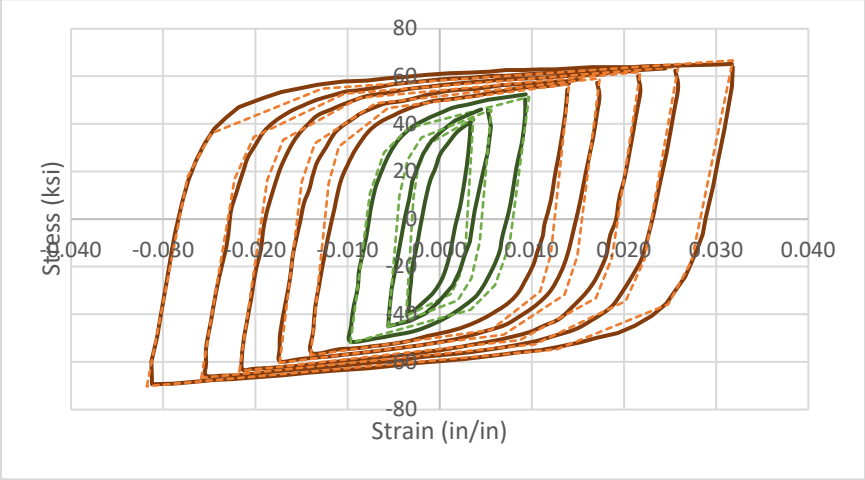

Figure 85: Actual and predicted stress-strain relationship for specimen 3G

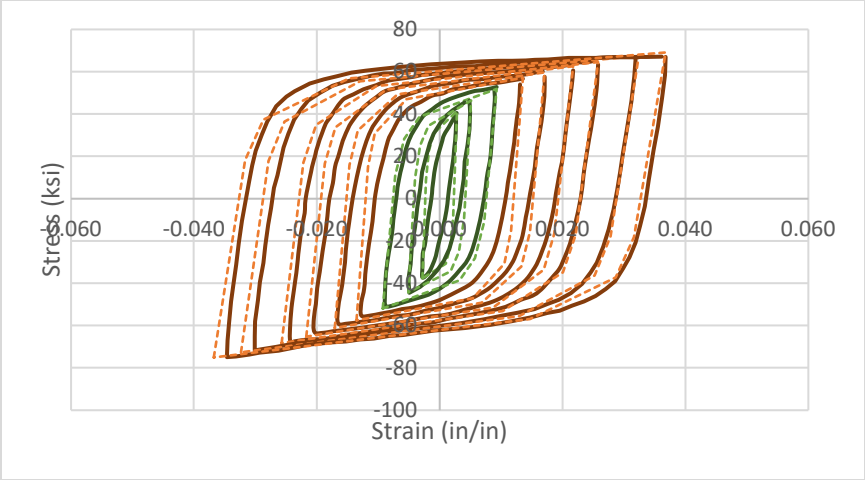

Figure 86: Actual and predicted stress-strain relationship for specimen 4G

Comparison between the test hysteresis and the predicted hysteresis indicated that this method of prediction yielded a satisfactory level of accuracy in predicting strain hardening behavior and the shape of the hysteresis loops at different strain levels. It was deemed to be an acceptable method of predicting hysteresis for a physically untested buckling-restrained brace.

Prediction of Hysteretic Behavior of Experimental Braces

The backbone curve provided by CoreBrace included two cycles: one with a maximum strain corresponding to yield strain and the other with maximum strain corresponding to two-percent story drift of the frame (see **Figure 84** following). Strain hardening parameters were extracted from this backbone curve following the procedure described previously (see **Figures 85** and **86** following).

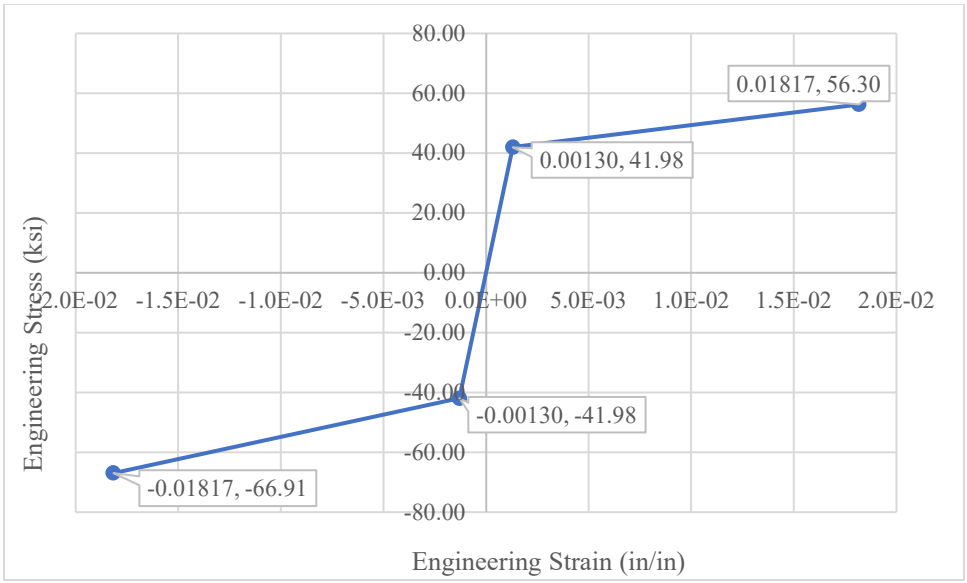

Figure 87: Stress-strain backbone curve provided by CoreBrace with points at brace yield and strain due to two-percent story drift of the frame

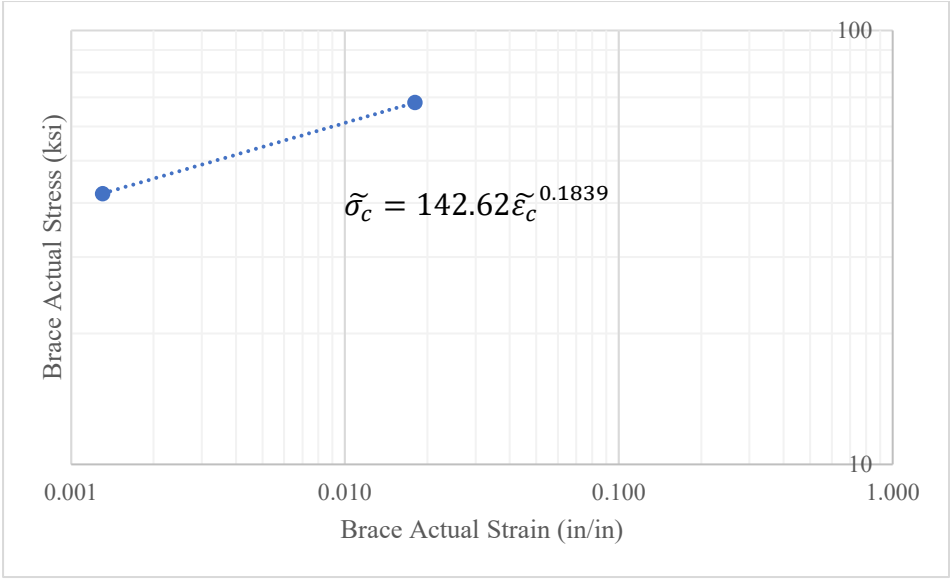

Figure 88: Strain hardening parameters for brace in compression

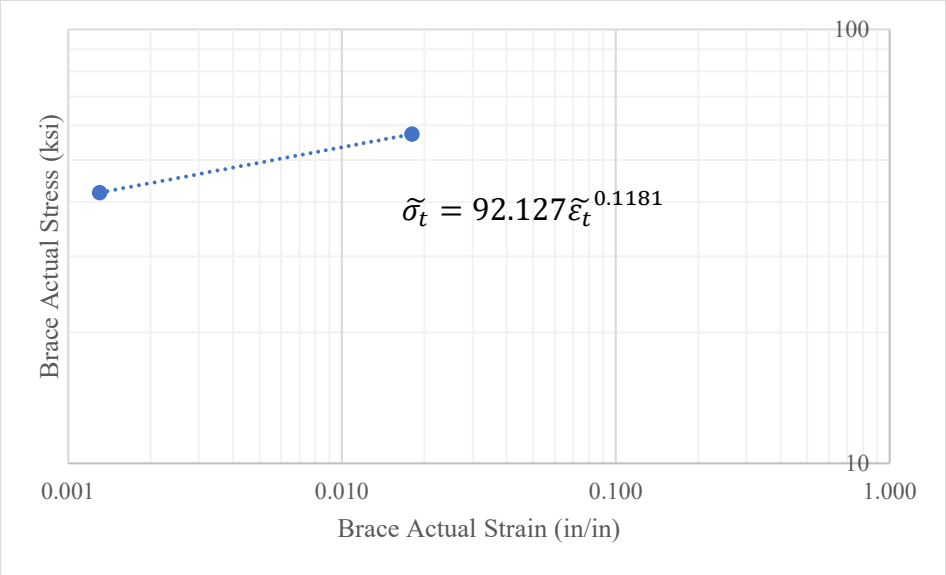

Figure 89: Strain hardening parameters for brace in tension

Because the strain at two-percent story drift was designed to correspond to a brace force equal to the maximum capacity of the experimental actuators, all of the strain levels described for cyclic test qualification of buckling-restrained braces in AISC 341-16 Section K3.4c could not developed in this experiment. For the purposes of this experiment the connection would be subjected to the stress-strain response of the brace at cycles corresponding to strains of $0.5\varepsilon_y$, ε_y, $0.125\varepsilon_{2\%}$, $0.25\varepsilon_{2\%}$, $0.5\varepsilon_{2\%}$, $0.75\varepsilon_{2\%}$, and $\varepsilon_{2\%}$.

Table 18: Required loading sequence for BRB subassemblage test specimen per AISC 341-16

Description	**Number of Cycles**
ε_y	2
$0.5\varepsilon_{2\%}$	2
$\varepsilon_{2\%}$	2
$1.5\varepsilon_{2\%}$	2
$2.0\varepsilon_{2\%}$	2

Table 19: Loading protocol connection will be subjected to, based on stress-strain response of brace at different strain levels

Description	Strain Level	Strain	Number of Cycles
$0.5\varepsilon_y$	Elastic	0.000652	2
ε_y	Elastic	0.001303	2
$0.125\varepsilon_{2\%}$	Low	0.002271	2
$0.25\varepsilon_{2\%}$	Low	0.004542	2
$0.5\varepsilon_{2\%}$	Low	0.009085	2
$0.75\varepsilon_{2\%}$	Medium	0.013627	2
$\varepsilon_{2\%}$	Medium	0.018169	2

Preliminary hysteresis loops were generated for the full-scale and scaled braces based on the initially determined strain levels and the stress-strain relationships that applied to each strain level. These preliminary hysteresis loops are presented in **Figure 87** and **Figure 88** following.

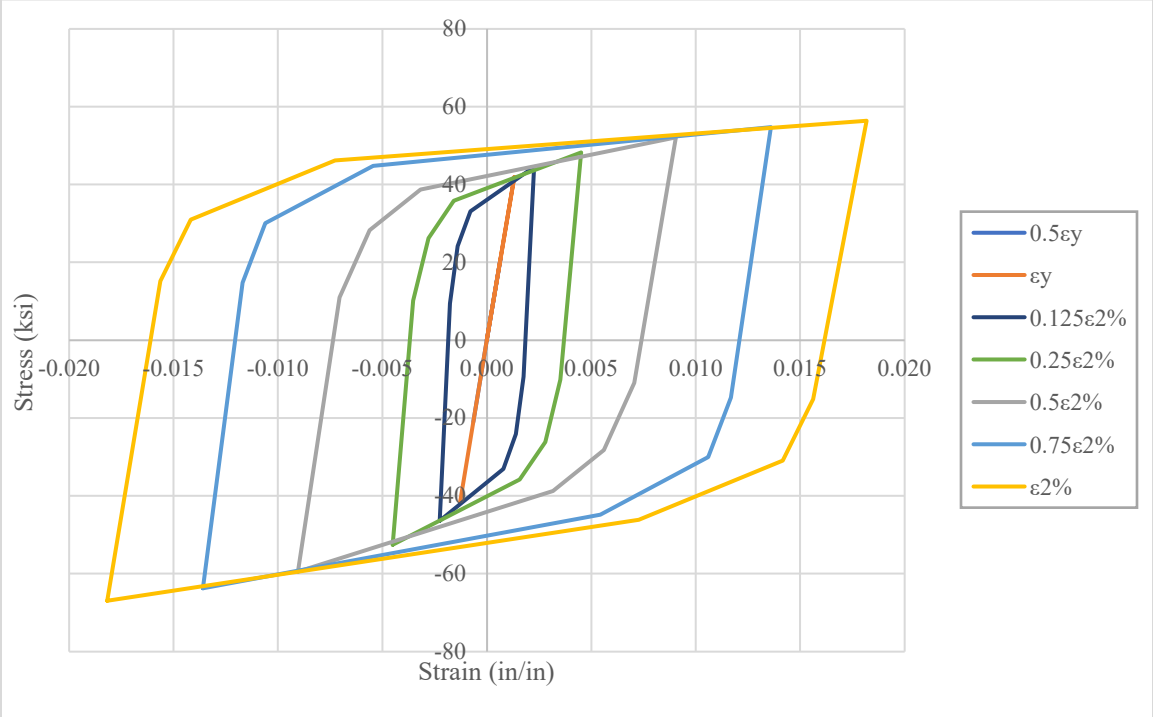

Figure 90: Preliminary hysteretic stress-strain relationships for full-scale brace at predetermined strain levels

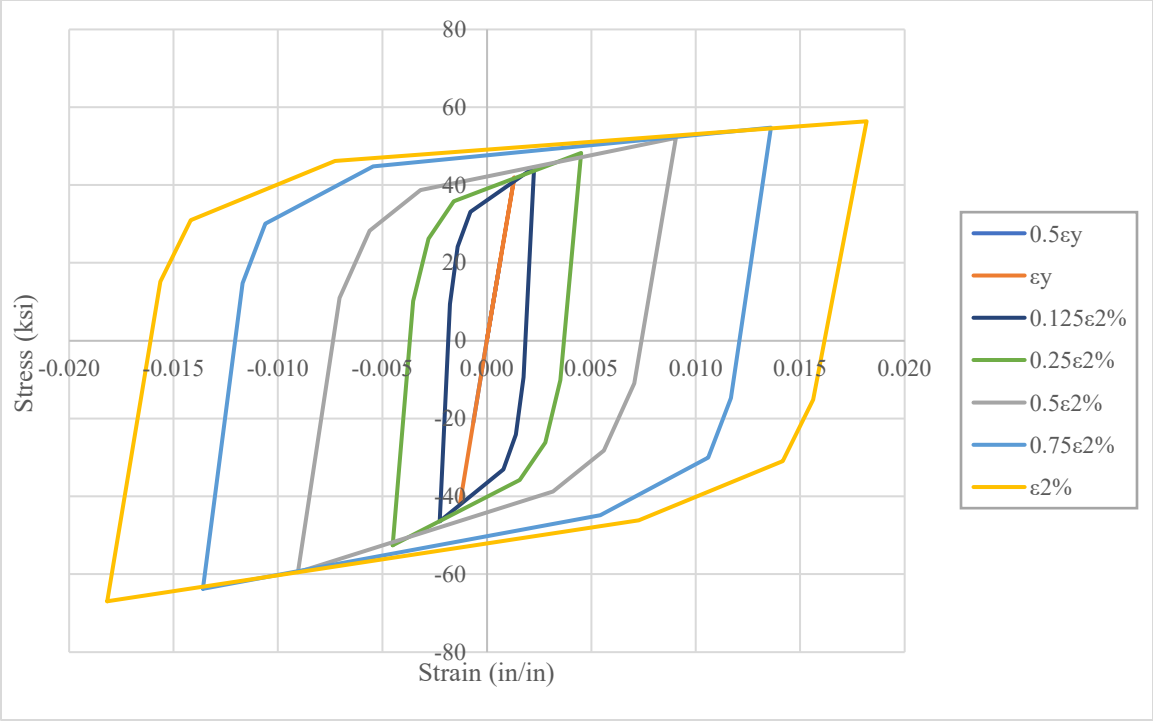

Figure 91: Preliminary hysteretic stress-strain relationships for scaled brace at predetermined strain levels

Both preliminary hystereses predict the anticipated increase in strength due to strain hardening with increased strain and each loop's shape resembles shapes seen in actual BRB test data. One unexpected trait of these predictions is that in some cases there is a softening-like behavior where the stress predicted at the max strain of a lower cycle is greater than the stress predicted at that same strain in the next cycle. For example, in the cycle corresponding to $0.25\varepsilon_{2\%}$ (0.004542) the max stress in tension is 48 ksi and in the cycle corresponding to $0.5\varepsilon_{2\%}$ (0.009085) the stress at a strain of 0.004542 is only 46 ksi. When this methodology was used to predict the hysteretic behavior of the CoreBrace specimens this softening-like behavior did not occur.

Adjusted Strain Relationships at Each Level

The reason for the softening-like behavior in the predicted hysteresis for the experimental specimens and not for the CoreBrace specimens is unknown. Because this methodology is only an estimation of the hysteretic behavior, it was deemed acceptable to manually adjust the relationships so that the softening was eliminated in the experimental specimens. Slight manual adjustments to the "low" and "medium" strain relationships were made; the changed values are indicated in **Table 20** in red text. These ratios were increased incrementally by an arbitrary amount until the softening was eliminated. The adjusted relationships are given following in **Table 20**.

Table 20: Adjusted stress-strain relationships based on multiple strain levels

Level of Strain	**Stress-Strain Relationship(s)***
Elastic	For $\varepsilon \leq 0.0014$: $$\sigma = \varepsilon E$$
Low	$$\sigma_{max,C} = K_C * \varepsilon_{max}^{n_C}$$ $$\sigma_{max,T} = K_T * \varepsilon_{max}^{n_T}$$ Segment 1: from $-\varepsilon_{max}$ to $-0.78\varepsilon_{max}$: $$\sigma = \left(\frac{0.21\sigma_{max,T} + \sigma_{max,C}}{0.22\varepsilon_{max}}\right)(\varepsilon + \varepsilon_{max}) - \sigma_{max,C}$$ Segment 2: from $-0.78\varepsilon_{max}$ to $-0.62\varepsilon_{max}$: $$\sigma = \left(\frac{2.06\sigma_{max,T}}{\varepsilon_{max}}\right)(\varepsilon + 0.78\varepsilon_{max}) + 0.30\sigma_{max,T}$$ Segment 3: from $-0.62\varepsilon_{max}$ to $-0.35\varepsilon_{max}$: $$\sigma = \left(\frac{0.74\sigma_{max,T}}{\varepsilon_{max}}\right)(\varepsilon + 0.62\varepsilon_{max}) + 0.63\sigma_{max,T}$$ Segment 4: from $-0.35\varepsilon_{max}$ to ε_{max}: $$\sigma = \left(\frac{0.19\sigma_{max,T}}{\varepsilon_{max}}\right)(\varepsilon + 0.35\varepsilon_{max}) + 0.74\sigma_{max,T}$$
Medium	$$\sigma_{max,C} = K_C * \varepsilon_{max}^{n_C}$$ $$\sigma_{max,T} = K_T * \varepsilon_{max}^{n_T}$$ Segment 1: from $-\varepsilon_{max}$ to $-0.86\varepsilon_{max}$: $$\sigma = \left(\frac{0.27\sigma_{max,T} + \sigma_{max,C}}{0.14\varepsilon_{max}}\right)(\varepsilon + \varepsilon_{max}) - \sigma_{max,C}$$ Segment 2: from $-0.86\varepsilon_{max}$ to $-0.78\varepsilon_{max}$: $$\sigma = \left(\frac{3.5\sigma_{max,T}}{\varepsilon_{max}}\right)(\varepsilon + 0.86\varepsilon_{max}) + 0.40\sigma_{max,T}$$ Segment 3: from $-0.78\varepsilon_{max}$ to $-0.4\varepsilon_{max}$: $$\sigma = \left(\frac{0.71\sigma_{max,T}}{\varepsilon_{max}}\right)(\varepsilon + 0.78\varepsilon_{max}) + 0.64\sigma_{max,T}$$ Segment 4: from $-0.4\varepsilon_{max}$ to ε_{max}: $$\sigma = \left(\frac{0.13\sigma_{max,T}}{\varepsilon_{max}}\right)(\varepsilon + 0.4\varepsilon_{max}) + 0.82\sigma_{max,T}$$
High	$$\sigma_{max,C} = K_C * \varepsilon_{max}^{n_C}$$ $$\sigma_{max,T} = K_T * \varepsilon_{max}^{n_T}$$ Segment 1: from $-\varepsilon_{max}$ to $-0.90\varepsilon_{max}$: $$\sigma = \left(\frac{0.18\sigma_{max,T} + \sigma_{max,C}}{0.1\varepsilon_{max}}\right)(\varepsilon + \varepsilon_{max}) - \sigma_{max,C}$$ Segment 2: from $-0.9\varepsilon_{max}$ to $-0.75\varepsilon_{max}$: $$\sigma = \left(\frac{2.87\sigma_{max,T}}{\varepsilon_{max}}\right)(\varepsilon + 0.9\varepsilon_{max}) + 0.18\sigma_{max,T}$$ Segment 3: from $-0.75\varepsilon_{max}$ to $-0.51\varepsilon_{max}$: $$\sigma = \left(\frac{0.75\sigma_{max,T}}{\varepsilon_{max}}\right)(\varepsilon + 0.75\varepsilon_{max}) + 0.61\sigma_{max,T}$$ Segment 4: from $-0.51\varepsilon_{max}$ to ε_{max}: $$\sigma = \left(\frac{0.14\sigma_{max,T}}{\varepsilon_{max}}\right)(\varepsilon + 0.51\varepsilon_{max}) + 0.79\sigma_{max,T}$$

The results of the application of these adjusted relationships to the experimental braces are shown following in **Figures 89** and **90**.

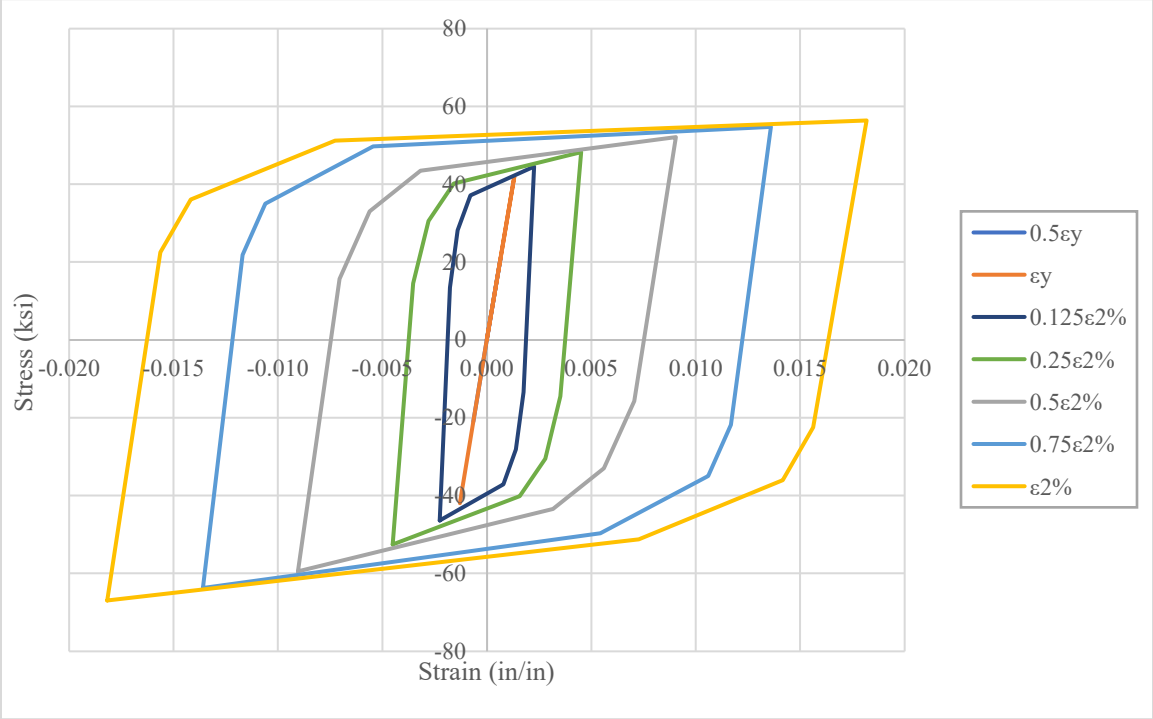

Figure 92: Adjusted hysteretic stress-strain relationships for full-scale brace at predetermined strain levels

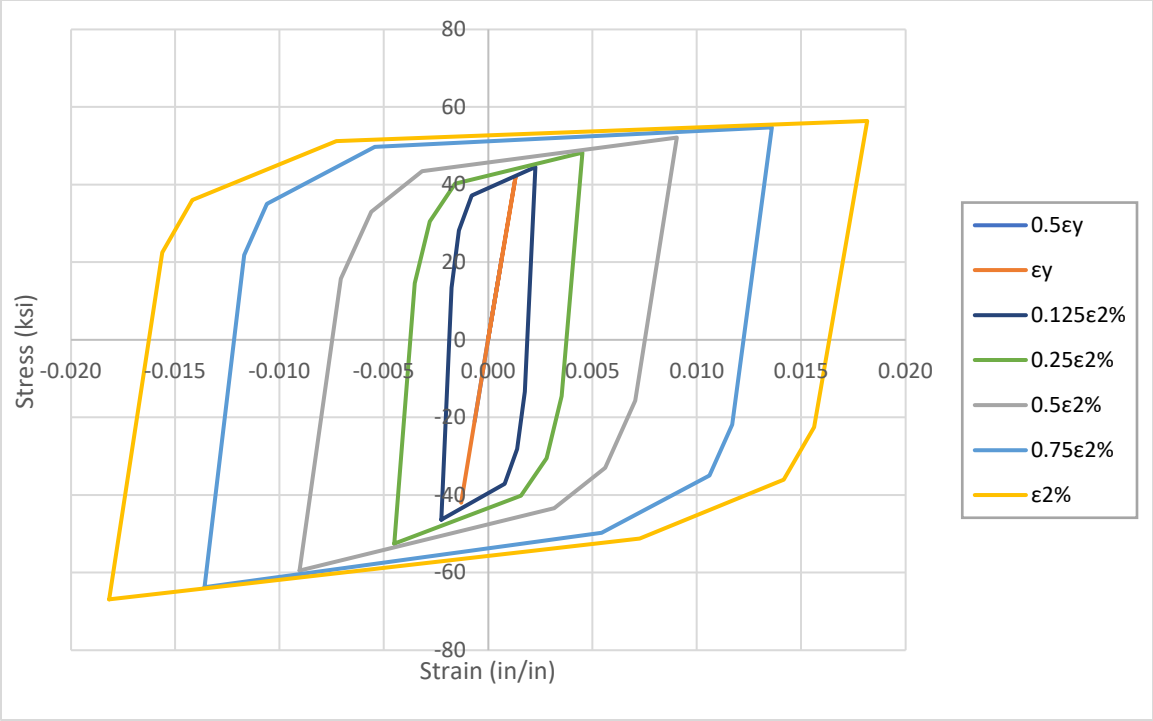

Figure 93: Adjusted hysteretic stress-strain relationships for scaled brace at predetermined strain levels

Validation of Adjusted Relationships on CoreBrace G Series Tests

To verify that these relationships were still representative of real hysteresis data, they were applied to the same CoreBrace G-Series braces. The resulting hystereses and actual hystereses are shown following in **Figures 91-94**.

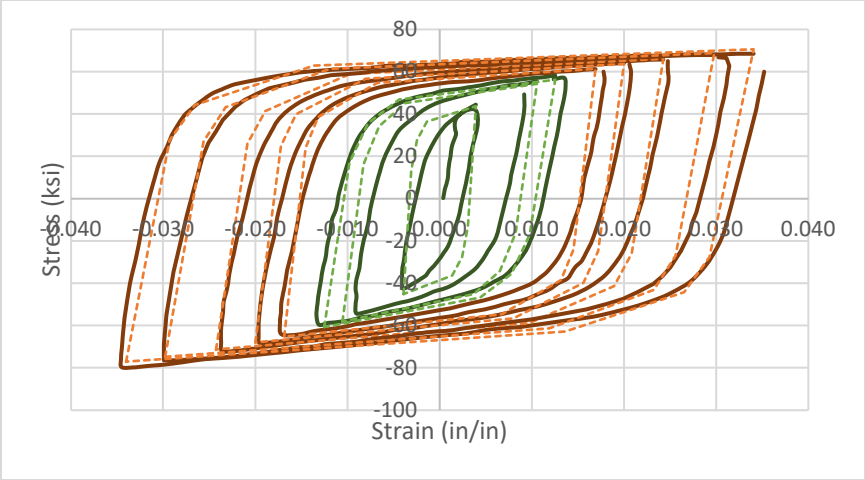

Figure 94: Actual and adjusted predicted stress-strain relationship for specimen 1G

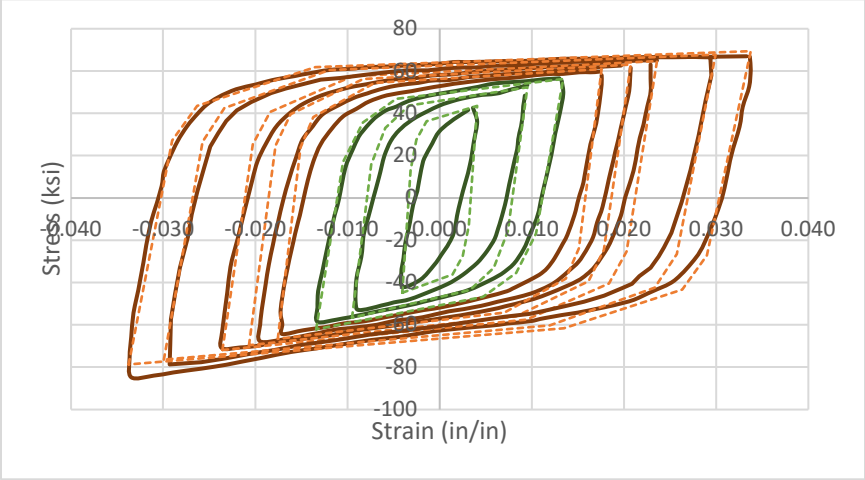

Figure 95: Actual and adjusted predicted stress-strain relationship for specimen 2G

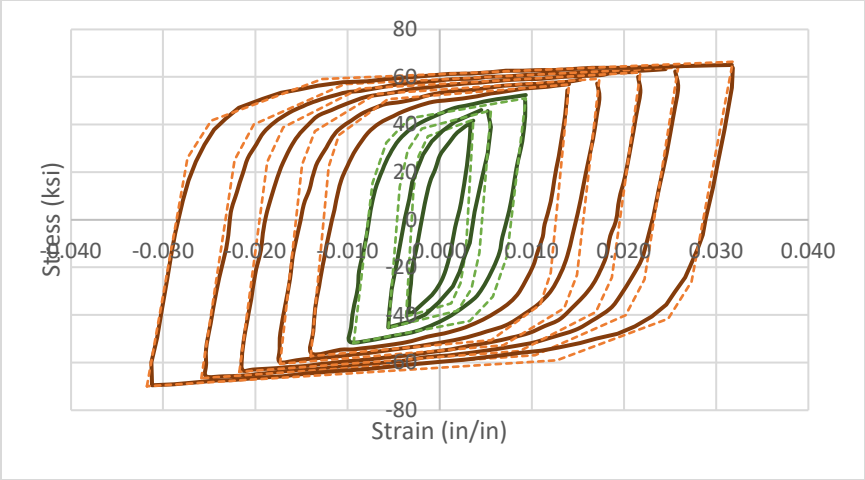

Figure 96: Actual and adjusted predicted stress-strain relationship for specimen 3G

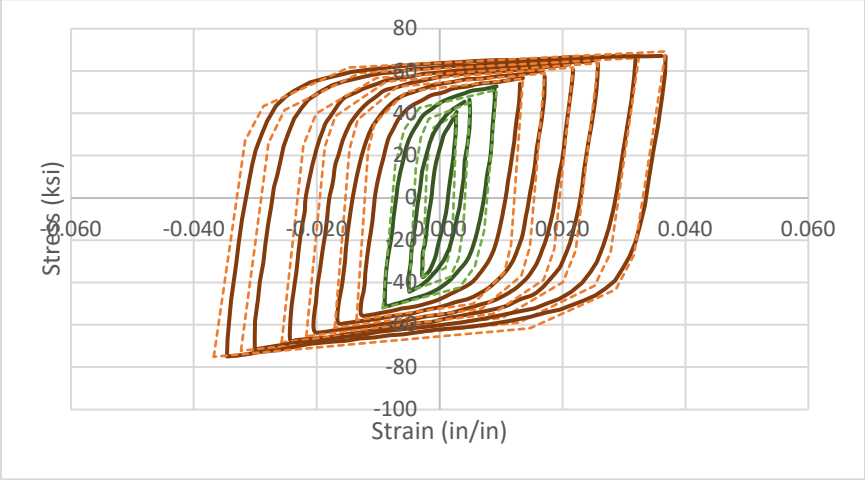

Figure 97: Actual and adjusted predicted stress-strain relationship for specimen 4G

These adjusted relationships provided a similar level of accuracy to the first set of relationships and, as such, were deemed appropriate for hysteresis prediction.

Final Predicted Hysteresis

Because the adjusted relationships were fairly accurate and did not result in softening-like behavior in the hystereses generated for the experimental braces they were

used for the final experimental hystereses. The experimental hystereses using the adjusted relationships are shown again following in **Figures 95** and **96**.

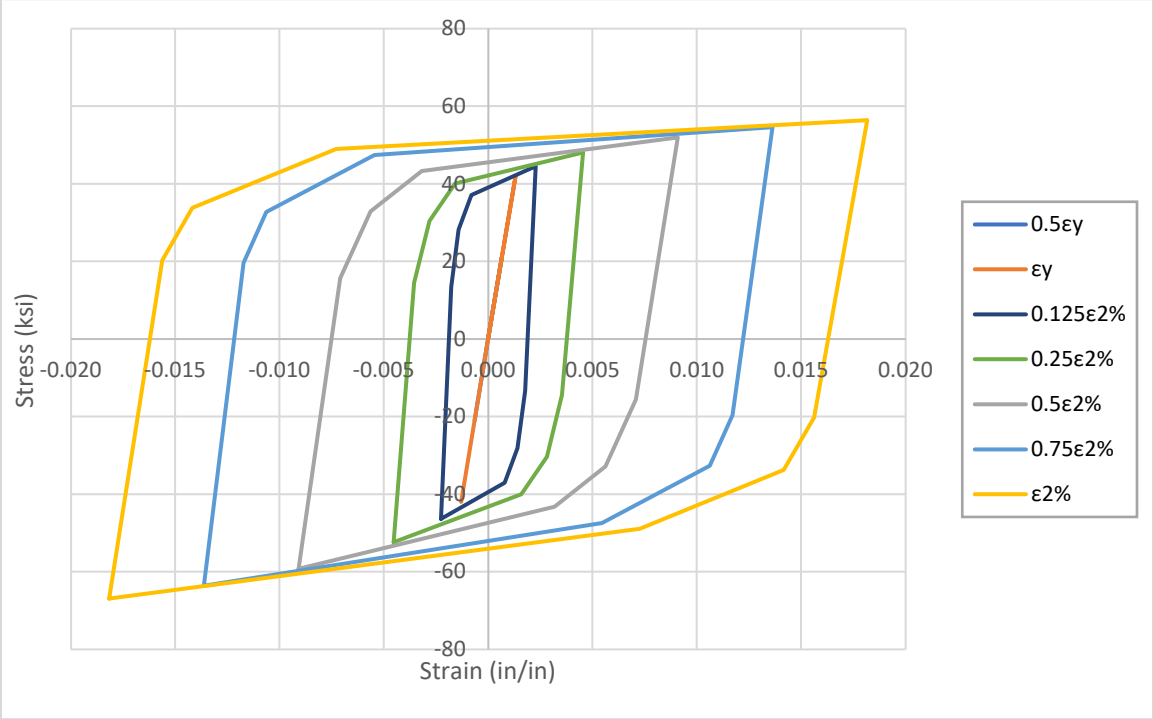

Figure 98: Final hysteretic stress-strain relationships for full-scale brace at predetermined strain levels

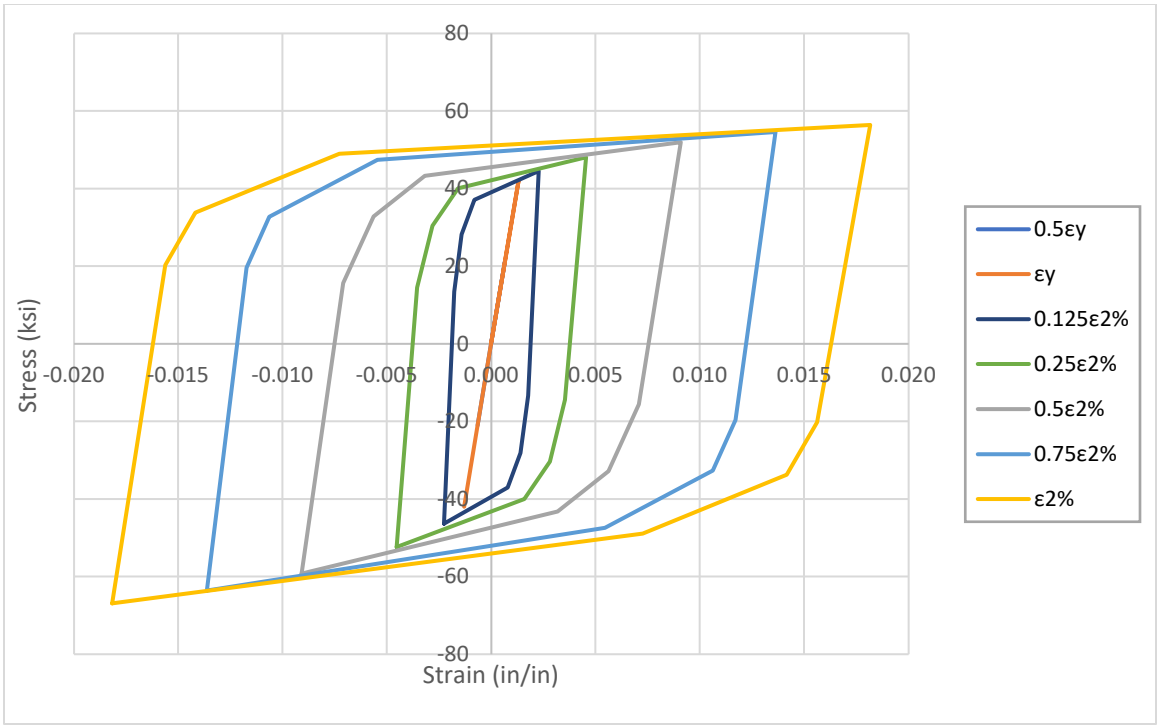

Figure 99: Final hysteretic stress-strain relationships for scaled brace at predetermined strain levels

Appendix B

Precast and Connection Design Drawings

Engineer's Drawings

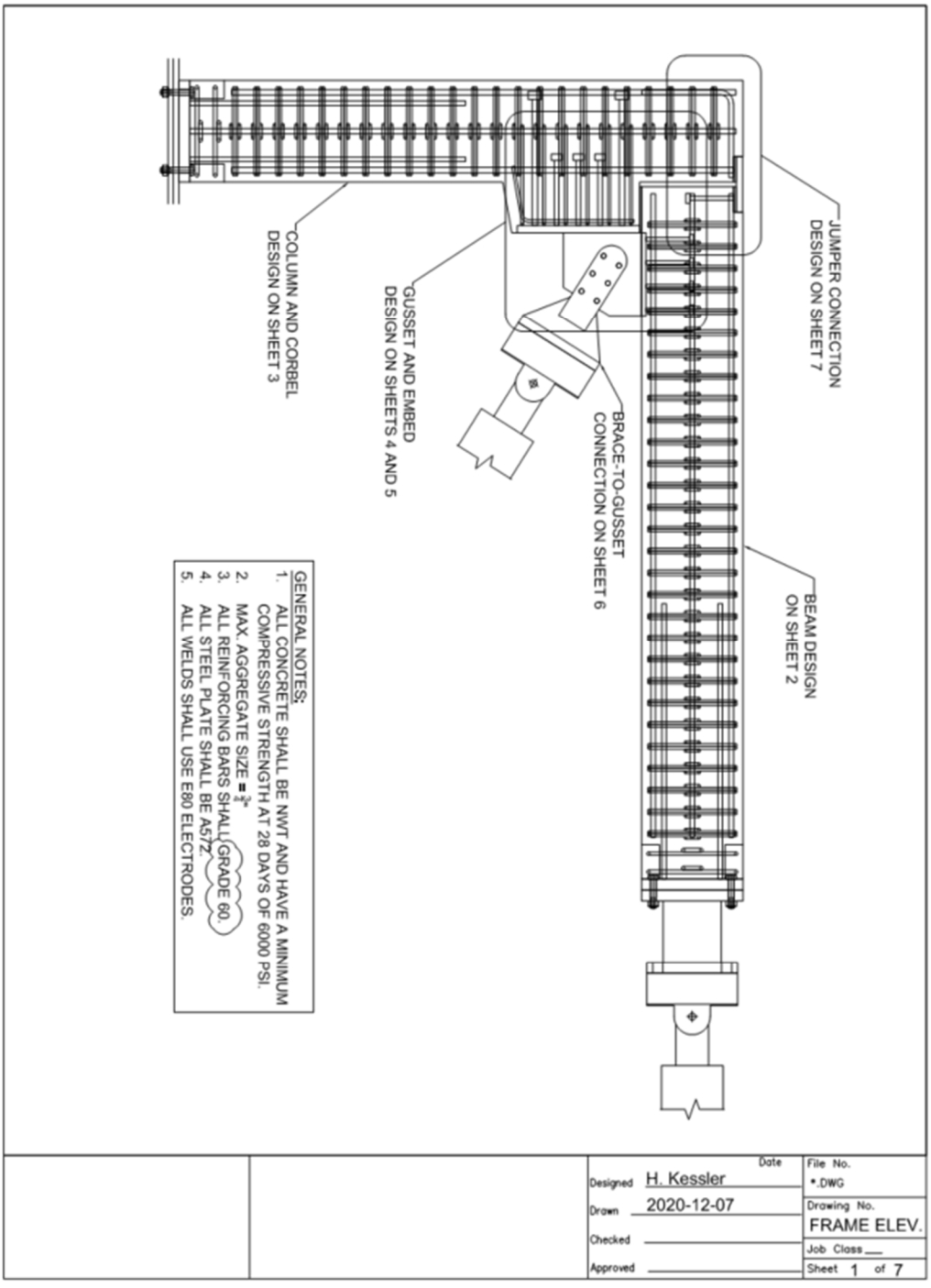

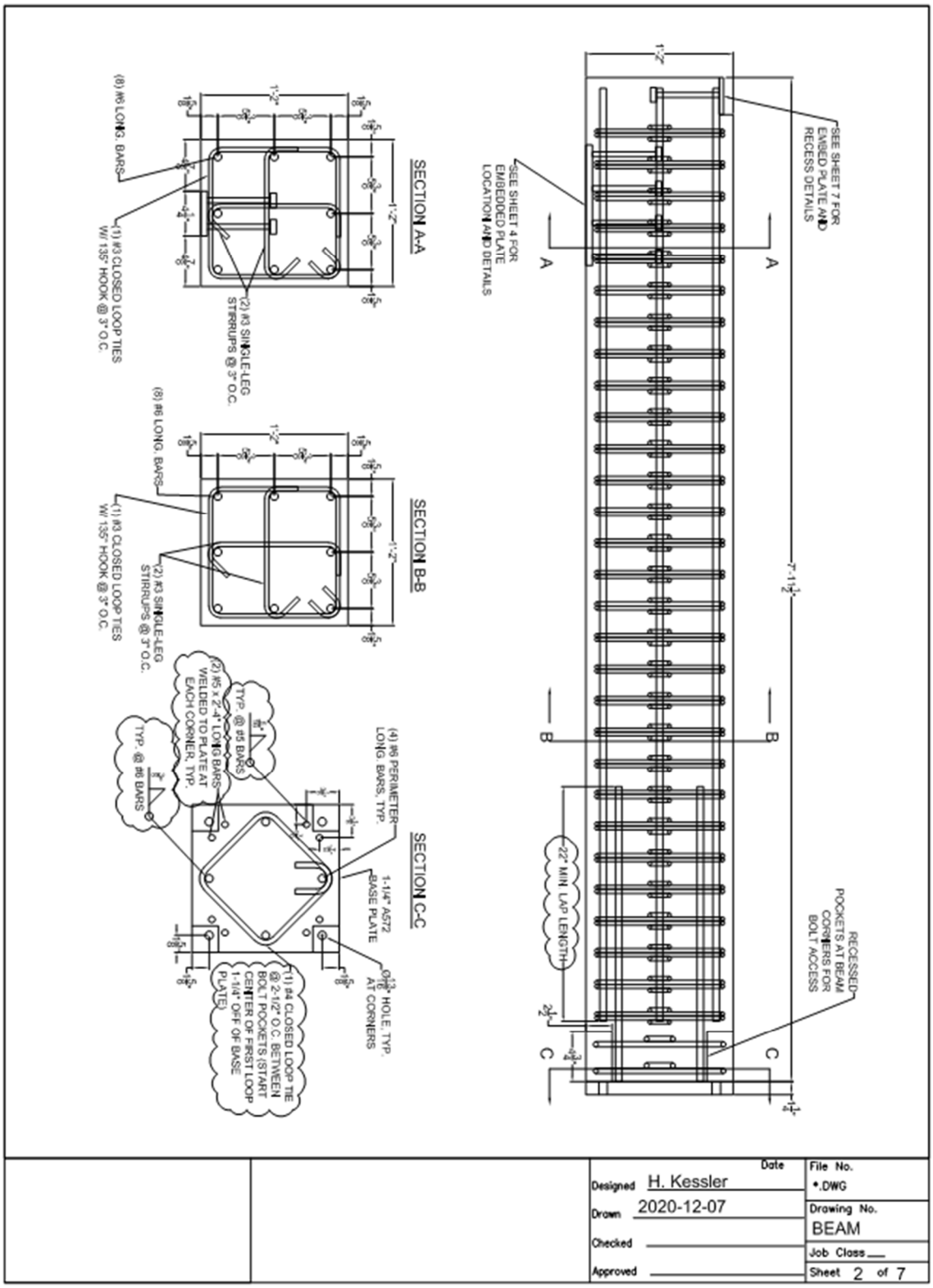

		Designed H. Kessler	Date
		Drawn 2020-12-07	File No. *.DWG
		Checked	Drawing No. BEAM
		Approved	Job Class___
			Sheet 2 of 7

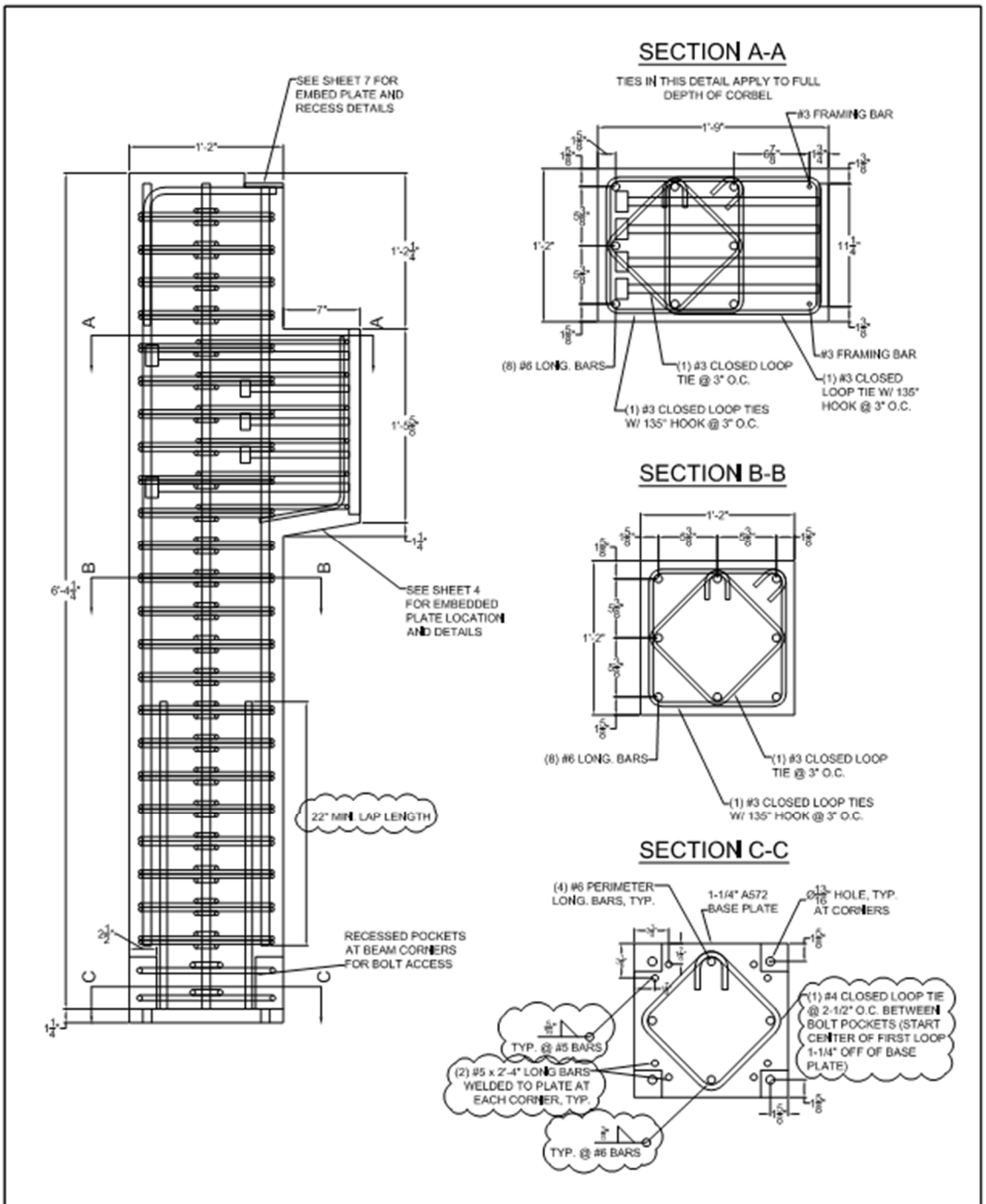

		Designed H. Kessler	File No. *.DWG
		Drawn 2020-12-07	Drawing No. COL/CORBEL
		Checked	Job Class
		Approved	Sheet 3 of 7

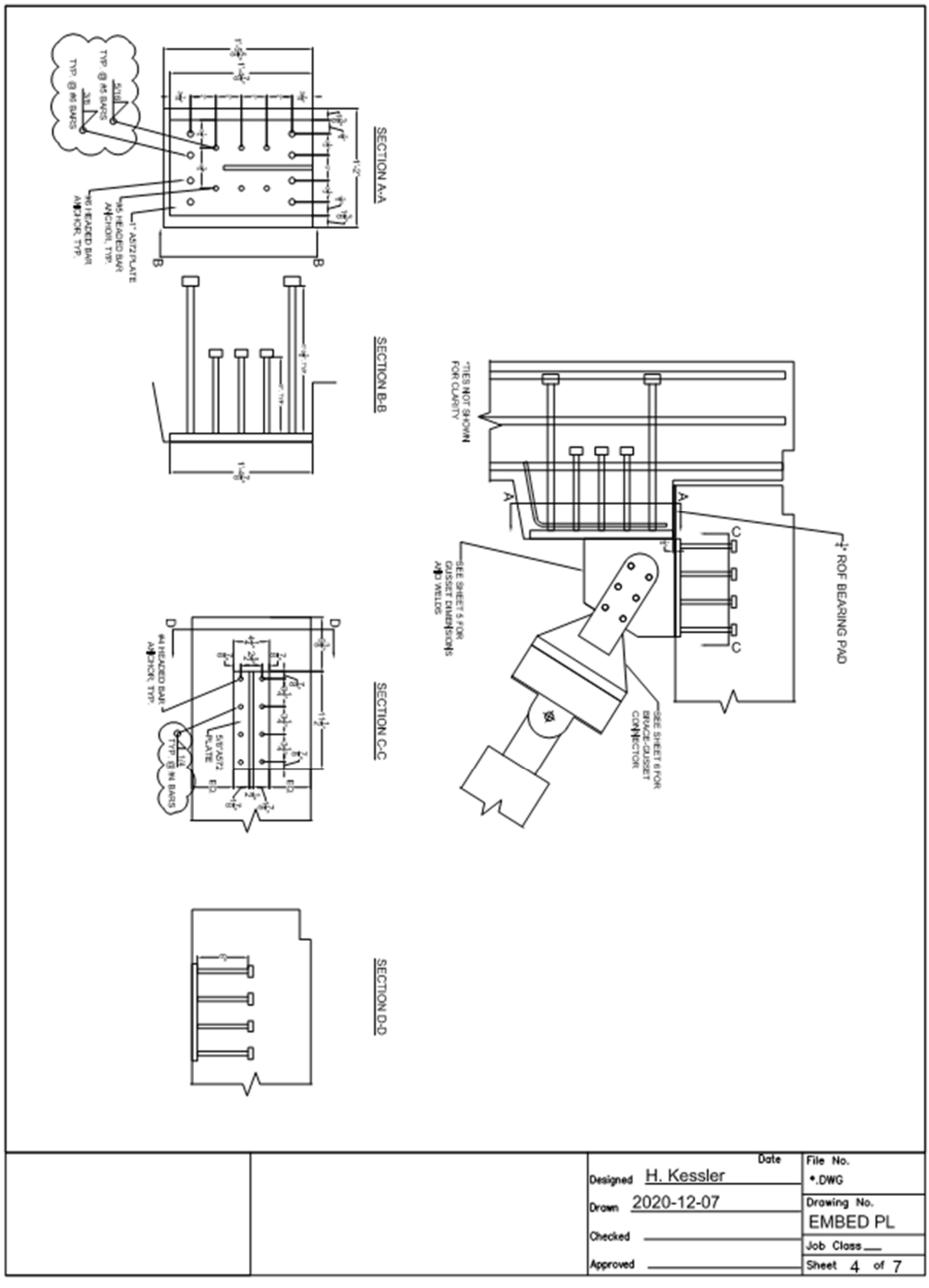
SECTION A-A
SECTION B-B
SECTION C-C
SECTION D-D
ROF BEARING PAD
*TIES NOT SHOWN FOR CLARITY
SEE SHEET 5 FOR GUSSET DIMENSIONS AND WELDS
SEE SHEET 6 FOR BRACE-GUSSET CONNECTOR
Designed H. Kessler
Drawn 2020-12-07
Checked
Approved
Date
File No. *.DWG
Drawing No. EMBED PL
Job Class
Sheet 4 of 7

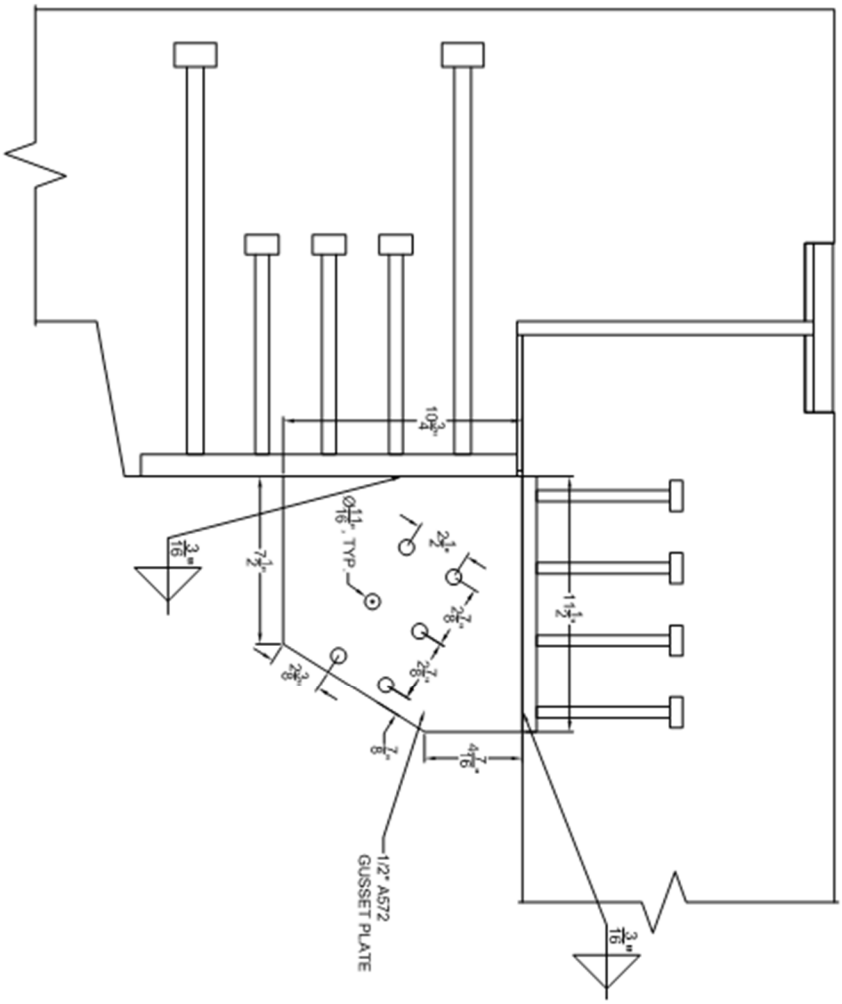

		Date	File No.
		Designed H. Kessler	*.DWG
		Drawn 2020-10-02	Drawing No. GUSSET PL
		Checked	Job Class
		Approved	Sheet 5 of 7

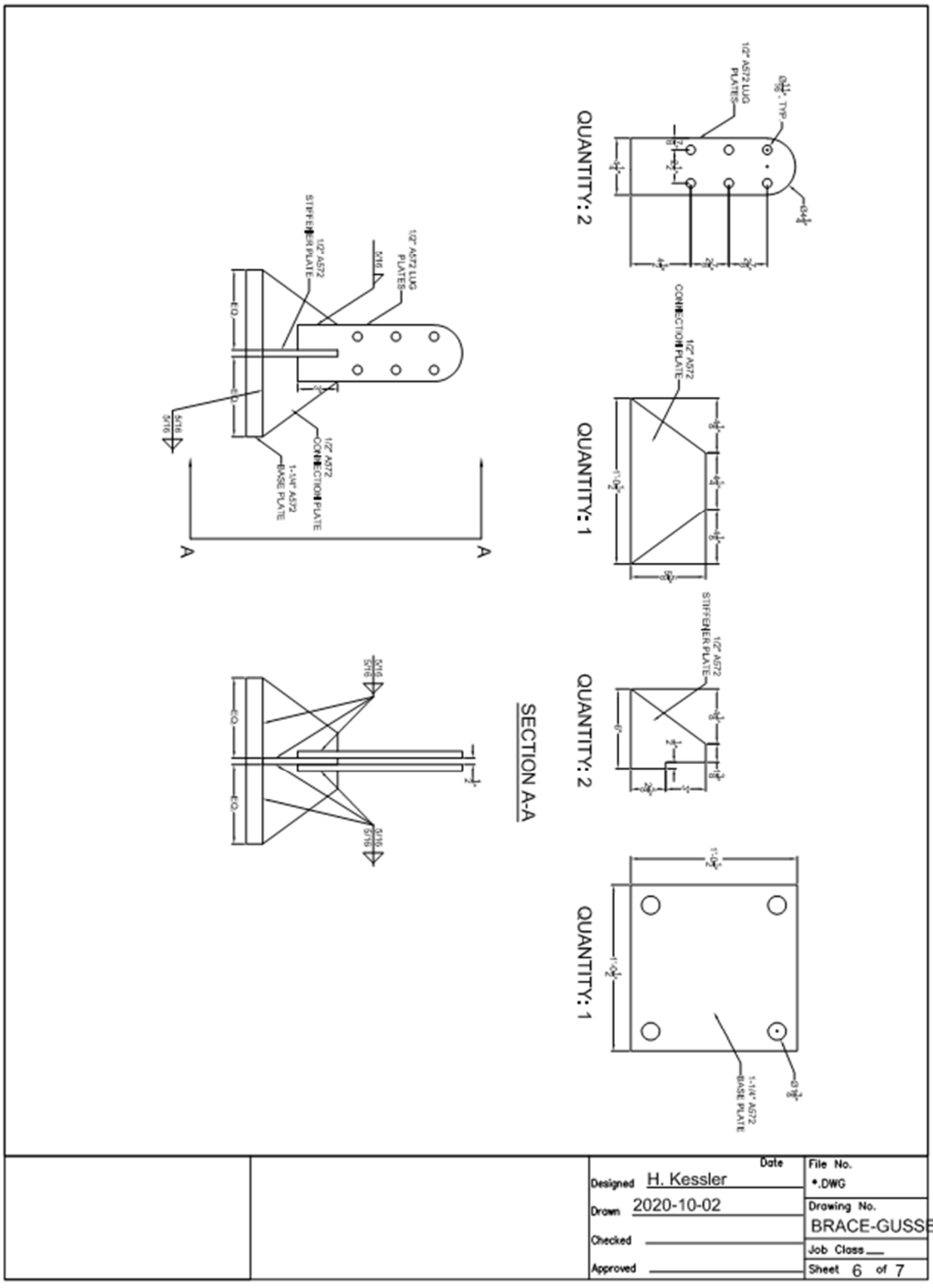

		Designed H. Kessler	Date
		Drawn 2020-10-02	File No. *.DWG
		Checked	Drawing No. BRACE-GUSSET
		Approved	Job Class ___
			Sheet 6 of 7

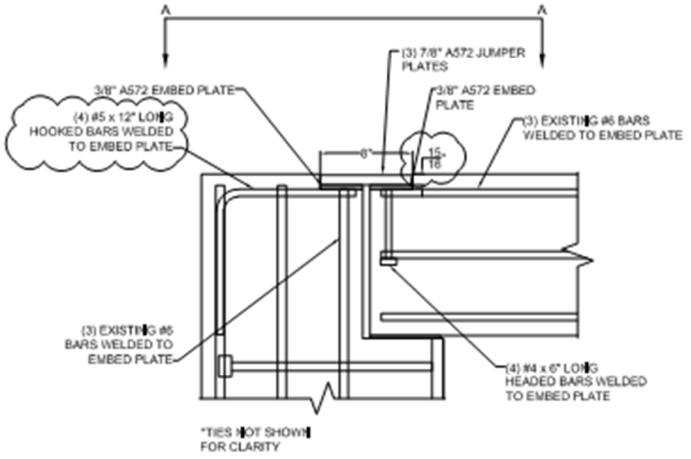

SECTION A-A

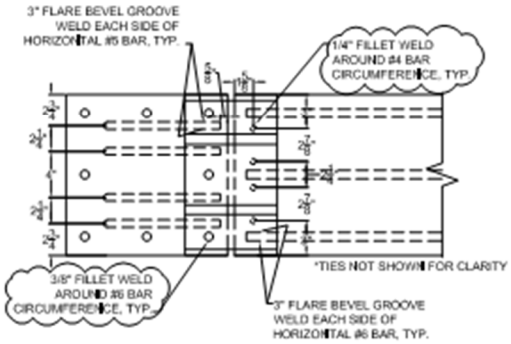

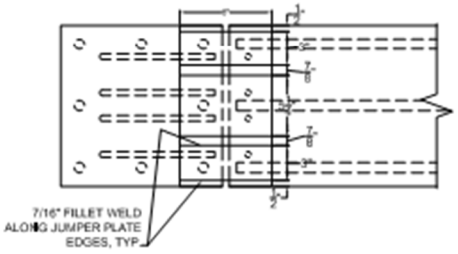

		Designed H. Kessler	File No. *.DWG
		Drawn 2020-12-07	Drawing No. BEAM-COL
		Checked	Job Class
		Approved	Sheet 7 of 7

REFERENCES

[1] Christopulos, Adam S. 2005. “Improved Seismic Performance of Buckling Restrained Braced Frames.”

[2] Black, Cameron J, Nicos Makris, and Ian Aiken. 2004. “Component Testing, Seismic Evaluation and Characterization of Buckling-Restrained Braces.” *Journal of Structural Engineering* 130 (6): 880–94.

[3] Tremblay, R., L. Poncet, P. Bolduc, R. Neville, and R. DeVall. 2004. “Testing and Design of Buckling Restrained Braces for Canadian Application.” In *Proceeding of the 13th World Conference on Earthquake Engineering*.

[4] Newell, James, Chia-Ming Uang, and Gianmario Benzoni. 2006. “Subassemblage Testing of Corebrace Buckling-Restrained Braces (G Series).”

[5] Corte, Gaetano Della, Mario D’Aniello, Raffaele Landolfo, and Federico M. Mazzolani. 2011. “Review of Steel Buckling-Restrained Braces.” *Steel Construction* 4 (2): 85–93. https://doi.org/10.1002/stco.201110012.

[6] *PCI Design Handbook: Precast and Prestressed Concrete*. 2017. 8th ed. Chicago: Precast/Prestressed Concrete Institute.

[7] Polat, Gul. 2008. “Factors Affecting the Use of Precast Concrete Systems in the United States.” *Journal of Construction Engineering and Management* 134 (3): 169–78.

[8] Viano, Jeffrey D., and Thomas C. Schaeffer. 2017. “Novel Use of Buckling-Restrained Braces in Precast Concrete Frames.” *PCI Journal* 62 (5): 28–34.

[9] Thornton, William. 1991. “On the Analysis and Design of Bracing Connections.” In *Proceedings of AISC National Steel Conference*.

[10] Lin, Pao-Chun, Keh-Chyuan Tsai, An-Chien Wu, and Ming-Chieh Chuang. 2014. “Seismic Design and Test of Gusset Connections for Buckling-Restrained Braced Frames.” *Earthquake Engineering and Structural Dynamics* 43: 565–87.

[11] Lin, Pao-Chun, Keh-Chyuan Tsai, An-Chien Wu, Ming-Chieh Chuang, Chao-Hsein Li, and Kung-Juin Wang. 2015. “Seismic Design and Experiment of Single and Coupled Corner Gusset Connections in a Full-Scale Two-Story Buckling-Restrained Braced Frame.” *Earthquake Engineering and Structural Dynamics* 44: 2177–98.

[12] Tsai, Ching-Yi, Keh-Chyuan Tsai, Li-Wei Chen, and An-Chien Wu. 2018. "Seismic Performance Analysis of BRBs and Gussets in a Full-Scale 2-Story BRB-RCF Specimen." *Earthquake Engineering and Structural Dynamics* 47: 2366–89.

[13] Cui, Yao, Xiaozhuo Xu, Tracy C. Becker, and Wei Zhang. 2021. "Incorporating Frame Action into Seismic Design of Gusset Plates." *Journal of Structural Engineering* 147 (3).

[14] *Building Code Requirements for Structural Concrete (ACI 318-19): An ACI Standard; Commentary on Building Code Requirements for Structural Concrete (ACI 318R-19)*. 2020. Farmington Hills: American Concrete Institute.

[15] Coy, Bradly B. 2007. "Buckling-Restrained Braced Frame Connection Design and Testing." Brigham Young University.

[16] Guerrero, Hector, Tianjian Ji, J. Alberto Escobar, and Amador Teran-Gilmore. 2018. "Effects of Buckling-Restrained Braces on Reinforced Concrete Precast Models Subjected to Shaking Table Excitation." *Engineering Structures* 163: 294–310.

[17] Maddux, Gene E., Leon A. Vorst, Joseph F. Giessler, and Terence Moritz. 1969. "Stress Analysis Manual."

[18] "CoreBrace Products." n.d. https://corebrace.com/products/.

[19] Muir, Larry S. 2008. "Designing Compact Gussets with the Uniform Force Method." *AISC Engineering Journal* 45 (1): 13–20.

[20] *Steel Construction Manual*. 2017. 15th ed. American Institute of Steel Construction.

[21] Gross, John L., and Geraldine Cheok. 1988. "Experimental Study of Gusseted Connections for Laterally Braced Steel Buildings."

[22] Bjorhovde, Reidar, and S. K. Chakrabarti. 1985. "Tests of Full-Size Gusset Plate Connections." *Journal of Structural Engineering* 111 (3): 667–84.

[23] Maheri, Mahmoud R., and S. Yazdani. 2016. "Design of Steel Brace Connection to an RC Frame Using Uniform Force Method." *Journal of Constructional Steel Research* 116: 131–40.

[24] Maheri, M. R., and A. Hadjipour. 2003. "Experimental Investigation and Design of Steel Brace Connection to RC Frame." *Engineering Structures* 25 (13): 1707–14

[25] *ANSI/AISC 360-16 Specification for Structural Steel Buildings*. 2016. Chicago: American Institute of Steel Construction.

[26] Muir, Larry S., and William Thornton. 2014. *Steel Design Guide 29, Vertical Bracing Connections--Analysis and Design*. Chicago: American Institute of Steel Construction.

[27] *ANSI/AISC 341-16 Seismic Provisions for Structural Steel Buildings*. 2016. Chicago: American Institute of Steel Construction.

[28] *ASTM International. A36/A36M-19 Standard Specification for Carbon Structural Steel*. West Conshohocken, PA; ASTM International, 2019.

[29] *ASCE/SEI 7-16 Minimum Design Loads and Associated Criteria for Buildings and Other Structures*. 2017. Reston: American Society of Civil Engineers.

[30] Darwin, David, Charles W Dolan, and Arthur H Nilson. 2016. *Design of Concrete Structures*. 15th ed. New York: McGraw Hill Education.

[31] Kaufmann, E, B Metrovich, and Alan Pense. 2001. "Characterization of Cyclic Inelastic Strain Behavior on Properties of A572 Gr. 50 and A913 Gr. 50 Rolled Sections."

[32] Patwardhan, Pranav S., Rajprasad A. Nalavde, and Daniel Kujawski. 2019. "An Estimation of Ramberg-Osgood Constants for Materials with and without Luder's Strain Using Yield and Ultimate Strengths." In *ICSI 2019 The 3rd International Conference on Structural Integrity*, 17:750–57. Elsevier B.V.

[33] Lee, Y. L., J. Pan, R. Hathaway, and M. Barkey. 2005. *Fatigue Testing and Analysis: Theory and Practice*. Oxford: Elsevier Butterworth-Heinemann.